DIGITAL ACCESS TO SCHOLARSHIP AT HARVARD
DASH.HARVARD.EDU

HARVARD LIBRARY
Office for Scholarly Communication

Measurements of Interaction-Driven States in Monolayer and Bilayer Graphene

Citation
Feldman, Benjamin Ezekiel. 2013. Measurements of Interaction-Driven States in Monolayer and Bilayer Graphene. Doctoral dissertation, Harvard University.

Permanent link
http://nrs.harvard.edu/urn-3:HUL.InstRepos:11181079

Terms of Use
This article was downloaded from Harvard University's DASH repository, and is made available under the terms and conditions applicable to Other Posted Material, as set forth at http://nrs.harvard.edu/urn-3:HUL.InstRepos:dash.current.terms-of-use#LAA

Share Your Story

The Harvard community has made this article openly available.
Please share how this access benefits you. Submit a story .

Accessibility

Measurements of Interaction-Driven States in Monolayer and Bilayer Graphene

A dissertation presented
by

Benjamin Ezekiel Feldman

to
The Department of Physics
in partial fulfillment of the requirements
for the degree of
Doctor of Philosophy
in the subject of

Physics

Harvard University
Cambridge, Massachusetts
August 2013

©2013 - Benjamin Ezekiel Feldman

All rights reserved.

Dissertation Advisor:

Professor Amir Yacoby

Author:

Benjamin Ezekiel Feldman

Measurements of Interaction-Driven States in Monolayer and Bilayer Graphene

Abstract

In materials systems with flat energy bands and limited disorder, interactions among electrons dominate and can dramatically alter physical behavior. Two-dimensional electron gases (2DEGs) offer excellent platforms to study these effects because the kinetic energy of the electrons is effectively quenched by a perpendicular magnetic field. The recent discovery of graphene, a two-dimensional form of carbon, has opened the door for further exploration into many-body phenomena. Graphene, unlike conventional 2DEGs, has fourfold degenerate electronic states due to its spin and valley degrees of freedom. This thesis describes several experiments that show how these underlying symmetries combine with electron-electron interactions to produce novel and tunable correlated electronic phases of matter.

We perform transport measurements of bilayer graphene flakes that are suspended above the substrate to minimize disorder. The data reveal full lifting of the degeneracy of the lowest Landau level (LL) due to electron-electron interactions as well as insulating behavior at the charge neutrality point. Using a scanning single-electron transistor (SET) to measure the local electronic compressibility, we quantitatively explore these broken-symmetry quantum Hall states as a function of magnetic field. Surprisingly, the measurements also reveal a correlated phase at zero electric and magnetic field.

When applied to suspended monolayer graphene, the high SET sensitivity and low disorder afforded by local measurements combine to reveal a multitude of fractional quantum

Hall (FQH) states whose sequence differs from that in conventional 2DEGs. This unique pattern reflects the spin and valley degeneracies in graphene, and changing the magnetic field leads to a series of phase transitions between FQH states with different spin and/or valley polarization. We also perform compressibility measurements of a bilayer graphene sample on boron nitride that show an electron-hole asymmetric pattern of FQH states.

Finally, we conduct local compressibility measurements that reveal changes in behavior near a monolayer-bilayer graphene interface. These preliminary findings suggest that the energy gap at the charge neutrality point closes where the two sides meet, and they highlight the possibility of locally tuning the band structure in graphene systems.

Contents

Title Page i
Abstract iii
Table of Contents v
List of Figures vii
Author List ix
Acknowledgments x
Dedication xiii

1 Introduction **1**
1.1 The Physics of Graphene 2
1.2 2DEGs in a Magnetic Field 7
1.3 Electron-Electron Interactions 12
1.4 Electronic Compressibility 16
1.5 Outline of This Thesis 21

2 Broken-Symmetry States and Divergent Resistance in Suspended Bilayer Graphene **22**
2.1 Introduction 23
2.2 Zero-Field Electronic Transport 24
2.3 Broken-Symmetry Quantum Hall States 27
2.4 Resistance at $\nu = 0$ 30
2.5 Methods 34
2.6 Supplementary Discussion 34

3 Local Compressibility Measurements of Correlated States in Suspended Bilayer Graphene **39**
3.1 Introduction 40
3.2 Energy Gaps and Widths of Quantum Hall States 41
3.3 Correlated State at Zero Field 45
3.4 Methods 50
3.5 Supplementary Discussion 50
3.6 Epilogue 54

4 Unconventional Sequence of Fractional Quantum Hall States in Suspended Graphene **56**
4.1 Introduction . . . 57
4.2 Fractional Quantum Hall (FQH) States . . . 58
4.3 Unconventional Sequence of FQH States . . . 60
4.4 Steps in Chemical Potential and Widths of FQH States . . . 63
4.5 Spatial Dependence . . . 66
4.6 Methods . . . 67
4.7 Supplementary Discussion . . . 68

5 Fractional Quantum Hall Phase Transitions and Four-Flux States in Graphene **84**
5.1 Introduction . . . 85
5.2 FQH Phase Transitions . . . 88
5.3 Model and Numerical Simulation . . . 89
5.4 Steps in Chemical Potential . . . 93
5.5 Four-Flux Composite Fermion States . . . 94
5.6 Methods . . . 96
5.7 Supplementary Discussion . . . 96

6 Electron-Hole Asymmetric Fractional Quantum Hall Effect in Bilayer Graphene **105**
6.1 Introduction . . . 106
6.2 FQH states in Bilayer Graphene . . . 107
6.3 Electron-Hole Asymmetric Sequence of States . . . 110
6.4 Steps in Chemical Potential of FQH States . . . 111
6.5 Methods . . . 114
6.6 Supplementary Discussion . . . 115

7 Electronic Compressibility at a Monolayer-Bilayer Graphene Interface **119**
7.1 Introduction . . . 120
7.2 Changes in Quantum Hall States . . . 122
7.3 Absence of Localized States at $\nu = 0$ . . . 124
7.4 Reproducibility and Outlook . . . 126

A Fabrication of Suspended Graphene Samples **129**
A.1 Fabrication of Suspended Devices . . . 129
A.2 Current Annealing . . . 130

B Scanning Single-Electron Transistor Microscope **131**
B.1 SET Fabrication . . . 131
B.2 Tips and Tricks for Running the Microscope . . . 132

Bibliography **137**

List of Figures

1.1 Graphene schematic . . . 3
1.2 Graphene band structure . . . 4
1.3 Graphene pseudospin . . . 5
1.4 Bilayer graphene schematic . . . 6
1.5 Bilayer graphene bands and pseudospin . . . 6
1.6 Landau levels (LLs) . . . 8
1.7 Quantum Hall effect in graphene . . . 10
1.8 Quantum Hall ferromagnetism . . . 14
1.9 Inverse compressibility . . . 17
1.10 Coulomb blockade . . . 18

2.1 Bilayer graphene transport at zero field . . . 25
2.2 Broken-symmetry states in bilayer graphene . . . 28
2.3 Quantization of states . . . 29
2.4 Temperature dependence of $\nu = 0$ resistance . . . 31
2.5 Scaling of $\nu = 0$ resistance . . . 32
2.6 Fluctuations in $\nu = 0$ resistance . . . 34
2.7 Suspended bilayer graphene Hall bar . . . 36
2.8 Inhomogeneity in Hall bar devices . . . 37

3.1 Scanning single-electron transistor measurement setup . . . 42
3.2 Energy gaps of broken-symmetry states in bilayer graphene . . . 43
3.3 Compressibility at low field . . . 46
3.4 Transport at low field . . . 47
3.5 Zero-field compressibility at large densities . . . 51
3.6 Spatial dependence of low-field compressibility . . . 52
3.7 Additional measurements of $|\nu| = 4$ energy gaps . . . 53

4.1 Measurement setup and Landau fan . . . 59
4.2 Sequence of fractional quantum Hall (FQH) states in graphene . . . 61
4.3 Steps in chemical potential and incompressible peak widths . . . 64
4.4 Spatial dependence of FQH states . . . 66
4.5 Magnetotransport through a monolayer-bilayer hybrid . . . 68

4.6 Inverse compressibility before current annealing 70
4.7 Spatial dependence before current annealing 71
4.8 FQH states before current annealing 72
4.9 Steps in chemical potential and widths before current annealing 73
4.10 Inverse compressiblity after gentle current annealing 74
4.11 Steps in chemical potential after gentle current annealing 75
4.12 Spatial average of inverse compressibility 76
4.13 Determining the zero of inverse compressibility 76
4.14 Extrapolated FQH steps in chemical potential 78
4.15 Measurements at additional positions 81
4.16 Two-dimensional spatial map at $\nu = 0$ 82

5.1 Phase transitions of FQH states in graphene 87
5.2 Composite Fermion LL schematic and numerical simulation 91
5.3 Steps in chemical potential of FQH states 93
5.4 Four-flux FQH states 95
5.5 Phase transitions at other locations 100
5.6 Phase transition at $\nu = 2/3$ in a dirtier sample 102
5.7 Zoom-ins on phase transitions 103

6.1 Sample characterization 108
6.2 FQH states in bilayer graphene 109
6.3 Steps in chemical potential of FQH states 112
6.4 Spatial dependence of inverse compressibility 113
6.5 Inverse compressibility of higher LLs 115
6.6 Effect of current annealing 116
6.7 Large geometric capacitance 117

7.1 Schematic and properties of a monolayer-bilayer hybrid 121
7.2 Inverse compressibility at a monolayer-bilayer interface 123
7.3 Spatial map of inverse compressibility at $\nu = 0$ 125
7.4 Absence of localized states at the interface 126
7.5 Effect of current annealing 127
7.6 Interface behavior in a sample on boron nitride 128

Author List

Chapter 2 is adapted from:
B. E. Feldman, J. Martin and A. Yacoby, Broken-Symmetry States and Divergent Resistance in Suspended Bilayer Graphene, *Nat. Phys.* **5**, 889-893 (2009).

Chapter 3 is adapted from:
J. Martin, B. E. Feldman, R. T. Weitz, M. T. Allen and A. Yacoby, Local Compressibility Measurements of Correlated States in Suspended Bilayer Graphene, *Phys. Rev. Lett.* **105**, 256806 (2010).

Chapter 4 is adapted from:
B. E. Feldman, B. Krauss, J. H. Smet and A. Yacoby, Unconventional Sequence of Fractional Quantum Hall States in Suspended Graphene, *Science* **337**, 1196-1199 (2012).

Chapter 5 is adapted from:
B. E. Feldman, A. J. Levin, B. Krauss, D. A. Abanin, B. I. Halperin J. H. Smet and A. Yacoby, Fractional Quantum Hall Phase Transitions and Four-Flux States in Graphene, *Phys. Rev. Lett.* **111**, 076802 (2013).

Chapter 6: Data obtained by A. Kou, B. E. Feldman and A. J. Levin. Text and figures prepared by A. Kou and B. E. Feldman.

Chapter 7: Data obtained by B. E. Feldman, B. Krauss, A. Kou and A. J. Levin. Text and figures (except where noted) prepared by B. E. Feldman.

Acknowledgments

This thesis is a product of the help and support of many spectacular people with whom I've had the pleasure to work. First and foremost, I thank my advisor, Amir Yacoby. He has cultivated an incredibly stimulating lab environment, and his excitement at the sight of new data and eagerness to discuss physics served as mentorship, motivation, and guidance. It has been a fantastic experience working with Amir, whose excellent experimental intuition and strong theoretical underpinning have generated creative approaches to interesting and important problems.

I am also indebted to Jens Martin, who taught me much of what I know about performing physics experiments. He explained everything from fabrication to graphene and quantum Hall physics to running the scanning single-electron transistor (SET) microscope. Not only was he a great resource, but he had infinite patience, and he provided an unending supply of creative ideas.

All the work in this thesis was a collaborative effort by various combinations of team graphene members. While we overlapped, Jens Martin was always at my side measuring and analyzing the data, and even after becoming a professor, he took the time to help troubleshoot major problems with the scanning SET microscope. Monica Allen is a wizard in the cleanroom, and a current annealing guru; this thesis is significantly longer because she took the time to current anneal samples with and for me. It was a pleasure to work with Thomas Weitz, who very quickly pushed our fabrication and measurement processes to new levels and was always available for stimulating discussions over coffee. Eva Peters and Beni Krauss contributed proportionally way more than the timeframes of their visits would indicate, and we have developed great friendships that are rekindled at (and result in!) international conferences. It was also a pleasure to work with Angela Kou, who somehow found time to help fix the microscope, bring a new class of ultraclean graphene to the Yacoby group, and push both measurement and interpretation forward, all in less than a

year. Finally, it has been great working with Andrei Levin and DiDi Wei, who have provided fresh enthusiasm to team graphene as they tackle difficult new problems. The microscope and team graphene are in good hands.

In addition to the guidance from Jens, I have also learned a lot from discussions with Vivek Venkatachalam and Sean Hart about electronic compressibility and SET measurements/fabrication. Thanks to Sean for experimental acrobatics as well. Hey, it's Mikey Shulman! Thank you for teaching me about quantum computing, and it was a pleasure working with you on the new Frossati fridge.

The graduate school experience is largely dependent on interactions with colleagues, and the members of the Yacoby group are some of the smartest and most capable people I know. In addition to those mentioned above, thanks to everyone for teaching me physics during countless blackboard and lunch table discussions: post-docs Hendrik Bluhm, Patrick Maletinsky, Oliver Dial, Lan Luan, Kristiaan de Greve and Marc Warner, graduate students Gilad Barak, Sandra Foletti, Sungkun Hong, Mike Grinolds, Gilad Ben-Shach, Shannon Harvey, Yuliya Dovzhenko and Hechen Ren, as well as visitors Timo Wagner, Susanne Muller and Lucas Thiel. Moreover, thanks to everyone for helping to keep things fun with late-night German Starcraft, MarioKart, and soccer. I've redacted your names for protection, but you know who you are.

The Yacoby lab has benefitted from several assistants who work tirelessly to make everything run smoothly. Thanks to Danielle Reuter, and most recently and most of all, Carolyn Moore, for being the glue that holds the lab together.

I have also had the privelege of collaborating with many amazing people outside of the Yacoby group. Although not every project has succeeded (yet), they were all excellent experiences. Beni Krauss and Jurgen Smet have been wonderful collaborators and friends, and they helped plan and complete the work on monolayer-bilayer hybrid devices, including

the measurements that only focused on one side of the resulting miracle device. Thanks to Paul Cadden-Zimansky, Yue Zhao, Fereshte Ghahari and Kirill Bolotin from the Philip Kim group for taking me in as one of their own and showing me how to measure at the National High Magnetic Field Lab. More recently, teaming up with Patrick Maher, Cory Dean and Philip Kim has also been rewarding. Working with Alex Kitt and Sebastian Remi from Bennett Goldberg's group on strain in suspended bilayer graphene was also a great experience, and I thank them as well as Ajit Srivastava from Atac Imamoglu's group for teaching me about optical measurements. Finally, thanks to Xu Zhang from the group of Tomas Palacios for a stimulating collaboration on the chlorination of suspended graphene flakes.

Last but certainly not least, I couldn't have made it through my graduate work without the constant support of friends and family. Mom and Papi, Naomi, and especially Lesley, you've been there throughout both highs and lows, and have always provided exactly the support I needed. And thank you for your gentle reminders that the world won't end if I occasionally leave lab!

Dedicated to my family, for their endless love and support.

Chapter 1

Introduction

Although there are relatively few fundamental constituents of matter, the diversity of physical behavior observed in condensed matter systems is staggering. Many of these differences can be explained in terms of the interaction between an individual electron and the surrounding lattice of atoms, and the tight binding model provides a straightforward prescription to determine the resulting band structure. However, some of the most surprising and remarkable physical phenomena, ranging from magnetism to superconductivity to the fractional quantum Hall effect (FQHE), originate from interactions among electrons. Predicting the consequences of electron-electron interactions is very difficult, and many-body effects can profoundly influence physical properties. This is especially true in systems with flat energy bands and very little disorder, because electron-electron interactions provide the dominant energy scale.

Historically, two-dimensional electron gases (2DEGs) have provided excellent platforms to explore many-body effects. Subjecting electrons moving in two dimensions to a perpendicular magnetic field leads to flat energy bands known as Landau levels (LLs), and measuring these systems resulted in the discovery of the integer [1] and fractional [2] quantum

Hall effects. Recently, a new class of 2DEG based on atomically thin sheets of carbon atoms has been experimentally realized [3], leading to a number of surprises and reinvigorating the study of quantum Hall physics. This thesis describes several experiments that probe how electron-electron interactions influence the behavior of carbon-based 2DEGs.

1.1 The Physics of Graphene

A wide variety of carbon allotropes are known to exist in nature: in addition to three-dimensional diamond and graphite crystals, zero-dimensional fullerenes and one-dimensional carbon nanotubes have also generated significant interest. Although graphite is composed of atomically thin layers of carbon known as graphene, individual crystalline sheets were not expected to be physically stable [4], and the concept of graphene was originally used only as a theoretical tool to understand the band structure of graphite and carbon nanotubes. In 2004, however, Kostya Novoselov and Andre Geim discovered a method to isolate individual graphene layers on Si substrates capped with SiO_2 [3].

Graphene is made up of carbon atoms arranged in a hexagonal lattice with a two-atom basis (Fig. 1.1), resulting in a honeycomb structure with a nearest-neighbor separation of 1.42 Å and a lattice constant $a = 2.46$ Å. Although the carbon atoms are physically indistinguishable, it is convenient to label the two sublattices A and B. Each carbon atom has sp^2-hybridized bonds with three nearest neighbors of the opposite sublattice. The fourth valence electron of each atom occupies a p_z orbital orthogonal to the graphene plane, and these electrons are connected in a delocalized network of π bonds.

1.1.1 Band structure

Performing a tight-binding calculation on the graphene lattice that only takes into account the π bonds and assumes nearest neighbor hopping $\gamma_0 \approx 3$ eV leads to the dispersion

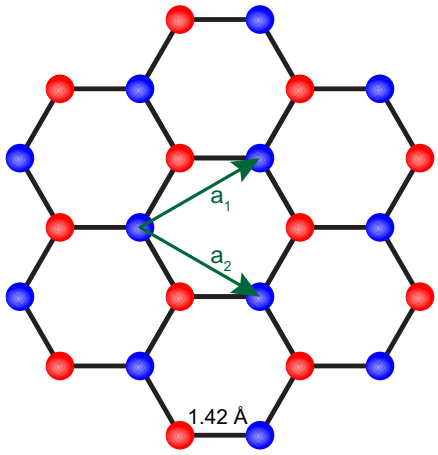

Figure 1.1: Graphene schematic, with the red and blue spheres representing sublattices A and B, respectively, and the black lines representing the bonds between atoms. The distance between carbon atoms and lattice vectors $\mathbf{a}_1$ and $\mathbf{a}_2$ are also labeled.

$$E = \pm\gamma_0\sqrt{3 + 2\cos[p_y a] + 4\cos[\frac{1}{2}p_y a]\cos[\frac{\sqrt{3}}{2}p_x a]}, \tag{1.1}$$

where $\boldsymbol{p}$ is the momentum and p_x, p_y are its components [5]. The graphene first Brillouin zone is hexagonal, and the band structure associated with Eq. 1.1 is shown in Fig. 1.2. It is characterized by low-energy cones, known as Dirac cones, with linear dispersion $E = \hbar v_F|\boldsymbol{k}|$, where $\hbar$ is Planck's constant divided by 2π, $v_F \approx 10^6$ m/s is the Fermi velocity of the charge carriers, and $\boldsymbol{k}$ is the momentum relative to the K or K' points, which occur at the corners of the first Brillouin zone. The valence and conduction bands meet at exactly the Fermi energy and are electron-hole symmetric. Although there are six Dirac cones, only two are inequivalent (the others are related by reciprocal lattice vectors), and they are time-reversed counterparts known as valleys K and K'.

The low-energy Hamiltonian of graphene can be conveniently written as

$$H = \hbar v_F \begin{pmatrix} 0 & k_x - ik_y \\ k_x + ik_y & 0 \end{pmatrix} = \hbar v_F \boldsymbol{\sigma} \cdot \boldsymbol{k}. \tag{1.2}$$

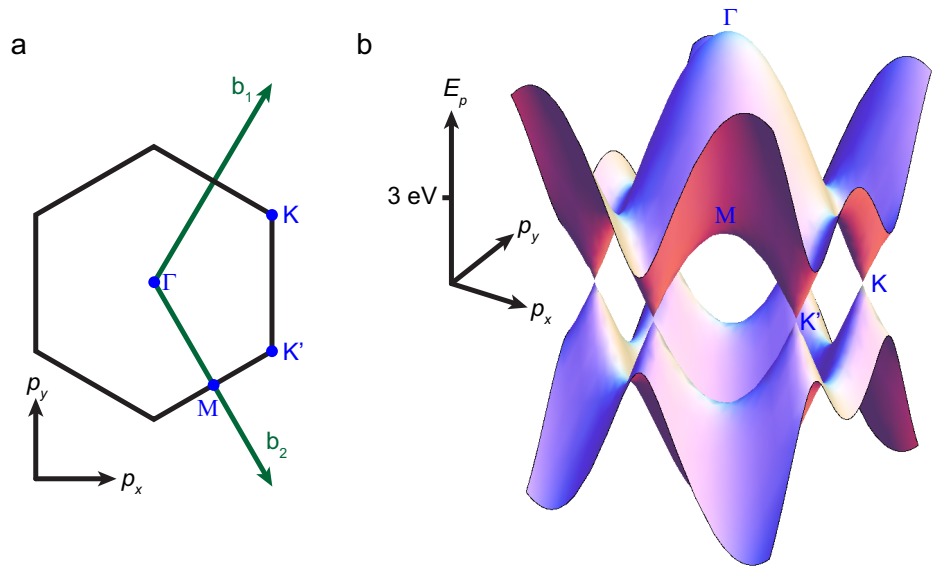

Figure 1.2: (a) First Brillouin zone of graphene, with high symmetry points labeled and reciprocal lattice vectors $\boldsymbol{b_i}$ shown. (b) The band structure of graphene. At low energies, the dispersion is linear and electron-hole symmetric, with the valence and conduction bands meeting at the Fermi energy.

Above, $\boldsymbol{\sigma}$ is a vector of the σ_x and σ_y Pauli matrices, and the Hamiltonian is expressed in the basis $\Psi = (\psi_A, \psi_B)$ of the sublattices for valley K (their order is reversed for valley K'). Eq. 1.2 has the same form as the Dirac equation for relativistic spin-1/2 particles, except that the Fermi velocity replaces the speed of light and the sublattice 'pseudospin' replaces real spin. The charge carriers in graphene therefore behave as massless Dirac fermions.

Graphene also has the special property that the momentum of its charge carriers relative to the K and K' points is linked to the sublattice degree of freedom, as illustrated in Fig. 1.3. The pseudospin relation is apparent from the wavefunction (again, for valley K)

$$\Psi = \frac{1}{\sqrt{2}} \begin{pmatrix} e^{-i\theta/2} \\ \pm e^{i\theta/2} \end{pmatrix}, \tag{1.3}$$

where θ is the angle of the momentum and $\pm$ refers to electrons (holes) [6]. Rotating θ by 2π adds an overall minus sign to Ψ, and this corresponds to a Berry's phase of π, which has important consequences in a magnetic field.

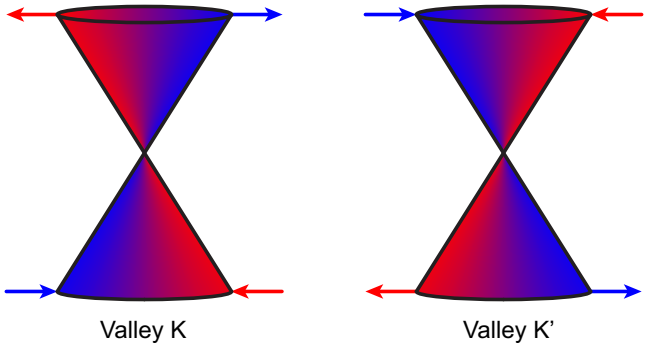

Figure 1.3: Dirac cones, with color representing the sublattice pseudospin. The colored arrows point in the direction of pseudospin, which is parallel (antiparallel) to the momentum for electrons in valley K (K'). The relation between pseudospin and momentum is opposite for electrons and holes.

1.1.2 Bilayer graphene

Bilayer graphene is a close relative of monolayer graphene, but it nonetheless exhibits starkly different physical properties. Its most common form is made by stacking two individual graphene sheets with 3.35 Å separation such that the atoms of one sublattice in the upper layer sit directly above atoms belonging to the other sublattice in the lower layer (Fig. 1.4). Because bilayer graphene has a four-atom basis, there are four energy bands to consider. However, only two are relevant at low energies because the nearest neighbor atoms in opposite layers hybridize to form bonding and antibonding states which are pushed away from the Fermi energy by the interlayer hopping energy scale $\gamma_1 \approx 0.4$ eV. Figure 1.5a shows a linecut of the resulting four-band dispersion around the K point.

To lowest order, the low-energy Hamiltonian of bilayer graphene is given by

$$H = \begin{pmatrix} U/2 & \hbar^2(k_x - ik_y)^2/2m^* \\ \hbar^2(k_x + ik_y)^2/2m^* & -U/2 \end{pmatrix}, \tag{1.4}$$

where $m^* \approx 0.042 m_e$ is the effective mass of the charge carriers, m_e is the electron mass, and U is the interlayer potential difference ($U = 0$ for intrinsic bilayer graphene) [7]. Like

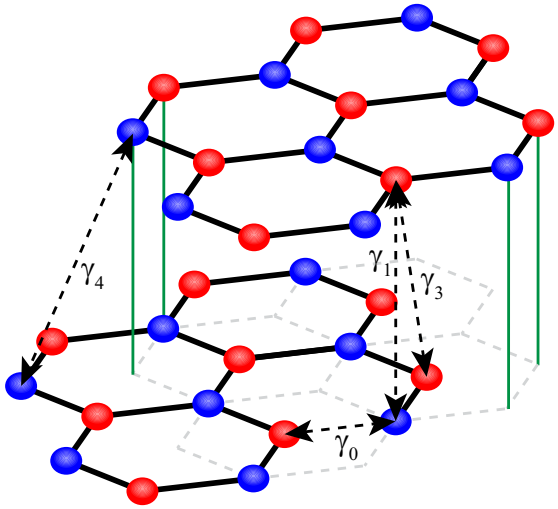

Figure 1.4: Schematic representation of Bernal-stacked bilayer graphene. Red and blue spheres represent the two sublattices of each layer, and the black lines are the nearest-neighbor in-plane bonds. Several hopping parameters γ_i are labeled.

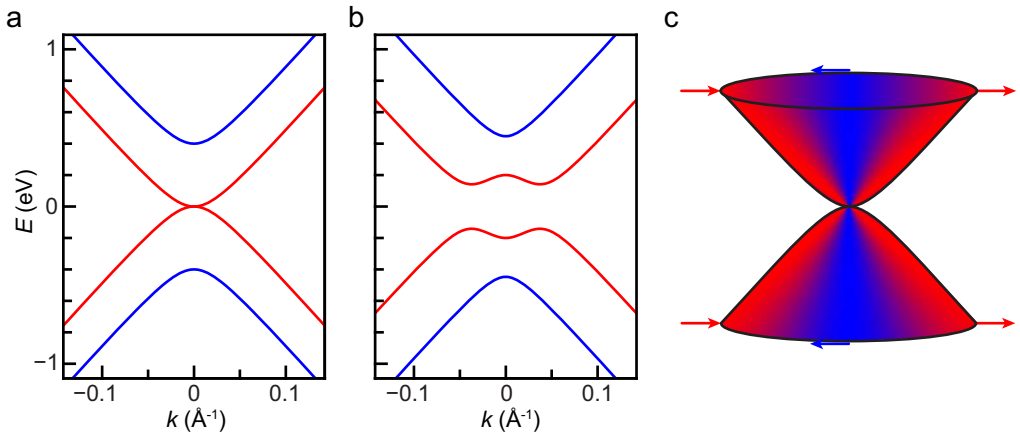

Figure 1.5: The band structure of bilayer graphene to lowest order, with layer symmetry (a), or including an interlayer potential difference equal to γ_1 (b). The low-energy (hybridized) bands are shown in red (blue). (c) Like monolayer graphene, there is a pseudospin-momentum relation, but it winds twice as quickly as in monolayers. Color represents the pseudospin, whose direction is marked with arrows at a few points.

monolayers, the low-energy states of bilayer graphene are centered around the K and K' points of the first Brillouin zone, and there is a twofold valley degeneracy. However, the dispersion is parabolic to lowest order at low energies, and although the charge carriers are chiral, the pseudospin rotates twice as fast as for monolayers (Fig. 1.5c), yielding a Berry's phase of 2π. The charge carriers in bilayer graphene are *massive* Dirac fermions.

Higher-order hopping terms (Fig. 1.4) slightly modify the band structure described above. Incorporating $\gamma_3 \approx 0.3$ eV generates so-called trigonal warping, which adds a term to the Hamiltonian similar to that of monolayer graphene [7]. This introduces four Dirac cones at low energies, one centered at the K (or K') point, and the other three offset in momentum so that the angles between them are 120°. Trigonal warping is relevant at carrier densities below about 10^{11} cm^{-2} [7]. The γ_4 hopping is expected to be about an order of magnitude smaller, but it leads to a slight increase in the mass of holes relative to that of electrons [8].

Even more interesting is the ability to modify the band structure of bilayer graphene by applying a perpendicular electric field [9–11]. This leads to a tunable band gap (Fig. 1.5b) whose magnitude is controlled by the magnitude of the electric field, which breaks layer (pseudospin) symmetry.

1.2 2DEGs in a Magnetic Field

When a perpendicular magnetic field B is applied to a 2DEG, the band structure changes dramatically. The effect of the magnetic field can be incorporated by making the transformation $\boldsymbol{p} \rightarrow \boldsymbol{p} + e\boldsymbol{A}$, where $\boldsymbol{A}$ is the vector potential and e is the absolute value of the electron charge. For non-relativistic 2DEGs with parabolic dispersion, this leads to a Hamiltonian analogous to a quantum harmonic oscillator [12]. The resulting energy levels

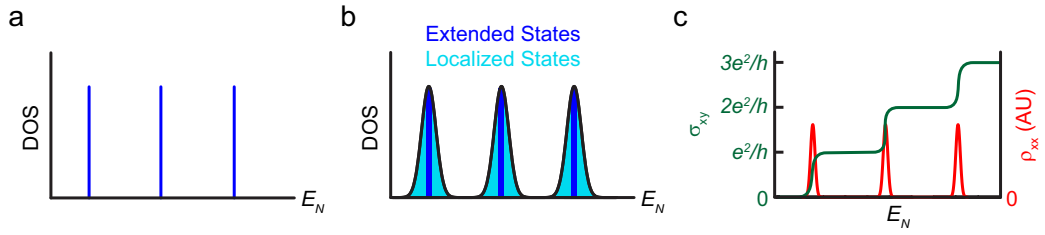

Figure 1.6: Landau levels in the limit of vanishing disorder (a) and including disorder (b). Dark blue regions correspond to extended states, which carry current across the sample. The cyan regions represent states that are localized in potential hills and valleys induced by disorder. (c) Schematic of the Hall conductivity and longitudinal resistivity in the quantum Hall regime. Plateaus in σ_{xy} and zeros in ρ_{xx} occur as the localized states are populated.

$E_N = \hbar\omega_c(N + 1/2)$, known as Landau levels (LLs) (Fig. 1.6a), each have a degeneracy of eB/h per unit area, where N is the orbital index and $\omega_c = eB/m^*$ is the cyclotron frequency. The nonrelativistic LL wavefunctions are given by a Gaussian prefactor multiplied by a Hermite polynomial.

1.2.1 Quantum Hall effect (QHE)

In contrast to the classical Hall effect known in three-dimensional materials, von Klitzing [1] found that for a 2DEG, the transverse (Hall) conductivity exhibits quantized plateaus of $\sigma_{xy} = \nu e^2/h$ around integer filling factors $\nu = nh/eB$, where n is the carrier density, and that concomitant dips occur in the longitudinal resistivity ρ_{xx} (Fig. 1.6c). This surprising behavior can be understood by considering the effect of (a small amount of) disorder on the LLs described above, pictured in Fig. 1.6b. Electrons perform fast cyclotron motion while drifting along equipotential contours. Near the center of a given LL, the electrons populate extended states which percolate through the bulk of the sample and contribute to conduction. In contrast, the broadened tails of the LLs involve electronic states localized to the hills and valleys of the disorder potential. As these states are populated, conduction only occurs through one-dimensional edge states formed when the confining potential at the

sample boundary causes the Fermi energy to intersect LLs that are fully populated in the bulk. No change in conductivity occurs as localized states are populated, giving rise to the pleateaus in σ_{xy}, and the conductivity of each edge mode, $G_0 = e^2/h$, sets the value of the quantization. Moreover, there are no low-energy states available for edge states to scatter into, so the current flow is dissipationless in the longitudinal direction, producing $\rho_{xx} = 0$.

It is worthwhile to note that one electronic state is filled (per LL) for each flux quantum $\phi_0 = h/e$ of the applied field. Naively, one might expect that the size of the localized states and the order in which they are populated is dictated solely by the single-particle disorder potential landscape. However, in practice, the population of localized states is strongly influenced by many-body screening [13]. As a consequence, localized states appear as diagonal lines in the n-B plane with a slope that is identical to their parent quantum Hall state. The density offsets of these states from their parents do not differ with magnetic field or filling factor, provided that the energy gaps and quasiparticle charge associated with the quantum Hall states have comparable magnitude.

1.2.2 QHE in Graphene

The quantum Hall effect in graphene is markedly different from that observed in conventional 2DEGs. In graphene, each electronic state has an additional fourfold degeneracy due to the spin and valley degrees of freedom. The Berry's phase of π adds to the phase accumulated by an electron performing cyclotron motion in a magnetic field, so the sequence of quantum Hall states is shifted by a half integer, and there is a LL at zero energy. Taken together, this means that the most prominent quantum Hall states in graphene occur at $\nu = \pm 4(M + 1/2)$, where M is a non-negative integer [14, 15], as illustrated in Fig. 1.7a.

The linear dispersion in graphene also leads to different LL energies compared to those in conventional 2DEGs. In graphene, the LL spectrum is given by $E_N = \pm v_F\sqrt{2e\hbar BN}$

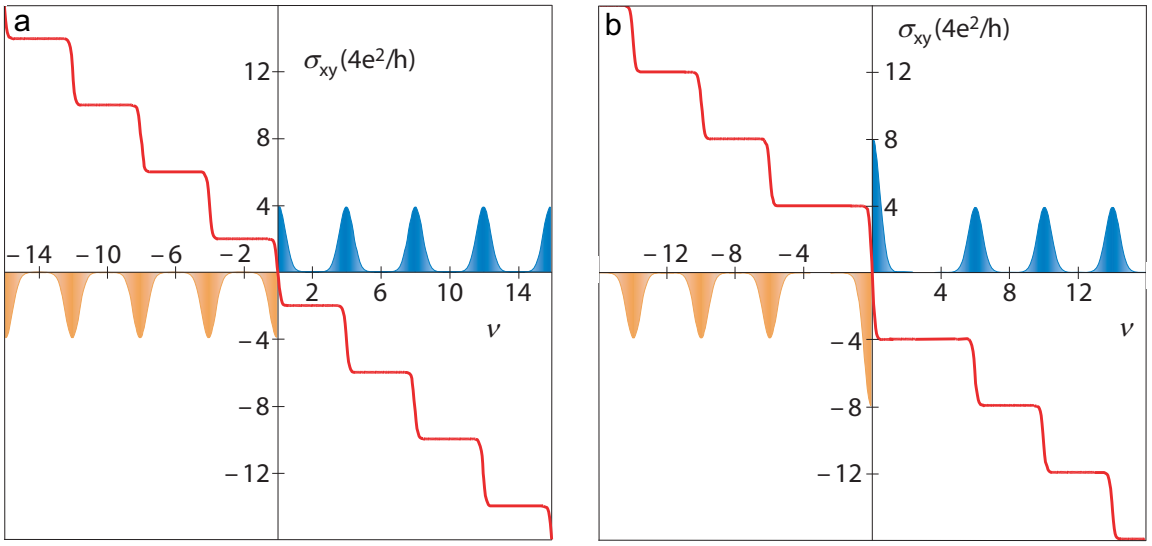

Figure 1.7: Quantum Hall effect in monolayer (a) and bilayer (b) graphene. Electron (blue) and hole (orange) density of states are shown as shaded regions. Quantum Hall plateaus occur at $\nu = \pm 4(M + 1/2)$ for monolayers and $\nu = \pm 4(M + 1)$ for bilayers. Figure adapted from ref. [16].

[14, 15]. Because the LL separation scales as $\sqrt{B}$, the ratio between LL separation and Coulomb energy is independent of magnetic field, unlike in conventional 2DEGs, where increasing the magnetic field can be used to minimize LL mixing. The $\sqrt{N}$ factor is also distinct from conventional 2DEGs, whose LL spacing does not depend on orbital index. Finally, it is worth noting that the lowest LL in graphene is special. It is made up of both electrons and holes, and for valley K (K'), the wavefunction is localized only on sublattice A (B). This is a specific case of the more general relation that for a particular valley, the N^{th} orbital wavefunction is given by $\Psi_N = (\psi_N, \psi_{N-1})$, where ψ_N is the N^{th} nonrelativistic LL orbital wavefunction. Similar to the zero-field case, the wavefunction components are reversed for the opposite valley.

1.2.3 QHE in Bilayer graphene

Bilayer graphene also supports a unique quantum Hall effect that is different from that of both monolayers and conventional 2DEGs. In bilayer graphene, the Berry's phase of 2π leads to the quantum Hall spectrum $E_N = \hbar\omega_c\sqrt{N(N-1)}$, and the most prominent quantum Hall features occur at $\nu = \pm 4(M+1)$ (Fig. 1.7b), where the factor of four is again due to spin and valley symmetry [16]. As in monolayers, the lowest LL in bilayer graphene is also centered at zero energy and contains both electrons and holes. It serves as an especially rich area for exploration because it includes both the $N = 0$ and $N = 1$ orbital states, yielding an overall eightfold degeneracy [7].

Also similar to monolayer graphene, the wavefunctions of each layer have different character for a given orbital index [7]. In the absence of an interlayer potential difference, the wave function of the N^{th} orbital state in a particular valley is given by $\Psi_N = (\psi_N, \psi_{N-2})$ for $N \geq 2$ (again, switching the valley reverses the components). In the lowest LL, the wavefunctions are $\Psi_0 = (\psi_0, 0)$ and $\Psi_1 = (\psi_1, 0)$; the sublattice, valley, and layer degrees of freedom are therefore all equivalent for this LL.

1.2.4 Symmetries in graphene

Compared to other 2DEGs, graphene possesses multiple underlying and intertwined symmetries, and it is worthwhile to summarize them here. In real space, it has a sublattice symmetry, which is typically referred to as pseudospin. In reciprocal space, there is a twofold valley (sometimes called isospin) symmetry between the K and K' points. Finally, electrons also have an SU(2) spin symmetry, and this combines with the valley degeneracy to form an approximate SU(4) symmetry. Bilayer graphene also hosts the same symmetries, except that the sublattice pseudospin corresponds to the layer degree of freedom. In addition,

the lowest LL in bilayer graphene exhibits an eightfold degeneracy because it includes the lowest two orbital states.

Several different physical effects can lift the symmetries described above to varying degrees. Perhaps the most straightforward is the Zeeman effect, which leads to a splitting $E_Z = g\mu_B B_{tot}$, where $g \approx 2$ is the g factor and μ_B is the Bohr magneton. Sublattice symmetry is robust in monolayer graphene (this is what protects the crossing bands at the Dirac points), but it can be lifted by a perpendicular electric field in bilayer graphene. An electric field also slightly breaks the $N = 0, 1$ orbital degeneracy by the amount $\Delta_{orbit} = U\hbar\omega_c/\gamma_1$ [17]. Finally, electron-electron interactions can also introduce symmetry-breaking terms, and these effects will be described in the following section.

1.3 Electron-Electron Interactions

Beyond the exotic single-particle behavior, graphene systems also provide a rich playground in which to explore many-body effects due to their many inherent symmetries. In this section, we explore the consequences of direct (Hartree) Coulomb repulsion

$$E_{dir} = \frac{1}{2}\int d\boldsymbol{r}d\boldsymbol{r'}V_C|\phi_1(\boldsymbol{r})|^2|\phi_2(\boldsymbol{r'})|^2, \tag{1.5}$$

and the exchange (Fock) energy

$$E_X = -\frac{1}{2}\int d\boldsymbol{r}d\boldsymbol{r'}V_C\phi_1^*(\boldsymbol{r})\phi_1(\boldsymbol{r'})\phi_2^*(\boldsymbol{r'})\phi_2(\boldsymbol{r}), \tag{1.6}$$

which is proportional to the overlap between electron wavefunctions for electrons with the same internal degrees of freedom [18]. Here, $V_C = e^2/4\pi\epsilon|\boldsymbol{r} - \boldsymbol{r'}|$ is the Coulomb potential, ϵ is the dielectric constant of the environment, and ϕ_i are the single-particle wavefunctions [18].

At zero field, wavefunction overlap can be loosely approximated to be proportional to the distance between particles, given by $n^{-1/2}$ [19]. Therefore, it becomes increasingly im-

portant as particle density is decreased. The non-vanishing density of states at the charge neutrality point in bilayer graphene make it especially susceptible to electron-electron interactions at zero field, and various types of correlated states have been studied theoretically [20–29]. These states and their experimental signatures are described in more detail in Chapter 3. In a magnetic field, the magnetic length $l_B = \sqrt{\hbar/eB}$ is the relevant distance to consider, and the Coulomb interaction energy scale is instead given by $E_c = e^2/4\pi\epsilon l_B$. In general, electron-electron interactions therefore scale as $\sqrt{B}$ and become increasingly important as the magnetic field increases.

1.3.1 Quantum Hall ferromagnetism

In systems with at least two degenerate LLs, spontaneous symmetry breaking can occur due to an exchange-driven phenomenon known as quantum Hall ferromagnetism [30]. When an integer number of LLs in the degenerate subspace are occupied, and in the limit of vanishing disorder, it becomes favorable to polarize the electronic degree(s) of freedom. For concreteness, we neglect Zeeman splitting below and use the electron spin as an example, but the conclusions are valid for any degree of freedom and for multicomponent systems.

At its most basic level, quantum Hall ferromagnetism can be understood as a consequence of the Pauli exclusion principle and Coulomb repulsion. Pauli exclusion guarantees that two electrons with the same spin must have a fully antisymmetric spatial wavefunction. Therefore, electrons with identical spin states will have minimal wavefunction overlap when compared to unpolarized electrons, and they will experience less Coulomb repulsion. If the corresponding gain in energy is larger than the cost in kinetic energy from occupying only one spin in the disorder-broadened LL, then the spins will all spontaneously polarize and an energy gap will develop. It is also worthwhile to note that the direction of polarization of the

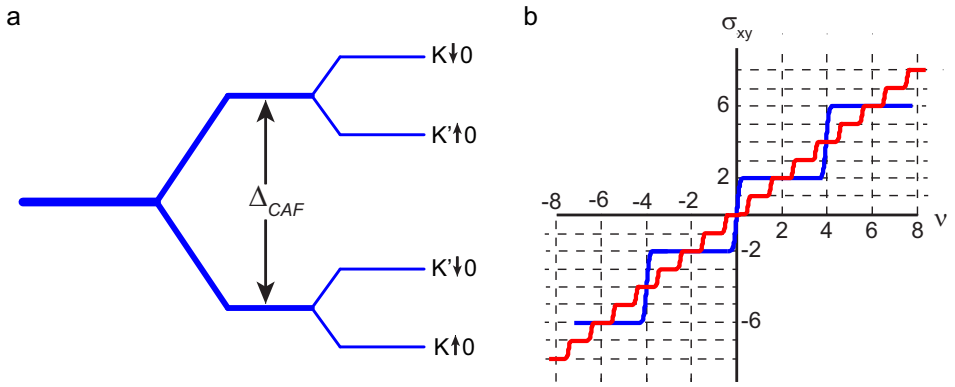

Figure 1.8: (a) Schematic diagram of the energy gaps that can arise in graphene from electron-electron interactions. The order of splitting depends on both intrinsic parameters and external fields; the canted antiferromagnet (CAF) $\nu = 0$ phase is shown. (b) The experimental signature of LL splitting is additional quantum Hall features at all integer filling factors (red curve). The blue curve shows the single-particle behavior in graphene.

broken-symmetry state may be chosen by single-particle effects, but exchange enhancement can still significantly increase the magnitude of the energy gap.

In graphene, any polarization in the SU(4) spin-valley subspace is possible (in principle), and for clean enough systems, quantum Hall states occur at all integer filling factors (Fig. 1.8). The order parameters of these states have been the subject of intense theoretical [30–33] and experimental [34–41] study, with special focus placed on the insulating $\nu = 0$ state at the charge neutrality point. In bilayer graphene, the $N = 0$ and $N = 1$ orbital states can also spontaneously polarize, fully lifting the eightfold degeneracy and producing quantum Hall plateaus at all integer multiples of e^2/h. The nature of each broken-symmetry state is discussed in more detail in Chapters 2, 3, and 6.

1.3.2 Valley anisotropy in graphene

Graphene systems are special in large part due to their approximate SU(4) spin and valley symmetry. This is distinct from GaAs-based 2DEGs, which only have a spin degree of freedom, and from other multicomponent 2DEGs such as Si and AlAs, where the

large g factor and effective mass lead to spin polarization at the single-particle level. Although Coulomb interactions in graphene are insensitive to spin and valley to first order, there are terms, known as valley anisotropies, which arise from short-range electron-electron [31, 42–44] and electron-phonon interactions [43–46] and lead to symmetry-breaking effects with important consequences for the nature of the $\nu = 0$ state. The valley anisotropies have characteristic energy scales given by e^2a/l_B^2, so their magnitude scales linearly with magnetic field, and they are significantly smaller than the SU(4)-symmetric Coulomb interactions. Depending on the sign and magnitude of each of the anisotropy terms, which can be strongly renormalized by LL mixing, several different broken-symmetry phases can be realized. Experimentally, recent measurements indicate that the canted antiferromagnet is favored at $\nu = 0$ in monolayer and bilayer graphene [47, 48], in contrast to the expectation of spin polarization in the absence of anisotropy terms.

1.3.3 Fractional quantum Hall effect (FQHE)

Incompressible quantum Hall states have also been observed at certain fractional filling factors in especially clean 2DEGs [2]. This behavior is known as the fractional quantum Hall effect (FQHE), and the strongest states follow the pattern

$$\nu = \frac{p}{2mp \pm 1}, \tag{1.7}$$

where m and p are integers. Soon after its experimental discovery, theoretical explanations of the FQHE in terms of interacting electrons were put forward [49, 50]. Remarkably, the quasiparticles associated with these states carry fractional charge [51], even though they arise due to correlations between electrons.

An intuitive mean-field framework with which to understand the FQHE is the composite fermion (CF) model [52]. The basic idea is to transform a system of strongly interacting

electrons into one of weakly interacting quasiparticles known as CFs. Within composite fermion theory, electrons capture an even number $2m$ of flux quanta (strictly speaking, vortices rather than flux quanta; the magnetic field is homogeneous), and these composite particles feel a reduced magnetic field given by $B^* = B - 2mn\phi_0$. CFs experience zero effective magnetic field at $\nu = 1/2m$, and any deviation from this filling factor acts as an effective magnetic field B^*. Like electrons in a magnetic field, the CFs form a sequence of flat energy bands separated by energy gaps. These are called Λ levels (ΛLs), and they are CF analogues of LLs that can each hold nh/eB^* CF states. As density or magnetic field changes, the number of occupied ΛLs changes, and if the CF filling lies between ΛLs, a quantum Hall state emerges. Integer numbers of ΛLs are occupied at exactly the fractional filling factors from Eq. 1.7. Therefore, the FQHE of electrons can be understood to arise from the integer quantum Hall effect of CFs.

Like electrons, composite fermions have internal degrees of freedom. In monolayer and bilayer graphene, the spin, valley, and orbital index of CFs play an important role in both the sequence and nature of the observed FQH states [53–55]. These effects are explored in detail in Chapters 4-6.

1.4 Electronic Compressibility

Most studies of quantum Hall physics have focused on electronic transport due to the simplicity of the measurements and their unambiguous experimental signatures. However, transport is dominated by the extended states that carry electronic current, and sample inhomogeneity can obscure underlying behavior in the presence of moderate disorder. Many of the experiments in this thesis instead rely on locally measuring a different quantity, the inverse electronic compressibility $\kappa^{-1} = n^2 d\mu/dn$. Inverse compressibility (hereafter, we

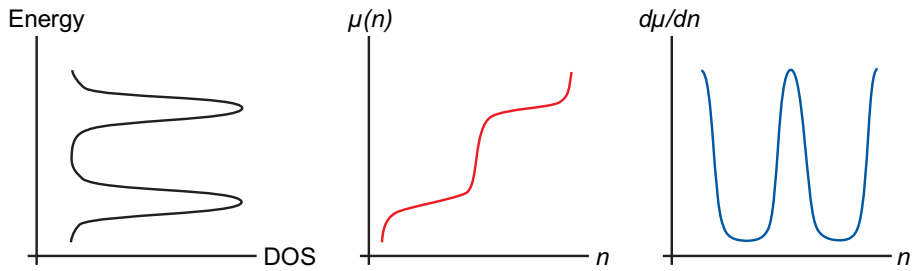

Figure 1.9: Schematic showing the relationship between disorder-broadened LLs, the chemical potential, and the inverse compressibility. Incompressible peaks occur any time there is an energy gap or a decreased density of states. Figure adapted from the original version created by Jens Martin.

drop the prefactor and use this term to mean $d\mu/dn$) provides a thermodynamic measurement of the behavior in the bulk of the sample. It is especially well-suited to the study of quantum Hall systems, where the bulk is insulating when the Fermi energy lies between LLs, resulting in incompressible peaks, as shown in Fig. 1.9. Electronic compressibility measurements serve as a powerful tool because the strongest signals occur when there is an energy gap or decreased density of states, and the technique is sensitive to both single-particle and many-body effects. Below, we describe the physics of single-electron transistors (SETs) and the experimental implementation that we use to measure the local electronic compressibility.

1.4.1 Single-electron transistor (SET)

A single-electron transistor consists of a quantum dot (the 'island') separated by tunnel junctions to source and drain electrodes. The energies of the electronic states on the island can be controlled by capacitive coupling C_g to a nearby gate. Their spacing is determined by two factors: the energies of the quantum dot eigenstates, and the charging energy $E_{chg} = e^2/2C$, where $C = C_s + C_d + C_g$ is the total capacitance to the source, drain, and gate electrodes [56]. For metallic islands (this is the regime of the experiments in this thesis),

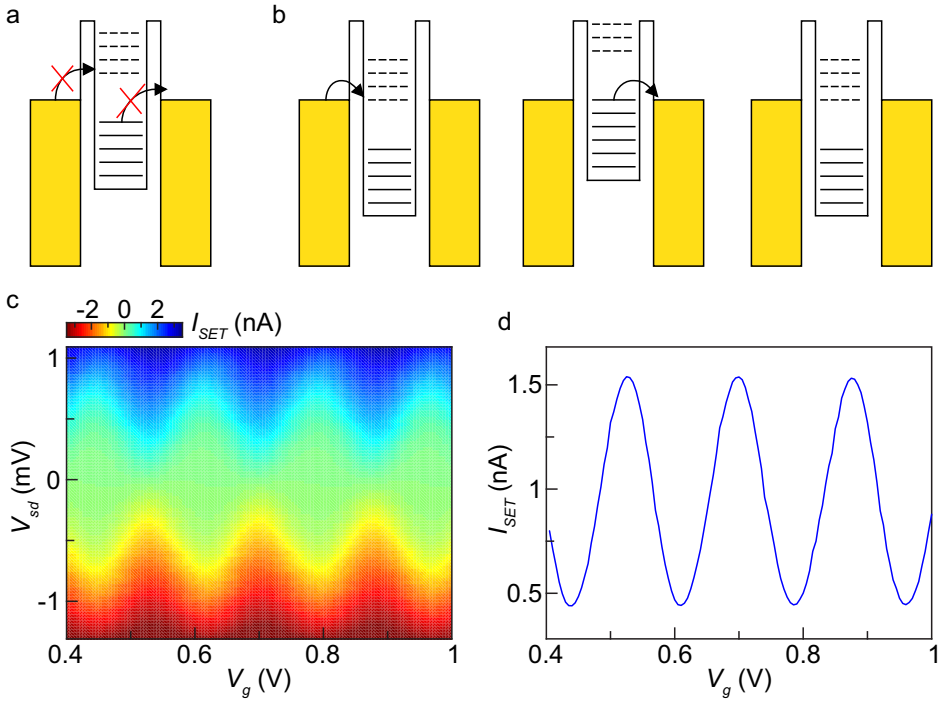

Figure 1.10: (a) Blockaded regime, in which the Fermi energy of the leads does not allow electrons to hop onto or off of the island (black arrows) at low temperature. (b) Conducting regime, in which an electron can hop onto the island from the source and off of it onto the drain. (c) Current as a function of source-drain bias V_{sd} and gate voltage V_g. Coulomb diamonds of low current are visible at low V_{sd}. (d) Current through the SET at $V_{sd} = 0.55$ V as a function of gate voltage showing Coulomb blockade oscillations. Each oscillation corresponds to changing the charge on the island by one electron.

the energy levels of the quantum dot can be ignored, and the behavior is dominated by the charging energy associated with adding or removing an electron from the island.

If the temperature is lower than the charging energy, then the passage of current from source to drain is either allowed or blocked, depending on the relative Fermi energies of each component. The two key cases are schematically illustrated in Figs. 1.10a,b. When an electronic state is aligned with the Fermi energies of the electrodes such that an electron can both hop from the source to the island and from the island to the drain, the SET is conducting. In contrast, if the temperature and source-drain bias are too small to allow one of these steps, current is blocked, a phenomenon known as Coulomb blockade.

Alternatively, if we assume that charge is quantized, this behavior can be described in terms of the free energy of electrons on the island, a parabola given by

$$E(Q) = (Q)^2/2C - QV, \tag{1.8}$$

where V is the external potential felt by the SET [56]. The minimum of this parabola occurs when $Q = CV$; when this charge corresponds to an integer number of electrons, the charge on the island is fixed and current cannot flow. In contrast, if Q corresponds to a half-integer, both $Q - e/2$ and $Q + e/2$ are degenerate in energy, so the number of electrons on the island can fluctuate, and current can flow. The current through the SET is therefore an oscillatory function of the external voltage (Figs. 1.10c,d), and each full period corresponds to adding an extra electron to the island. Measuring the current through the SET then acts as an especially sensitive measure of the local electrostatic potential.

1.4.2 Measurement setup

The measurement configuration that we use to determine inverse compressibility is based on a technique originally developed by Eisenstein [19, 57]. In contrast with earlier capacitive techniques, which suffered from a comparatively small and difficult-to-quantify signal due to the background geometric capacitance, we use a field-penetration technique in which a third component (the SET) is used to measure the electric field that penetrates through a 2DEG of interest in response to a change in gate voltage.

We hold the electrochemical potential $\Phi = \mu + eV$ of the sample fixed. In equilibrium, this means that any changes in the chemical potential μ of the sample induce corresponding changes in the electrostatic potential V, and we can therefore use the SET to measure the chemical potential. Changing the gate voltage controls the charge density of the sample, and monitoring the response of current through the SET as a function of gate voltage allows us to determine the inverse compressibility $d\mu/dn$.

The detailed measurement schematic is illustrated in Fig. 3.1a, as well as several other figures throughout the thesis, so it is not reproduced here. We apply a small (few mV) bias V_{SET} across the SET, and monitor the output current I_{SET} after it goes through a current amplifier. We control the carrier density of the sample using a dc voltage applied to the back gate V_{bg}, and we also add a small ac excitation to mitigate low-frequency noise. Monitoring the SET current response I_{bg} to the the ac back gate excitation and normalizing it by the slope of the Coulomb blockade oscillation allows us to extract the inverse compressibility, $d\mu/dn$. We simultaneously measure this slope by monitoring the current response I_{2D} of the SET to an ac excitation V_{2D} between tip and sample. Finally, in order to minimize doping of the sample caused by the tip, we also apply a dc tip-sample bias to account for the work function difference between the two materials. Taken together, this scheme probes $d\mu/dn$:

$$\frac{dI_{bg}}{dV_{bg}}/\frac{dI_{2D}}{dV_{2D}} = \frac{C}{e}\frac{dI_{bg}}{dn}\frac{dV_{2D}}{dI_{2D}} = -\frac{C}{e^2}\frac{d\mu}{dn} \tag{1.9}$$

We use a feedback circuit to maintain the current at the maximum sensitivity point of the Coulomb blockade oscillation. This involves changing V_{2D} to compensate any change in μ while maintaining $(V_{bg}-V_{2D})$. Monitoring V_{2D} therefore provides a direct dc measurement of $\mu(n)$. While noisier than the ac technique, the higher frequency associated with the latter causes artificial enhancement of $d\mu/dn$ if the sample is very resistive, because the sample cannot fully charge.

The measurements presented in this thesis were performed in a scanning SET microscope in which an SET is evaporated on a quartz rod and is mounted on a scanning probe microscope head. Tip fabrication details, as well as other tips and tricks for operation are provided in Appendix B.

1.5 Outline of This Thesis

The remainder of this thesis is grouped into several major themes. Chapters 2 and 3 describe electronic transport and compressibility measurements of broken-symmetry integer quantum Hall states in suspended bilayer graphene. Chapter 3 also presents evidence for a correlated electronic state at zero electric and magnetic field. Chapters 4 and 5 discuss scanning SET measurements that illustrate the impact of spin and valley symmetry on FQH states in suspended monolayer graphene. In Chapter 6, we describe compressibility measurements of FQH states in bilayer graphene on boron nitride. Finally, Chapter 7 presents preliminary results regarding the behavior at the interface between monolayer and bilayer graphene. Sample and SET fabrication details are included as Appendices A and B.

Chapter 2

Broken-Symmetry States and Divergent Resistance in Suspended Bilayer Graphene

Monolayer and bilayer graphene have generated tremendous excitement, owing to their unique and potentially useful electronic properties [6]. Suspending single-layer graphene flakes above the substrate [58,59] has been shown to greatly improve sample quality, yielding high-mobility devices with little charge inhomogeneity. Here we report the fabrication of suspended bilayer graphene devices with very little disorder. We observe quantum Hall states that are fully quantized at a magnetic field of 0.2 T, as well as broken-symmetry states at intermediate filling factors $\nu = 0, \pm 1, \pm 2$, and ± 3. In the $\nu = 0$ state, the devices show extremely high magnetoresistance that scales as magnetic field divided by temperature. This resistance is predominantly affected by the perpendicular component of the applied field, and the extracted energy gap is significantly larger than expected for Zeeman splitting.

These findings indicate that the broken-symmetry states arise from many-body interactions and underscore the important role that Coulomb interactions play in bilayer graphene.

2.1 Introduction

The linear dispersion of graphene near its Fermi energy gives rise to low-energy excitations that behave as massless Dirac fermions [6]. These quasiparticles show an anomalous integer quantum Hall effect [14, 15] in which the Hall conductivity is quantized at values of $\sigma_{xy} = \nu e^2/h$ for filling factors $\nu = \pm 4(M + 1/2)$. Here, M is a non-negative integer, e is the electron charge, h is Planck's constant, and the factor of four is due to spin and valley degeneracy. Recent measurements [38, 39] of graphene monolayers in high magnetic field B have revealed broken-symmetry quantum Hall states at $\nu = 0, \pm 1$, and ± 4, which have been proposed to arise from quantum Hall ferromagnetism [30, 31] or the formation of excitonic energy gaps [32, 33]. The $\nu = 0$ state has received particular attention owing to contradictory experimental observations. Some samples show large magnetoresistance of $\sim 10^5 - 10^7$ Ω near the charge-neutrality point [34–37], and this behavior has been ascribed to the opening of a spin gap [34], the approach of a field-induced Kosterlitz-Thouless transition to an insulating state [35, 36] or the formation of a collective insulator [37]. Others, however, report resistance of only $\sim 10^4$ Ω [38–40], and attribute their findings to the existence of spin-polarized counterpropagating edge modes [38, 40].

Although experimental investigations of broken-symmetry quantum Hall states have so far focused only on graphene monolayers, recent theoretical studies have investigated excitonic condensation [60] and quantum Hall ferromagnetism [17] in bilayer graphene and the resultant ground states at intermediate filling factors [61]. The physics is richer in bilayers owing to an extra twofold orbital degeneracy in the Landau level (LL) spectrum [16],

which leads to an eightfold-degenerate LL at zero energy and a corresponding step of $8e^2/h$ in σ_{xy}. It has been shown both theoretically [7] and experimentally [10,11] that a potential difference between the two layers opens an energy gap, leading to a plateau in σ_{xy} at $\nu = 0$, but no other broken-symmetry states have been observed. Here we report the fabrication of high-quality suspended bilayer graphene devices (Figs. 2.1a,b) that show full splitting of the eightfold-degenerate zero-energy LL. The $\nu = 0$ state emerges at $B \approx 0.1$ T and is characterized by an extremely large resistance that increases exponentially with the perpendicular component of B. The $|\nu| = 2$ states emerge at $B = 0.7$ T, and all symmetries are broken for $B > 3$ T.

2.2 Zero-Field Electronic Transport

We focus first on the behavior of the samples in zero magnetic field. Figure 2.1c shows the resistivity ρ of two suspended bilayers as a function of carrier density n. Each sample shows a sharp peak in ρ with a full-width at half-maximum on the order of 10^{10} cm^{-2}, comparable to that of suspended monolayer devices [58, 59] and an order of magnitude smaller than that of unsuspended bilayers [62]. In all samples, the peak lies close to zero back-gate voltage ($|V_{peak}| < 0.5$ V), indicating that there is little extrinsic doping in our devices. As a measure of sample cleanliness, we can estimate the magnitude of carrier-density fluctuations δn on the basis of the carrier-density dependence of the conductivity $\sigma(n)$, shown in Fig. 2.1d. Near the charge-neutrality point, local variations in potential lead to the formation of electron-hole puddles [63], and $\sigma(n)$ is expected [64] to remain constant in this regime because $|n| < \delta n$. In our suspended bilayers, δn is typically on the order of 10^{10} cm^{-2}, and it reaches as low as 10^9 cm^{-2} in sample S3.

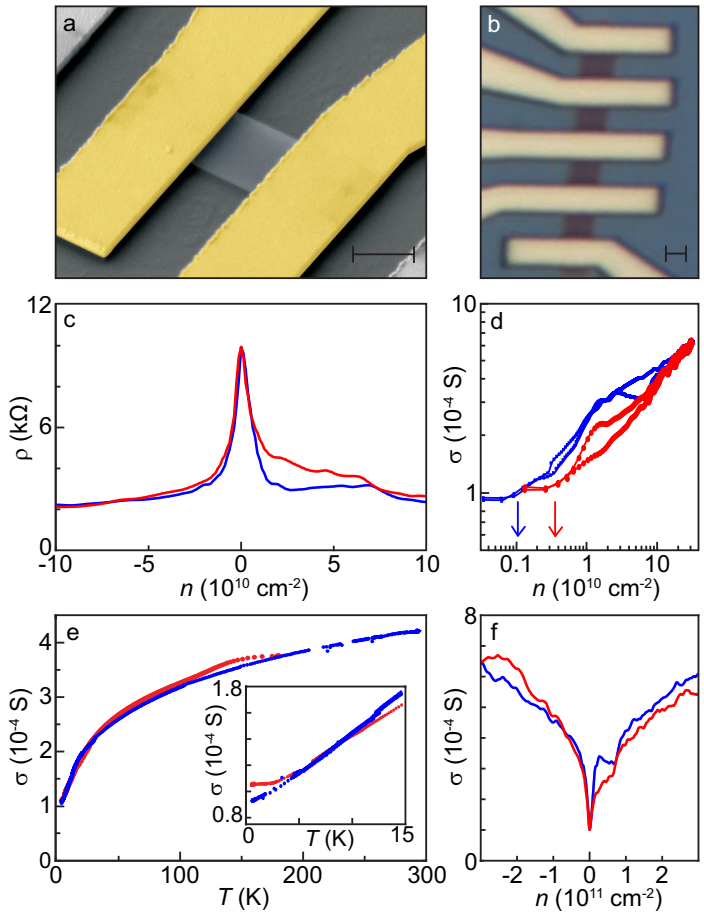

Figure 2.1: Characterization of suspended bilayer samples S3 (blue) and S4 (red) at zero magnetic field. (a) False-color scanning electron micrograph of a typical suspended bilayer graphene flake. (b) Optical microscope image of several two-terminal suspended bilayer samples in series. The scale bars are 1 μm. (c) Two-terminal resistivity ρ as a function of carrier density n. Both samples show a pronounced peak in ρ with full-width at half-maximum of 1.5×10^{10} cm^{-2} and 2×10^{10} cm^{-2}, respectively, at temperature $T = 450$ mK. (d) Electron and hole branches of the conductivity σ. The width of the plateau in σ, marked by the arrows, indicates the magnitude of carrier-density fluctuations due to disorder. (e) Temperature dependence of the minimal conductivity σ_{min}. Inset: Zoom-in on the low-temperature behavior. For sample S4, disorder causes σ_{min} to saturate for $T < 2$ K. The decrease of σ_{min} for sample S3 down to 450 mK indicates that it is cleaner, consistent with the findings in (c) and (d). (f) Conductivity at $T = 450$ mK. For $n > 2 \times 10^{11}$ cm^{-2}, the mobility is about 7,500 cm^2 V^{-1} s^{-1}. The pronounced dip in the conductivity at very low densities may be enhanced by a disorder-induced gap.

The temperature dependence of the minimum conductivity σ_{min} (Fig. 2.1e) provides a second method to estimate δn. At low temperatures, σ_{min} is dominated by transport through the electron-hole puddles rather than thermal effects, so we expect strong temperature dependence only for $k_B T > E_{pud}$, where k_B is Boltzmann's constant and E_{pud} is the typical magnitude of the screened potential fluctuations responsible for electron-hole puddles. For bilayer graphene, we can estimate $E_{pud} \approx h^2 \delta n / 8\pi m^*$, where $m^* \approx 0.042 m_e$ is the effective mass in bilayer graphene [7] (m_e is the electron mass). In sample S3, σ_{min} shows temperature dependence down to 450 mK, providing an upper bound of $\delta n < 1.33 \times 10^9$ cm^{-2}. In contrast, σ_{min} saturates at approximately 2 K in sample S4, corresponding to $\delta n \approx 6 \times 10^9$ cm^{-2}. Both estimates are consistent with the estimate of disorder obtained from $\sigma(n)$. In both samples, σ_{min} at 450 mK is a few times the conductance quantum, in good agreement with theoretical predictions for its intrinsic limit [65, 66].

In contrast to the typically reported linear behavior in bilayer graphene, $\sigma(n)$ is sublinear in suspended samples (Fig. 2.1f). If we assume mobility $\mu = (1/e) d\sigma/dn$, then μ typically ranges from 10,000 to 15,000 cm^2 V^{-1} s^{-1} in our suspended bilayers at carrier densities of 2-3 $\times 10^{11}$ cm^{-2}. These numbers represent a modest improvement of approximately a factor of two over unsuspended bilayers, but it remains unclear why the mobility is this low given the indications of sample quality discussed above, the low magnetic field at which we observe quantum Hall plateaus and the high mobilities observed in suspended monolayers [58, 59]. It is predicted [64] that the mobility of bilayer graphene should be more than an order of magnitude smaller than that of monolayer graphene. This discrepancy was not observed in unsuspended samples [62], but mobility in such samples may be limited by disorder associated with the substrate. It is also worthwhile to comment on the possibility that the sharp dip in conductivity at low n is enhanced by a small energy gap that opens owing to disorder-induced differences in carrier density between the top and bottom layers

of the flake [17]. Differences in density of a few times 10^9 cm^{-2} would lead to an energy gap of approximately 0.05 meV [10].

2.3 Broken-Symmetry Quantum Hall States

We next discuss the magnetic-field-dependent behavior of the samples. Figures 2.2a,b show the conductance of sample S1 as a function of magnetic field and carrier density $G(n, B)$, and Fig. 2.3a highlights traces of $G(n, B)$ at several representative magnetic fields. The devices show the expected quantum Hall conductance plateaus at $4(M + 1)e^2/h$ for bilayer graphene, corresponding to filling factors $\nu = \pm 4(M + 1)$. Full quantization for $\nu = \pm 4$ occurs at very low B, indicative of the cleanliness of the devices. In sample S3, the $\nu = \pm 4$ plateaus are fully quantized at 0.2 T (Fig. 2.3b, inset).

As well as the expected behavior highlighted above, we observe quantum Hall plateaus corresponding to intermediate filling factors $\nu = 0, \pm 1, \pm 2$, and ± 3. The $|\nu| = 2$ (1) state becomes apparent at 0.7 (2.7) T, and fully develops into a conductance plateau of $2e^2/h$ (e^2/h) at 2.7 (7.3) T on the hole side (Figs. 2.2a and 2.3b). The $|\nu| = 3$ state emerges at a similar magnetic field to the $|\nu| = 1$ state, but leaves the experimentally accessible regime before it is fully quantized. Near the charge-neutrality point, a $\nu = 0$ state with a very large resistance that increases exponentially with B emerges at $B \approx 0.1$ T. Measurements of Hall bar devices show a corresponding plateau at $\sigma_{xy} = 0$ and rule out the possibility that the large resistance arises from contact resistance between the graphene and the electrical leads. We focus, however, on two-terminal devices because they are more homogeneous (see Section 2.6).

The appearance of quantum Hall states at $\nu = 0, \pm 1, \pm 2$, and ± 3 indicates that the eightfold degeneracy of the zero-energy LL in bilayer graphene is completely lifted. The

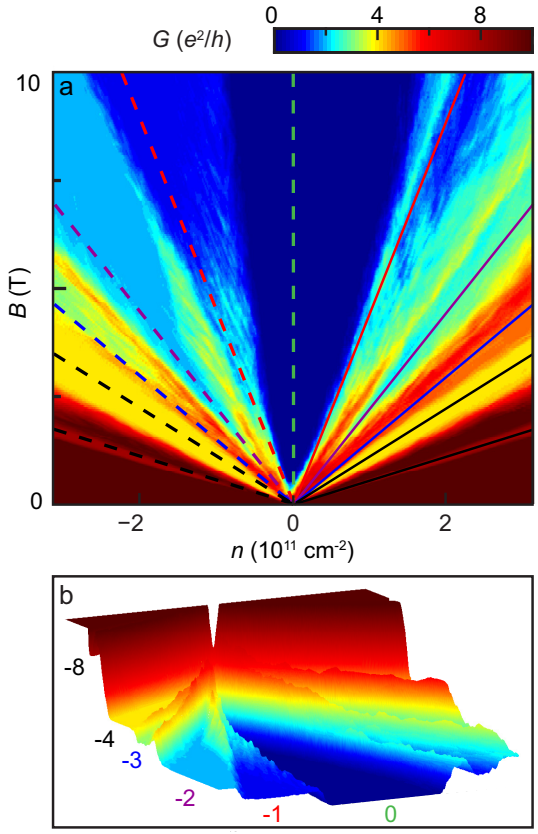

Figure 2.2: Splitting of the eightfold-degenerate Landau level in suspended bilayers. (a) Carrier-density and magnetic-field dependence of the two-terminal conductance $G(n, B)$ in sample S1 at $T = 100$ mK. Lines indicate filling factors $|\nu| = 8$ and 4 (black), 3 (blue), 2 (purple), 1 (red) and 0 (green). The conversion between back-gate voltage and density for each sample was calibrated using this type of measurement. (b) 3D rendering of $G(n, B)$ in sample S1. The numbers indicate filling factor. Broken-symmetry states at $\nu = 0, \pm 1, \pm 2$, and ± 3 are clearly visible.

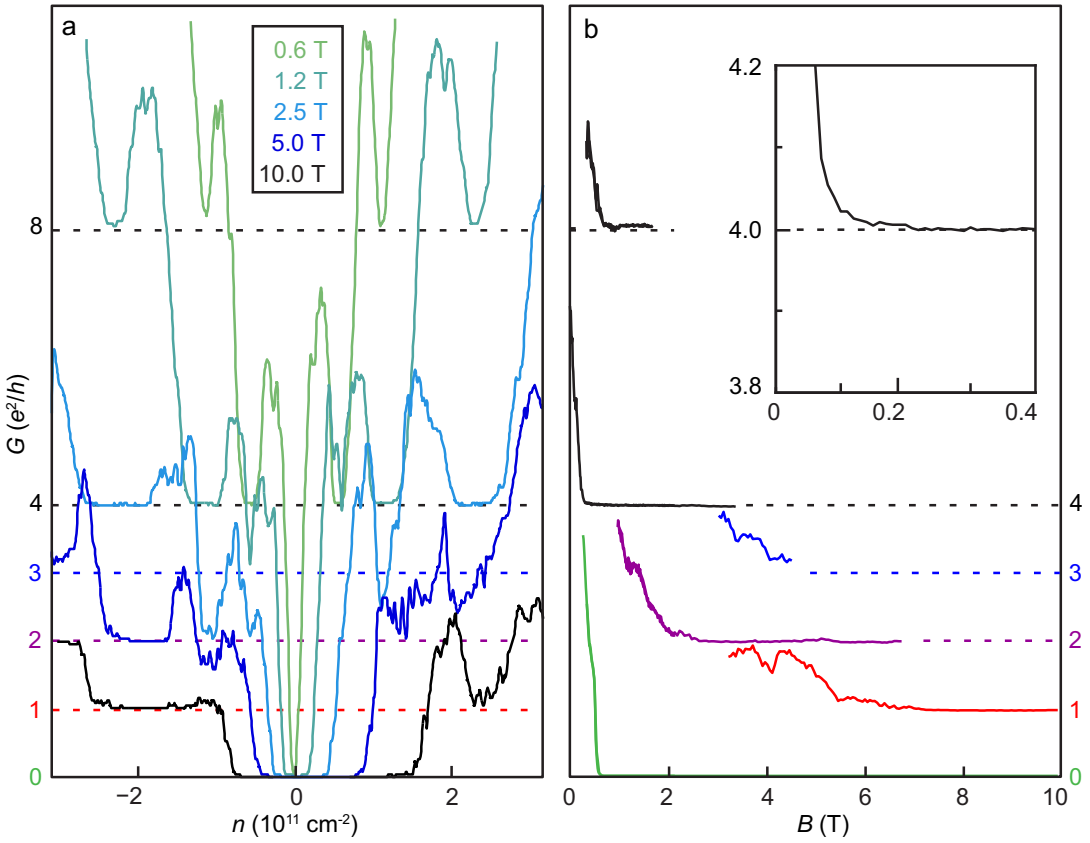

Figure 2.3: Quantization of states as a function of magnetic field. (a) Line traces of $G(n, B)$ at various magnetic fields. Quantum Hall plateaus associated with the broken-symmetry quantum Hall states are apparent. (b) Conductance traces taken along the dotted lines in Fig. 2.2a. For sample S1, full quantization is observed at $B = 0.4$ T for $\nu = 4$, $B = 2.7$ T for $\nu = 2$ and $B = 7.3$ T for $\nu = 1$. Inset: For sample S3, quantization of the $\nu = 4$ state is reached for $B = 0.2$ T at $T = 450$ mK.

magnetic field at which these effects emerge is over an order of magnitude smaller than has been reported for monolayers [34–40]. Broken-symmetry states could arise from several causes, including spin splitting due to the Zeeman effect [34], strain-induced lifting of valley degeneracy [67], the opening of an energy gap due to a potential difference between the two layers, or Coulomb interactions [17, 60]. In our samples, the proximity of V_{peak} to zero back-gate voltage makes it unlikely that we observe an energy gap due to chemical doping [10]. It has recently been shown [68] that large-scale ripples appear in suspended graphene membranes when they are cooled from 600 to 300 K, but room-temperature scanning electron micrographs of our suspended flakes do not show prominent corrugations (Fig. 2.1a). The interaction energy due to Coulomb effects in bilayer graphene is expected to be two orders of magnitude stronger than spin splitting caused by the Zeeman effect [17,60], so the observed broken-symmetry states are unlikely to be associated with Zeeman splitting. We therefore tentatively attribute the symmetry breaking to Coulomb interactions. The order in which broken-symmetry states emerge in our samples is indeed consistent with the expectations of Barlas *et al.*, who predict [17] the largest energy gap for a spin-polarized state at $\nu = 0$, followed by spin- and valley-polarized states at $|\nu| = 2$ and finally spin-, valley- and LL-index-polarized states at $|\nu| = 1$ and $|\nu| = 3$.

2.4 Resistance at $\nu = 0$

We now discuss in more detail the large magnetoresistance of the $\nu = 0$ state. Figure 2.4 shows the maximum resistance of sample S3 in a small carrier density range around the charge neutrality point as a function of magnetic field and temperature, $R_{max}(B, T)$ at various temperatures between 450 mK and 24.5 K (see also Section 2.6). $R_{max}(B, T)$ increases by more than four orders of magnitude to 10^8 Ω (the *de facto* limit of our measurement

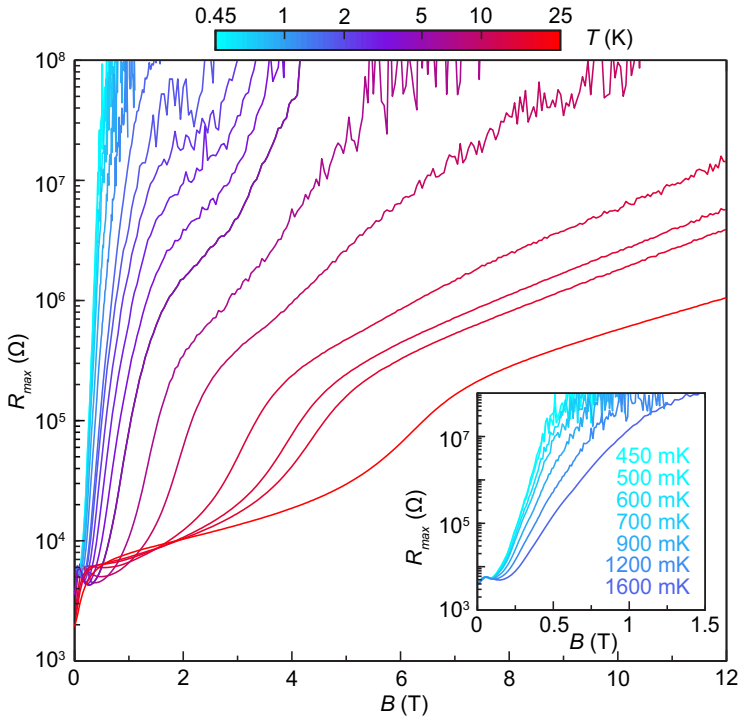

Figure 2.4: Maximum resistance of sample S3 at the charge-neutrality point as a function of magnetic field and temperature. Inset: Zoom-in on the low-temperature curves. We do not observe saturation of the resistance for temperatures down to 450 mK.

capabilities) within a few Tesla for $T < 5$ K. This increase is significantly steeper than in monolayers, where the reported [36] resistance reached only 40 MΩ at 30 T. The data do not fit a Kosterlitz-Thouless-type transition, nor do the flakes show activated behavior over the full temperature range of the measurements.

One of the main findings of this report is that $R_{max}(B,T)$ scales as B/T, as plotted in Fig. 2.5a. For $T \geq 1.9$ K, the data collapse rather nicely onto one curve. At lower temperatures, $R_{max}(B,T)$ continues to increase with decreasing T, but it does not do so as quickly as expected for B/T dependence (Fig. 2.5a, inset). This can be explained if we assume that the LLs are broadened by disorder. In such a scenario, a constant offset in magnetic field B_{off} is needed to resolve distinct quantum Hall states. Using $B_{off} = 0.14$ T, in reasonable agreement with the field at which the $|\nu| = 4$ states become fully quantized

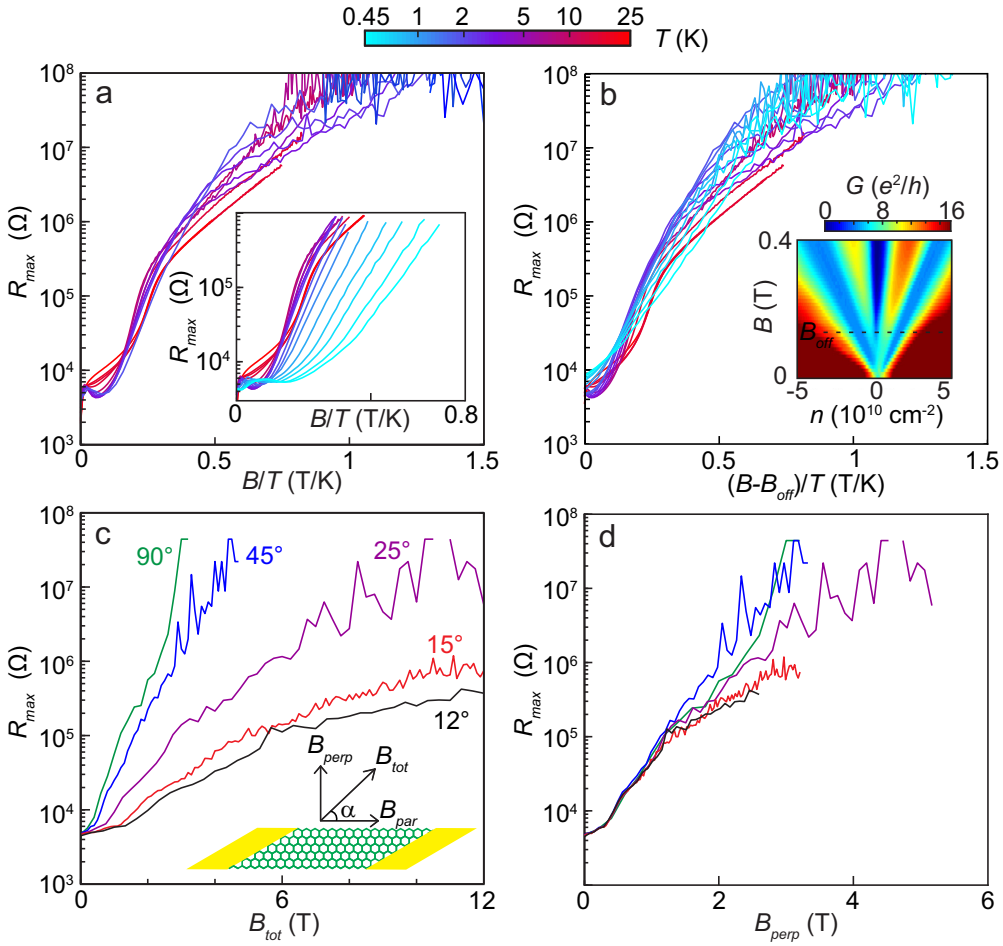

Figure 2.5: Scaling of the maximum resistance in the $\nu = 0$ state. (a) $R_{max}(B,T)$ of sample S3 plotted versus B/T. The data collapse onto one curve for temperatures $T > 1.9$ K. Inset: B/T scaling does not succeed for $T < 1.9$ K. (b) $R_{max}(B,T)$ versus $(B - B_{off})/T$. All data collapse using $B_{off} = 0.14$ T, which arises owing to disorder in the bilayer. Inset: Two-terminal conductance as a function of density and magnetic field. B_{off} coincides with quantization of the $\nu = \pm 4$ plateaus and the emergence of the $\nu = 0$ state. (c) $R_{max}(B,T)$ of sample S2 as a function of total applied magnetic field for several angles α between sample and field. Inset: Schematic showing the relative orientation between field and sample. (d) $R_{max}(B,T)$ as a function of the perpendicular component of the magnetic field for the same angles as in (c). The resistance depends primarily on B_{perp}, contradicting the expected behavior for a Zeeman gap.

and the $\nu = 0$ resistance begins to diverge (Fig. 2.5b, inset), the $R_{max}(B,T)$ data collapse onto one curve for the entire temperature range when plotted against $(B - B_{off})/T$ (Fig. 2.5b).

We infer that an energy gap $\Delta/2 \approx 0.3-0.9(B[\mathrm{T}])$ meV develops in an applied magnetic field. The gap is several times larger than expected for Zeeman splitting, and tilted-field experiments provide further evidence that the broken-symmetry states probably arise from many-body effects rather than Zeeman splitting. $R_{max}(B,T)$ is primarily dictated by the perpendicular component of field B_{perp} (Figs. 2.5c,d), in stark disagreement with the behavior expected for a Zeeman gap. Moreover, at fixed B_{perp}, an increase in the parallel component of the field reduces $R_{max}(B,T)$ (Fig. 2.5d), indicating that the low-energy excitations of the $\nu = 0$ state are not skyrmionic spin flip in nature [61]. The linear dependence of Δ on B is qualitatively different from what is expected for quantum Hall ferromagnetism and magnetic catalysis, which both predict [17, 60, 69, 70] a gap that scales as $B^{1/2}$. It is worth noting, however, that early studies [71] of the exchange-enhanced spin gap at $\nu = 1$ in GaAs samples also showed an energy gap that was linear in B. Coulomb interactions are predicted [17,60] to generate $\Delta \sim 100$ meV for magnetic fields of a few Tesla, far larger than we observe, but this discrepancy is probably due to disorder in our samples.

Acknowledgements

We would like to acknowledge discussions with L. S. Levitov, R. Nandkishore, D. A. Abanin, A. H. Castro Neto, A. H. MacDonald, M. S. Rudner and S. Sachdev. We acknowledge support from Harvard NSEC, the ONR MURI program and Harvard CNS, a member of the NNIN, which is supported by the NSF.

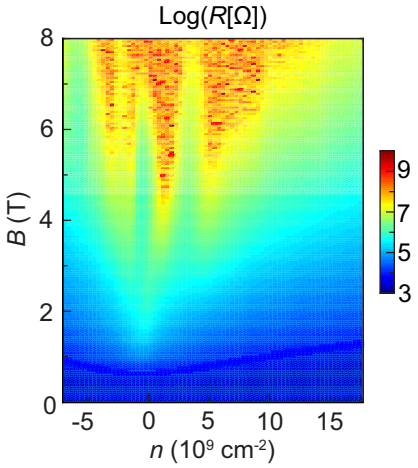

Figure 2.6: Resistance on a log scale as a function of magnetic field and carrier density at 4.5 K for sample S3 in a small density range around the charge neutrality point. Oscillations in resistance that are several orders of magnitude are visible as carrier density n is varied. These features occur at constant n as magnetic field is varied.

2.5 Methods

Fabrication of suspended bilayer graphene is described in Appendix A. Electronic transport measurements were made on multiple samples using standard ac lock-in techniques with excitation voltages below 100 μV, in either an ultrahigh-vacuum ^{3}He cryostat or a dilution refrigerator. The Si substrate serves as a global back gate, which is used to vary the carrier density in the bilayer. Back-gate voltage is limited to $|V_{bg}| < 10$ V to avoid structural collapse of suspended devices.

2.6 Supplementary Discussion

2.6.1 Resistance in the $\nu = 0$ State

Figure 2.6 shows $\log[R(n, B, 4.5\text{ K})]$ for sample S3 in a narrow range of carrier density around the charge neutrality point. For $B > 4$ T, $R(n, B, 4.5\text{ K})$ changes by several orders of magnitude as n is varied within the highly resistive region. These oscillations are

repeatable, and we find that the regions of relatively low and high resistance are approximately constant in n. It is also apparent from Fig. 2.6 that the highly resistive region is asymmetric: it extends to higher densities for electrons than for holes. Both the oscillations in $R(n, B,$ 4.5 K) and the electron-hole asymmetry have been observed in multiple samples. Their origin is unclear but disorder and/or systematic effects from the fabrication process remain likely candidates. We also note that the position of the peak resistance $R_{max}(B,T)$ shifts slightly (< 50 mV) in back gate voltage V_{bg} as B is varied. We therefore use $R_{max}(B,T)$ rather than the resistance at a constant value of V_{bg} to follow the evolution of the $\nu = 0$ state.

In addition to the gap size Δ that we obtain from the behavior of $R_{max}(B,T)$, we can obtain an independent estimate by measuring the width in carrier density of the highly resistive region and converting to energy according to $E = h^2 n/8\pi m^*$. As shown in Fig. 2.2a, the width of this region is approximately linear in B, as expected from the behavior of $R_{max}(B,T)$. Further, we obtain an estimate that $\Delta \approx 0.7(B[\mathrm{T}])$ meV, in good agreement with our prior findings from the measurements of $R_{max}(B,T)$. We note, however, that this second estimate of Δ is not fully rigorous because Landau level formation must be accounted for at large magnetic fields, changing the effective conversion between energy and density.

2.6.2 Hall Bar Devices

In addition to two-terminal devices, we have also fabricated and measured samples in the Hall bar geometry (Fig. 2.7a), which exhibit broken symmetry states at $\nu = 0, \pm 1$, and ± 2. The $\nu = 0$ state displays a large magnetoresistance in four-terminal measurements, so we conclude that this behavior is due to the graphene and is not caused by contact resistance. The longitudinal conductance σ_{xx} of sample S5 is plotted in Fig. 2.7b as a function of ν. Zeros in σ_{xx} are clearly visible for $\nu = 0$ and $\nu = \pm 4$, and local minima

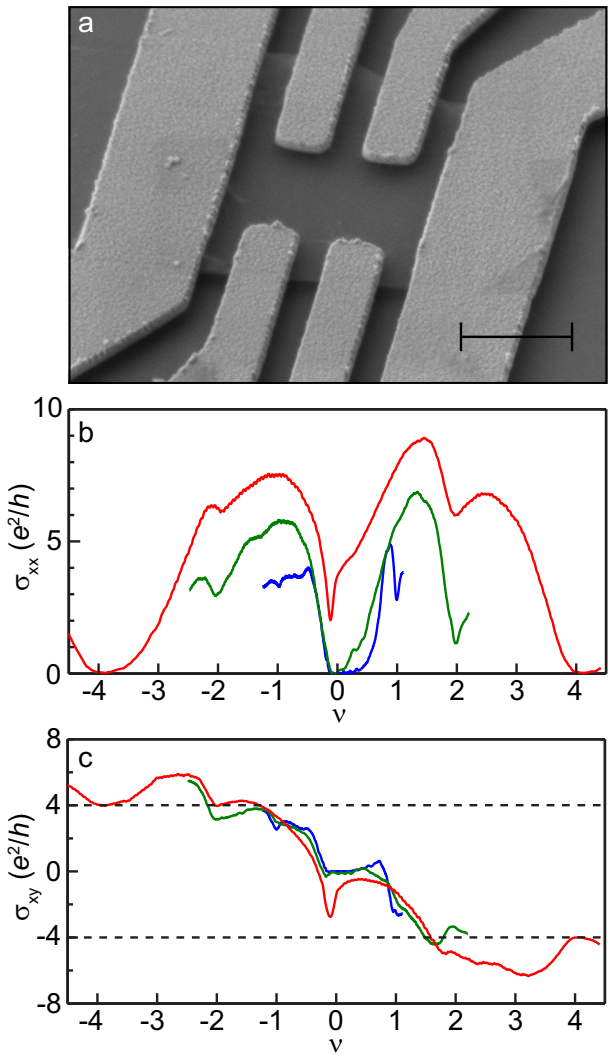

Figure 2.7: Broken symmetry states in a Hall bar device. (a) Scanning electron micrograph of a typical suspended bilayer graphene flake in the Hall bar geometry. Scale bar is 1 μm. (b) Longitudinal conductance σ_{xx} as a function of filling factor ν at magnetic field B of 3 T (red), 6 T (green), and 12 T (blue). Zeros are apparent for $\nu = 0$ and ± 4, and local minima occur at $\nu = \pm 1$ and ± 2. (c) Hall conductance σ_{xy} as a function of ν at the same magnetic fields as in panel (b). The $\nu = 0$ and ± 4 plateaus are fully quantized. Other broken symmetry quantum Hall states at $\nu = \pm 1$ and ± 2 are apparent, but their Hall conductance is not quantized.

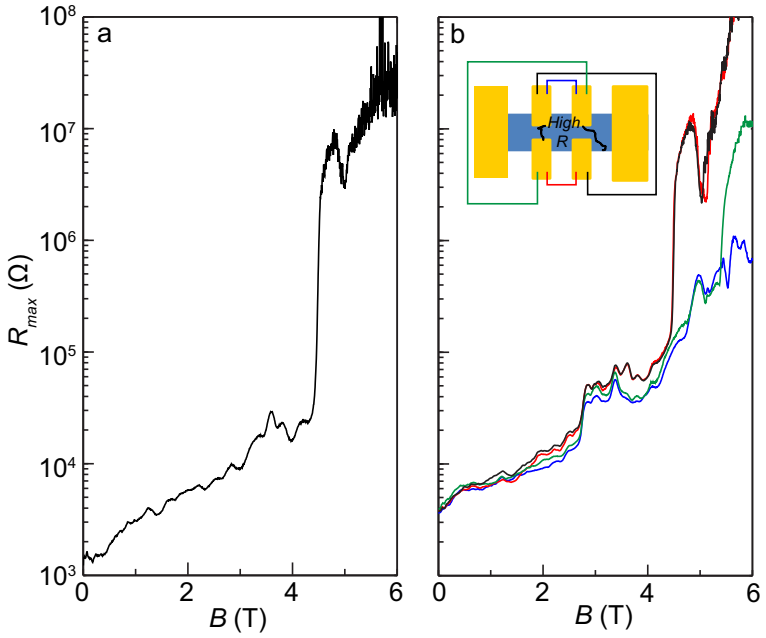

Figure 2.8: Inhomogeneity in Hall bar devices. (a) Four-terminal resistance as a function of magnetic field B for sample S5. A large spike in resistance occurs at $B = 4.5$ T. (b)Two-terminal resistance of the outer two contacts as a function of B for sample S5 when different pairs of inner contacts are shorted together. Differing behavior as a function of shorted contact indicates sample inhomogeneity. Inset: schematic diagram of the Hall bar device, with a highly resistive region labeled that is consistent with the data. Colors in the main panel correspond to shorting of the pins connected by the same color in the inset.

are apparent for $\nu = \pm 1$ and ± 2. Figure 2.7c shows σ_{xy} vs. ν for the same flake. Again, the $\nu = \pm 4$ plateaus are well developed, and a plateau at $\sigma_{xy} = 0$ is also apparent at $\nu = 0$. Quantum Hall plateaus at other intermediate filling factors, however, do not reach their fully quantized values for $B < 6$ T. We therefore conclude that devices in the Hall bar geometry are more disordered than two-terminal devices, likely due to doping from the closely spaced contacts.

The decrease in cleanliness is also evident in the resistance of sample S5 as a function of magnetic field B, which shows a spike at $B \approx 4.5$ T (Fig. 2.8a). By measuring the two-terminal conductivity between the outer electrical contacts of the Hall bar design while shorting different pairs of inner contacts, we are able to determine that this spike is caused

by inhomogeneity between different portions of the flake. Shorting some pairs of inner contacts does not affect the measured resistance, whereas shorting others allows the current to bypass the highly resistive region of the flake so that the resistance at 6 T drops from more than 10^8 Ω to less than 1 MΩ (Fig. 2.8b). This not only shows that the flake in inhomogeneous, but also that the contact resistance of the electrical leads (at least that of the two outer contacts) is small compared to the resistances that we measure, providing further evidence that the highly resistive behavior is a fundamental property of the graphene itself.

Chapter 3

Local Compressibility Measurements of Correlated States in Suspended Bilayer Graphene

Bilayer graphene has attracted considerable interest due to the important role played by many-body effects, particularly at low energies. Here we report local compressibility measurements of a suspended graphene bilayer. We find that the energy gaps at filling factors $\nu = \pm 4$ do not vanish at low fields, but instead merge into an incompressible region near the charge neutrality point at zero electric and magnetic field. These results indicate the existence of a zero-field ordered state and are consistent with the formation of either an anomalous quantum Hall state or a nematic phase with broken rotational symmetry. At higher fields, we measure the intrinsic energy gaps of broken-symmetry states at $\nu = 0, \pm 1$, and ± 2, and find that they scale linearly with magnetic field, yet another manifestation of the strong Coulomb interactions in bilayer graphene.

3.1 Introduction

The low-energy dispersion of bilayer graphene can be described to first order by parabolic valence and conduction bands that meet at the Fermi energy [7]. The charge excitations of this band structure are massive chiral fermions whose quantum Hall signature differs from that of both monolayer graphene [14,15] and conventional two-dimensional electron gases. In the absence of interactions, the Landau level (LL) energy spectrum of bilayer graphene is given by $E_N = \pm\hbar\omega_c\sqrt{N(N-1)}$, where N is the orbital index, $\hbar = h/2\pi$ (h is Planck's constant), $\omega_c = eB/m^*$ is the cyclotron frequency, e is the electronic charge, B is the magnetic field, and m^* is the effective mass [16]. Plateaus occur in Hall conductivity at $\sigma_{xy} = (M+1)e^2/h$, where the factor of four is due to spin and valley degeneracy and M is a non-negative integer.

When magnetic field is large enough or disorder is sufficiently low, interaction effects such as quantum Hall ferromagnetism [17] or magnetic catalysis [60] are predicted to open energy gaps and give rise to additional Hall plateaus at intermediate filling factors. Recent transport measurements have indeed revealed signatures of many-body effects in bilayer graphene [72–75] and the dependence of resistance on temperature and magnetic field was used to determine the magnitude of the corresponding energy gaps [72, 73]. More recently, it has been theoretically predicted that spontaneously broken symmetries will occur in bilayer graphene at zero magnetic field. The nature of the zero-field interacting phase is still under intense theoretical debate, with suggestions of spontaneous transfer of charge between layers [20,21], ferroelectric domains [22], nematic ordering [23,24], or the formation of an anomalous Hall insulator [20, 21, 25–28].

One way to distinguish between the various interacting states is to determine whether an energy gap is present at $B = 0$. Transport measurements can provide an indication of

gap size, but it is known that disorder can decrease the apparent transport gap relative to the true intrinsic gap [11,76]. Therefore, it is desirable to directly probe electronic properties in a thermodynamic measurement. Here, we report the use of a scanning single-electron transistor (SET) [63, 77–79] to measure the local compressibility of a suspended bilayer graphene flake. Investigations into the compressibility of bilayer graphene were recently reported on unsuspended samples [8, 80] with particular attention paid to the gap induced by an electric field, but disorder in these systems was too large to observe the broken-symmetry states discussed above. Our measurement combines the high sensitivity afforded by an SET with the low disorder of suspended devices, allowing us to study electronic states that arise from Coulomb interactions and revealing the existence of an ordered state at zero field. A schematic illustration of the measurement system is shown in Fig. 3.1a; for a full description of the measurement technique, see refs. [77, 78] and Section 3.4. The SET is capable of measuring changes in local electrostatic potential Φ with μV sensitivity. As carrier density n is varied, changes in Φ directly reflect the changes in local chemical potential μ of the bilayer flake, so the scanning SET tip can be used as a local probe of inverse compressibility $d\mu/dn$.

3.2 Energy Gaps and Widths of Quantum Hall States

In order to establish the measurement technique, we first describe the sample behavior in the high-field regime. Figure 3.1b shows a typical measurement of inverse compressibility taken at $B = 2$ T and a temperature of 450 mK. Peaks in $d\mu/dn$, caused by the low density of states between neighboring LLs, are apparent at filling factors $\nu = 0, \pm 2$, and ± 4. The observation of incompressible regions at $\nu = 0$ and ± 2 is indicative of broken symmetries in the zero-energy LL, consistent with recent transport measurements [72–75]. The widths

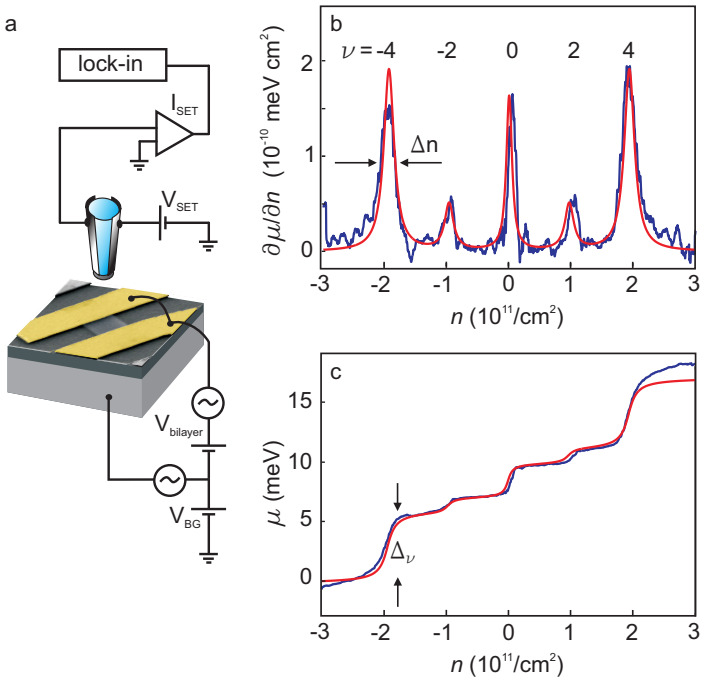

Figure 3.1: (a) Schematic illustration of the measurement setup. (b) Inverse compressibility as a function of carrier density at $B = 2$ T, showing incompressible peaks at $\nu = 0, \pm 2$, and ± 4. (c) Chemical potential as a function of carrier density at $B = 2$ T, obtained by integrating the data in (b). Steps in chemical potential occur at $\nu = 0, \pm 2$, and ± 4 as electrons begin to occupy the next Landau level. In panels (b) and (c), experimental data are shown in blue and fits, based on a Lorentzian at each filling factor, are shown in red.

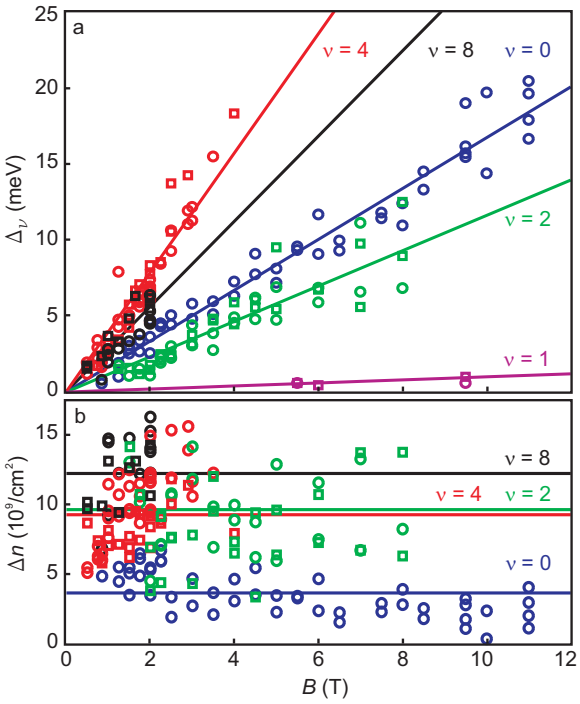

Figure 3.2: (a) Gap size, extracted from a Lorentzian fit, as a function of magnetic field for $\nu = 0$ (blue), ± 1 (magenta), ± 2 (green), ± 4 (red), and ± 8 (black). Squares correspond to electrons, circles to holes. Gap size at all filling factors is well described by linear scaling with magnetic field, with fits given by the solid lines. (b) Incompressible peak width as a function of magnetic field for $\nu = 0$, ± 2, ± 4, and ± 8 [same colors as in (a)]. Peak width does not strongly depend on magnetic field.

of the incompressible regions provide a measure of disorder [79], and the full width at half maximum at $\nu = 4$ is on the order of 10^{10} cm^{-2}. This is more than ten times smaller than in unsuspended devices [62], and is consistent with estimates from transport measurements of similar suspended bilayers [72].

Chemical potential as a function of carrier density, shown in Fig. 3.1c for $B = 2$ T, is obtained either by direct measurement or by integrating curves similar to that shown in Fig. 3.1b. The steps in $\mu(n)$ at each filling factor provide a measure of the energy gaps Δ_ν between neighboring LLs. We have measured gap size at $\nu = 0, \pm 1, \pm 2, \pm 4$, and ± 8 as a function of magnetic field, and the resulting data are shown in Fig. 3.2a. Consistent with the

expected behavior of E_N, Δ_4 and Δ_8 scale linearly with magnetic field, with magnitudes of 3.9 and 2.8 meV/T, respectively. This linear dependence confirms that the range of carrier densities probed in our experiment lies within the energy regime where the bilayer graphene band structure is well approximated by parabolic bands. It should be contrasted with cyclotron resonance and compressibility studies performed at higher densities where the hyperbolic nature of the dispersion was apparent from the sublinear dependence of gap size on magnetic field [8, 81].

It is apparent from Fig. 3.2a that the energy gaps Δ_0 and Δ_2 corresponding to broken-symmetry states at $\nu = 0$ and ± 2 also increase proportionally with B, and have gap sizes of 1.7 and 1.2 meV/T, respectively. For $\nu = 0$, the data show good agreement with the activation energy $E_a = \Delta_0/2 \approx$ 0.3-0.9 meV/T measured in transport experiments [72], as well as recent theoretical predictions [22, 82, 83]. For $\nu = 2$, activation experiments on unsuspended flakes [73] yielded significantly smaller gap sizes and suggested a $B^{1/2}$ dependence for the gap, which seems to conflict with our measurement. However, the error bars from the transport measurement are large enough that a linear fit to the data which passes through the origin is not inconceivable. Linear scaling with B for interaction-driven LLs is reasonable if one considers screening from higher orbital LLs, whose energy separation is much smaller than the Coulomb energy for all experimentally relevant fields [22]. The linear scaling of Δ_0 and Δ_2 can therefore be understood to result from the very strong Coulomb interactions in bilayer graphene. Finally, the sample exhibits energy gaps of less than 1 meV at $\nu = \pm 1$ in high magnetic fields. Linear scaling with a slope of approximately 0.1 meV/T provides a reasonable fit to these data, but the gap sizes are too small to conclusively rule out $B^{1/2}$ dependence.

We can use the measured gap sizes to determine the effective mass of bilayer graphene. Using the measured energy gaps for $|\nu| = 4$ and 8 at each magnetic field and comparing

with the expression for E_N, we obtain an estimate that $m^* = (0.042 \pm .002)m_e$, in good agreement with Shubnikov de Haas measurements [10]. It is also important to note that for samples with a single gate, density and electric field cannot be controlled independently, so all gaps at nonzero filling factors are measured in an electric field. Changes in the effective mass could result from deviations from the parabolic band structure or from an electric field applied perpendicular to the flake [9, 10].

Figure 3.2b shows the widths of the incompressible regions at each filling factor as a function of magnetic field. The peak at $\nu = 0$ is significantly narrower than the others (see also Fig. 3.1b), which may indicate that higher filling factors are subject to additional sources of disorder that do not affect the $\nu = 0$ state. One possible explanation for this finding is the existence of variations in the effective magnetic field, which can be caused by ripples or strain [84–86].

3.3 Correlated State at Zero Field

We now discuss the behavior of the sample at small magnetic fields. Figures 3.3a,b show inverse compressibility as a function of density and magnetic field. We observe distinct incompressible peaks corresponding to quantum Hall states at $\nu = \pm 4$ that extend all the way down to $B = 0$, where they merge into an incompressible region at the charge neutrality point (Figs. 3.3a-c). Surprisingly, the $\nu = \pm 4$ gaps do not vanish at low fields; in fact, they increase with decreasing field below 0.2 T, as shown in Fig. 3.3d. The zero-field incompressible peak has a width of approximately 10^{10} cm^{-2}, and integration yields a step in chemical potential of nearly 2 meV. This increase in chemical potential is too large to be explained by a disorder-induced electric field, which would only lead [10] to gaps on the order of 0.1 meV for charge inomogeneity of 10^{10} cm^{-2}. We observe qualitatively similar

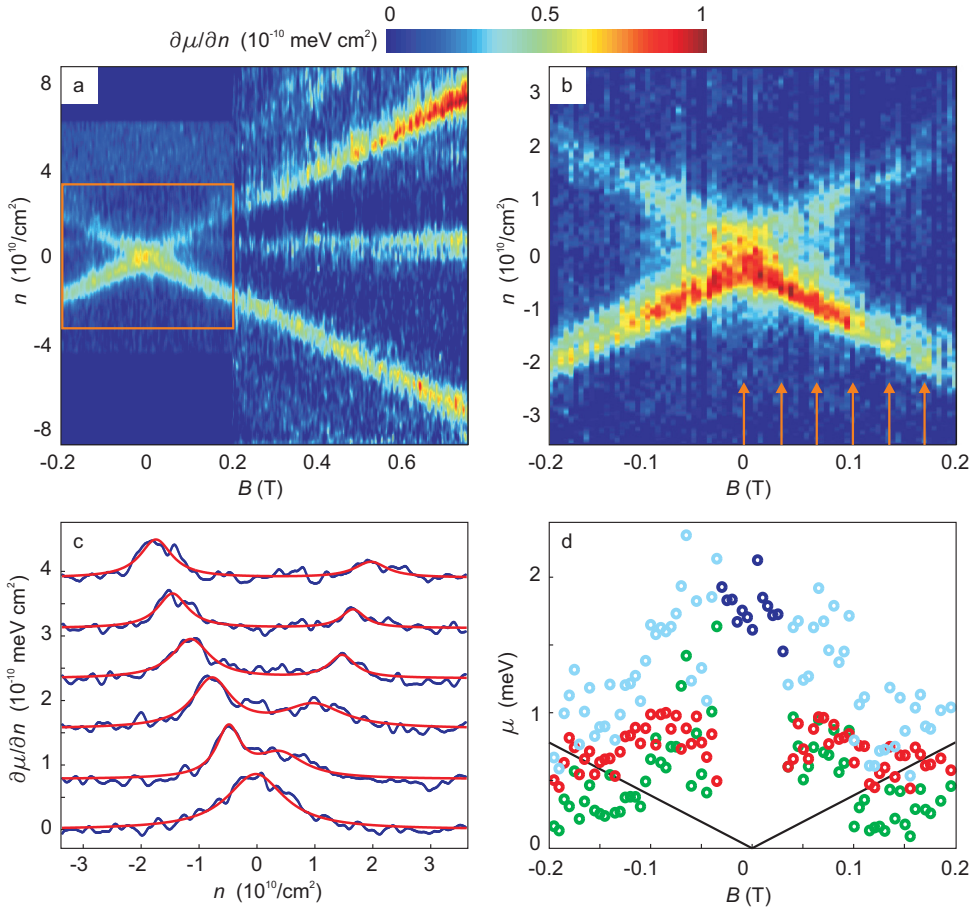

Figure 3.3: (a) Inverse compressibility as a function of carrier density and magnetic field. Incompressible peaks occur at $\nu = 0$ and ± 4. Below about 0.2 T, peak height along $\nu = \pm 4$ increases with decreasing field, culminating in an incompressible peak at zero field. (b) Zoom-in on the low-field behavior of the sample, taken at a different location on the flake from that in (a). (c) Line cuts of inverse compressibility along the red arrows shown in panel (b) for magnetic fields between $B = 0$ and 0.175 T in steps of 0.035 T. Curves are offset for clarity. Data are shown in blue, and the red curves are two-Lorentzian fits, except for the zero-field fit, which is composed of only one Lorentzian. (d) Gap size at $|\nu| = 4$ for electrons (green), holes (red), and their sum (cyan). Data for $|B| > 0.03$ T is based on a two-Lorentzian fit. The blue circles at low field describe the jump in chemical potential across the charge neutrality point, as modeled by a single Lorentzian fit. Solid black lines correspond to $\Delta_4 = 3.9(B[\mathrm{T}])$ meV.

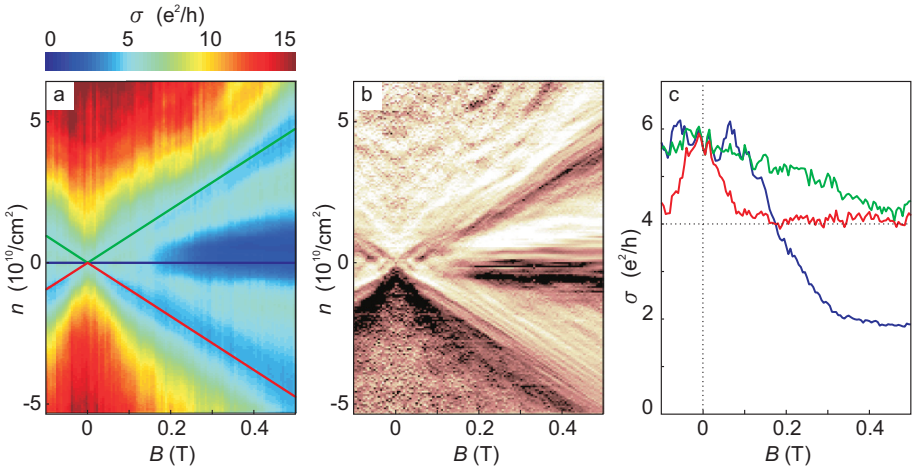

Figure 3.4: (a) Two-terminal conductance as a function of carrier density and magnetic field. Quantum Hall plateaus at $\nu = \pm 4$ emerge at very low field, and the onset of the highly resistive state at $\nu = 0$ is also apparent. (b) Derivative of conductance with respect to carrier density. Local peaks and minima with the same slope as $\nu = \pm 4$ are visible, indicative of localized states. (c) Conductivity along filling factors $\nu = -4$ (red), 0 (blue), and 4 (green) as a function of magnetic field.

behavior at all positions along the flake (see Section 3.5). It is worthwhile to note that the measurements give no indication of negative compressibility [87] at zero field, but are consistent with more recent predictions [88].

To further elucidate the origin of the low-field incompressible behavior, we have performed transport measurements on the same flake. Two-terminal resistance as a function of carrier density and magnetic field is shown in Fig. 3.4a. Despite the relatively large jump in chemical potential that we observe in compressibility measurements, the resistance near the charge neutrality point at $B = 0$ is only a few kΩ. For comparison, we note that the gap size of the $\nu = 0$ state at $B = 0.5$ T is less than 1 meV, but even for this small gap, a marked decrease in conductance is already apparent (Fig. 3.4c). Therefore, the formation of an energy gap with conduction mediated by activation is an insufficient explanation for the zero-field behavior that we observe. The derivative of conductance with respect to carrier density is plotted in Fig. 3.4b. Several sharp lines with the same slope as the $\nu = 4$

state are apparent, and these conductance fluctuations are caused by localized states in the bilayer [89]. The localized states, which indicate the presence of an energy gap, persist all the way to zero field.

The incompressible behavior and transport characteristics at $B = 0$ indicate the presence of an interacting state, in agreement with recent studies of dual-gated bilayers [90]. In the limit of parabolic bands, the non-vanishing density of states at the charge neutrality point means that even infinitesimally small electron-electron interactions can lead to correlated states [20–28]. The existence of a zero-field incompressible peak and the fact that gap size along $\nu = \pm 4$ does not vanish at low fields are consistent with two proposed interacting states, which we discuss below.

One proposal that is consistent with our measurements is the formation of an anomalous Hall insulator at low electric and magnetic field [20,21,25–28]. In such a state, time-reversal symmetry is spontaneously broken and domains form where the flake is at either $\nu = 4$ or $\nu = -4$. It is reasonable that we observe incompressible behavior at both filling factors if we assume that the SET is too large to resolve individual domains. In this scenario, the $B = 0$ conductance is dominated by edge state transport and should therefore remain at a few kΩ per square, consistent with our findings. The fact that gap size along $\nu = \pm 4$ increases with decreasing field below about 0.2 T can be understood to arise from the competition between the anomalous Hall phase and the standard quantum Hall gap [27,28].

So far, we have assumed parabolic bands and neglected trigonal warping. Trigonal warping modifies the band structure of bilayer graphene so that four Dirac cones emerge at low energies, leading to a 16−fold degenerate LL at zero energy for low magnetic fields. Effects of trigonal warping should be apparent [7] at densities as high as 10^{11} cm^{-2}, which is well within the experimentally accessible regime due to the low disorder in the sample. The results, however, cannot be explained by trigonal warping in the single-particle picture

because the incompressible peaks at low magnetic field in Fig. 3.4a follow $\nu = \pm 4$ rather than $\nu = \pm 8$. Recently, however, it was theoretically predicted [23,24] that electron-electron interactions can break rotational symmetry and modify the dispersion into a nematic phase that is characterized by two Dirac cones. In this scenario, one would expect incompressible peaks along $\nu = \pm 4$, with energy gaps that scale as $\Delta_\nu \sim B^{1/2}$. This means that gap size would remain relatively large at low fields, as we observe. In this picture, the zero-field incompressible peak that we measure can be ascribed to the vanishing density of states, and because of the gapless nature of the spectrum, the conductance should remain relatively high, also consistent with our observations.

Acknowledgments

We would like to acknowledge useful discussions with L. S. Levitov, R. Nandkishore, S. Sachdev, M. S. Rudner, A. H. MacDonald, and B. I. Halperin. This work was supported by the U.S. Department of Energy (DOE), Office of Basic Energy Sciences, Division of Materials Sciences and Engineering under Grant No. DE-SC0001819, by the DOE SCGF administered by the Oak Ridge Institute for Science and Education (ORISE), by the 2009 U.S. Office of Naval Research Multi University Research Initiative (MURI) on Graphene Advanced Terahertz Engineering (GATE) at MIT, Harvard and Boston University, by Harvards NSEC under National Science Foundation Grant No. PHY-0646094, and by the Alexander von Humbolt Foundation. This work was performed in part at the Center for Nanoscale Systems (CNS), a member of the National Nanotechnology Infrastructure Network (NNIN), which is supported by the National Science Foundation under NSF Grant No. ECS-0335765. CNS is part of the Faculty of Arts and Sciences at Harvard University.

3.4 Methods

Sample fabrication is described in Appendix A. The sample was measured in an ultra-high vacuum scanning probe system with a ^{3}He refrigerator. All measurements were performed at 450 mK. Back gate voltage was limited to ± 15 V to avoid collapse of the device.

Scanning probe tips were fabricated according to the procedure outlined in Appendix B. The SET leads and island were all 19 nm thick. For the measurements described in this chapter, tip size was approximately 150-200 nm and the tip was held between 50 and 200 nm above the flake. Compressibility measurements were performed using the ac and dc techniques described in subsection 1.4.2, with the carrier density modulated by about 1.5×10^9 cm^{-2}.

Due to the finite sample size, the SET is also affected in both schemes by fringing fields from the back gate [63, 79], which give rise to a constant offset in $d\mu/dn$. We account for this parasitic capacitance by subtracting a constant value so that $d\mu/dn = 0$ within each LL. This is necessarily an overestimate, because it corresponds to a delta-function representation of the LL, whereas real LLs are broadened by disorder. Therefore, the gap sizes should be taken as lower limits. Incompressible peaks at each filling factor are fit with a single Lorentzian, with amplitude and width as fitting parameters. The uncertainty in effective mass is calculated by adding in quadrature the uncertainty at each filling factor, as obtained by a linear regression.

3.5 Supplementary Discussion

3.5.1 Zero-field compressibility at large densities

Figure 3.5 shows the inverse compressibility of the sample at zero magnetic field, taken over a larger density range and at a slightly different position along the flake. Similar to the

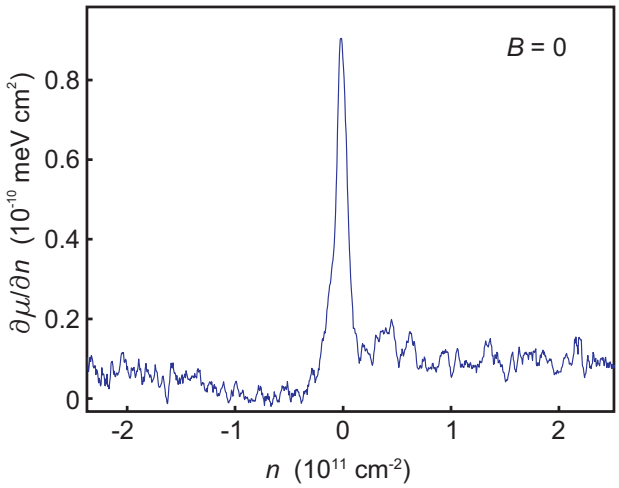

Figure 3.5: Inverse compressibility as a function of carrier density at zero magnetic field. A sharp peak near the charge neutrality point is apparent, consistent with the measurements presented in the main portion of the paper. There is little variation in compressibility outside the central peak.

measurements presented in the main portion of the paper, a sharp incompressible peak is apparent at the charge neutrality point. As electron density is increased beyond this central peak, little change in compressibility occurs over the entire measurement range. For holes, inverse compressibility increases slightly as density is increased. The origin of this behavior is unclear, and the change is an order of magnitude smaller than the negative compressibility predicted by Kusminskiy *et al.* [87]. It also appears that the compressibility is somewhat larger for holes than for electrons. Such behavior is consistent with the inclusion of the γ_4 hopping parameter, which increases the density of states for holes and decreases it for electrons [8]. However, a non-negligible γ_4 would also be expected to cause an asymmetry between the energies of electron and hole Landau levels, which we do not observe.

3.5.2 Spatial scans at low magnetic field

It is apparent in Fig. 3.3 that the incompressible peak height and the gap sizes are larger for holes than for electrons along $|\nu| = 4$ at low magnetic fields. Figures 3.6a,b

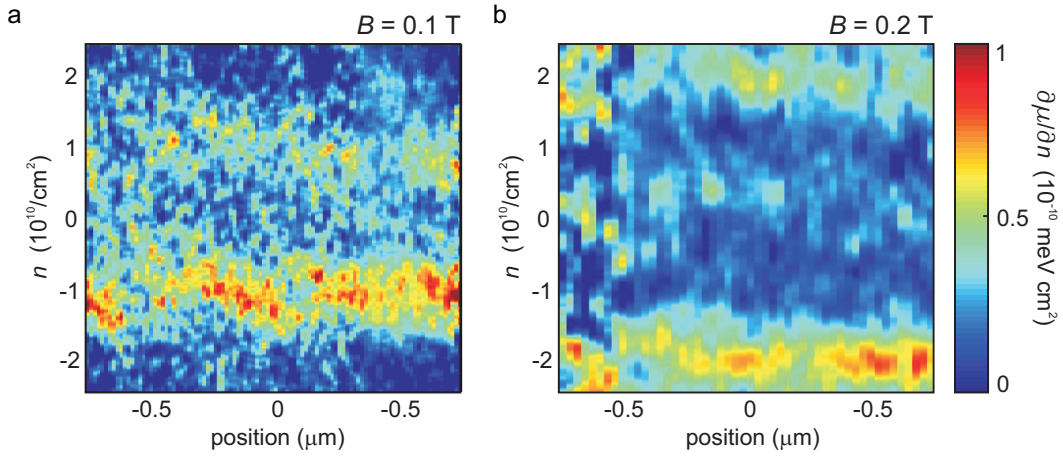

Figure 3.6: (a) Inverse compressibility as a function of carrier density and position along the flake at 0.1 T. The incompressible peaks at $\nu = \pm 4$ (centered at approximately $\pm 10^{10}$ cm^{-2}) are consistently apparent, independent of position. The incompressible peak on the hole side is consistently stronger than that on the electron side. Some variations in the density at which the peaks occur is visible, providing an estimate of disorder. (b) Inverse compressibility as a function of carrier density and position along the flake at 0.2 T. The incompressible peaks at $\nu = \pm 4$ (centered at approximately $\pm 2 \times 10^{10}$ cm^{-2}) are again apparent along the entire flake. The electron-hole asymmetry is also apparent at this field, and the $\nu = 0$ peak is just beginning to emerge.

show compressibility measurements taken as a function of density and position along the flake at $B = 0.1$ and 0.2 T, respectively. These measurements show that the electron-hole asymmetry is consistent across the entire width of the sample. It is also worthwhile to note that the fluctuations in density at which the incompressible peaks occur can provide another measure of the disorder in the sample. Consistent with estimates made by other means, it appears that the charge inhomogeneity is less than 10^{10} cm^{-2}.

3.5.3 Additional measures of $\nu = \pm 4$ gap magnitude

Figures 3.7a,b show 'slanted' scans of inverse compressibility which follow a fixed carrier density range surrounding filling factors $\nu = -4$ and 4, respectively, at magnetic field between 0 and 1 T. At low fields, the second $|\nu| = 4$ peak and the $\nu = 0$ peak are visible

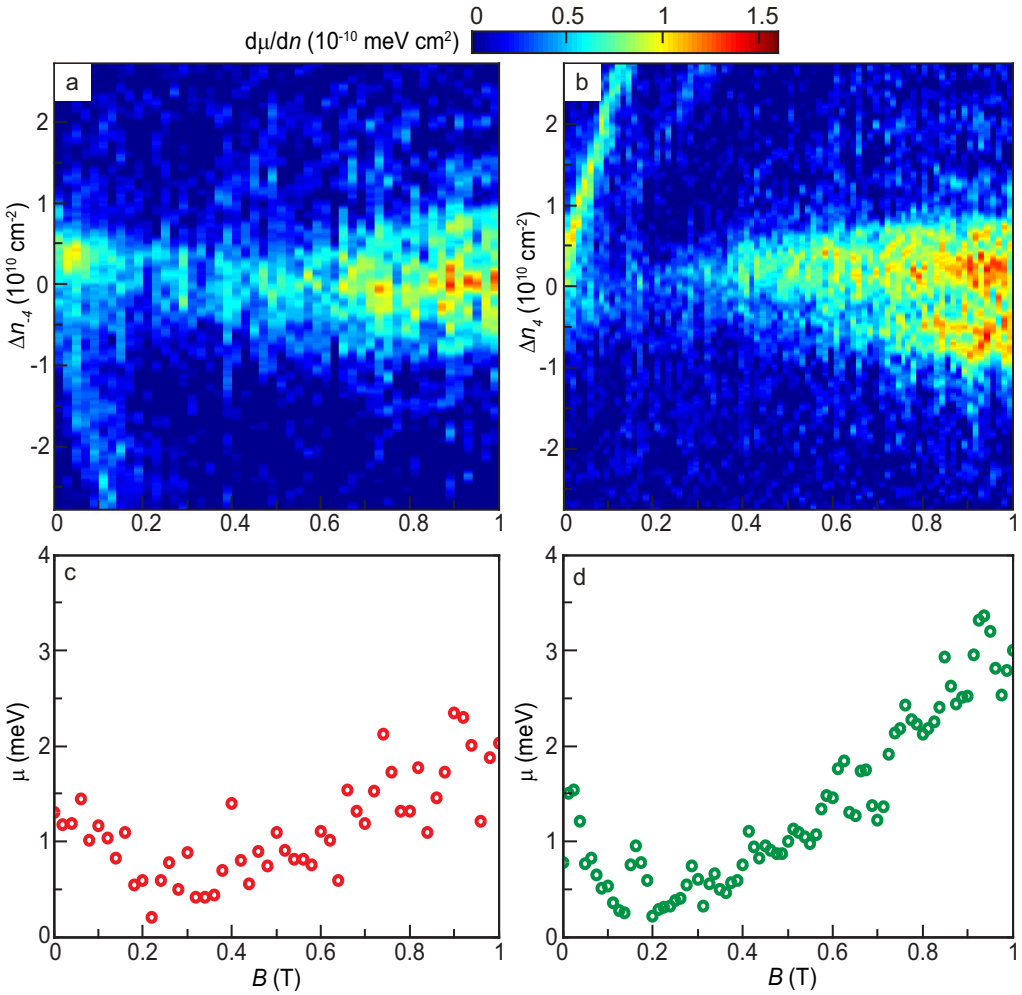

Figure 3.7: Inverse compressibility taken over a constant density range centered around $\nu = -4$ (a) and $\nu = 4$ (b) as a function magnetic field. Data was taken at a slightly different position and height compared to that presented in the main paper. In each case, at low fields, the other $|\nu| = 4$ peak is visible as well. Gap size along $\nu = -4$ (c) and $\nu = 4$ (d) as a function of magnetic field, as fit by a single Lorentzian. For $B < 0.1$ T, the gap size may be an overestimate due the effect of the other $|\nu| = 4$ incompressible peak.

as well. These measurements were performed at slightly different positions and heights compared to those presented in the paper. Figures 3.7c,d show the extracted gap size at each respective filling factor as a function of magnetic field. We again observe that the gap size along $\nu = \pm 4$ does not vanish at low field, but increases with decreasing field below 0.2 T. For $B > 0.2$ T, gap size increases linearly with field, as expected. The qualitative agreement between this dataset and that presented in the main paper provides a second indication that our findings are not strongly dependent on position.

3.6 Epilogue

The nature and tunability of the broken-symmetry quantum Hall states and the zero-field behavior discussed above have continued to attract significant theoretical and experimental attention from many groups over the past several years. Concurrently with the measurements described in this chapter, a suspended bilayer graphene sample with a suspended top gate was fabricated to enable independent control of carrier density and electric field [90]. Transport measurements on these dual-gated devices showed evidence for a phase transition between two different types of insulating $\nu = 0$ states, one stabilized at high magnetic field, and the second favored by a large electric field. The strengths of other broken-symmetry quantum Hall states also varied with electric field, and subsequent measurements by other experimental groups showed similar behavior [91, 92].

Initially, Weitz *et al.* [90] identified the $\nu = 0$ state at high electric field as layer-polarized and the state at high magnetic field as spin-polarized. However, subsequent theoretical calculations mapped out the phase diagram of possible order parameters, and suggested that the experimental observations were best fit by a canted antiferromagnet at low electric field rather than a spin-polarized state [44]. Recent experiments on dual-gated

bilayer graphene indeed provide evidence for a canted antiferromagnet at large perpendicular magnetic field that undergoes a second order phase transition to a spin-polarized state with counter-propagating spin-polarized edge modes in a large parallel magnetic field [48].

In addition to the high-field broken-symmetry $\nu = 0$ states, transport measurements showed evidence of a third distinct weakly resistive phase at the charge neutrality point in zero electric and magnetic field [90], similar to the low-field behavior described in this chapter. Since these first observations, many other groups have also found evidence of a state at zero magnetic field in bilayer graphene. However, the experimental signature has varied from weakly resistive [90, 93, 94] to fully insulating [92], and some samples do not show a phase transition as magnetic field is increased. Moreover, based on these different observations, the zero-field state has been identified as a nematic state [93] or a layer antiferromagnet [92], with other groups [90, 94] allowing for multiple possible candidate states. Beyond the theoretical explanations discussed above, mechanical strain has been suggested as a possible cause of the observed behavior [95], and others have sought to explain the experimental differences in terms of different screening in different samples [29]. To date, the detailed nature of the zero-field state at the charge neutrality point in bilayer graphene has not been resolved, and remains an active and exciting area of research.

Chapter 4

Unconventional Sequence of Fractional Quantum Hall States in Suspended Graphene

Graphene provides a rich platform to study many-body effects, owing to its massless chiral charge carriers and the fourfold degeneracy arising from their spin and valley degrees of freedom. We use a scanning single-electron transistor to measure the local electronic compressibility of suspended graphene, and we observe an unusual pattern of incompressible fractional quantum Hall states that follows the standard composite fermion sequence between filling factors $\nu = 0$ and 1 but involves only even-numerator fractions between $\nu = 1$ and 2. We further investigate this surprising hierarchy by extracting the corresponding energy gaps as a function of the magnetic field. The sequence and relative strengths of the fractional quantum Hall states provide insight into the interplay between electronic correlations and the inherent symmetries of graphene.

4.1 Introduction

Application of a strong perpendicular magnetic field B to a two-dimensional electron gas (2DEG) gives rise to flat energy bands called Landau levels (LLs), which normally contain a total of eB/h states, where e is the electron charge and h is Planck's constant. In graphene, each of these states has an additional fourfold degeneracy resulting from the spin and valley degrees of freedom, and the LLs possess an approximate SU(4) symmetry [30]. Incompressible quantum Hall states are formed when the Fermi energy lies between LLs. In graphene, LLs are filled at filling factors $\nu = nh/eB = \pm 4(N + 1/2)$ in the absence of electron-electron interactions [14, 15, 79], where n is the charge-carrier density and N is the orbital index. In this expression, the quantum Hall sequence is shifted by a half-integer, a distinctive signature that reflects the sublattice pseudospin of graphene.

When disorder is low and at high magnetic fields, Coulomb forces between electrons become important, and many-body effects emerge. One example is the fractional quantum Hall effect (FQHE), in which correlations between electrons generate excitations with fractional charge at certain rational filling fractions [2, 49, 50, 52]. Recently, the FQHE of Dirac fermions has attracted considerable attention [33, 96–108]. In graphene, the low dielectric constant and unusual band structure lead to FQH states with energy gaps that are larger than in GaAs at the same field, particularly in the $N = 1$ LL [97, 101, 102]. Moreover, the SU(4) symmetry of charge carriers in graphene could yield FQH states without analogs in GaAs [98, 99, 105]. The FQHE was recently observed [58, 109, 110] in suspended graphene samples at $\nu = 1/3$ and $2/3$, and transconductance fluctuations also showed evidence of a state at $\nu = 2/5$ [111]. Measurements of graphene on hexagonal boron nitride substrates [53] revealed further FQH states at all multiples of $\nu = 1/3$ up to $13/3$, except at $\nu = 5/3$. The absence of a FQH state at $\nu = 5/3$ might result from low-lying excitations associated with

SU(2) or SU(4) symmetry, but alternate scenarios associated with disorder could not be ruled out in earlier studies [53].

Here, we report local electronic compressibility measurements of a suspended graphene flake performed with a scanning single-electron transistor (SET) (Fig. 4.1a) [77, 78]. By modulating the carrier density and monitoring the resulting change in SET current, we measure both the local chemical potential μ and the local inverse electronic compressibility of the graphene flake (inverse compressibility $\kappa^{-1} = n^2 d\mu/dn$, but hereafter we drop the prefactor and use the term to mean $d\mu/dn$). Therefore, our local technique provides a direct thermodynamic measurement of bulk sample properties and is sensitive to weak effects that may be obscured by disorder in global transport studies.

4.2 Fractional Quantum Hall (FQH) States

The inverse compressibility as a function of carrier density and magnetic field is shown in Fig. 4.1b. At zero magnetic field, we observe an incompressible peak that arises from the vanishing density of states at the charge neutrality point in graphene. For $B > 0$, strong incompressible behavior occurs at $\nu = \pm 4(N + 1/2)$, confirming the monolayer nature of our sample. In addition to the expected single-particle quantum Hall features, we observe incompressible states at intermediate integer filling factors ν = 0, 1, 3, 4, 5, 7, 8, and 9. These integer broken-symmetry states arise from interactions among electrons [39, 53, 110, 112] and are visible at fields well below 1 T, indicating the high quality of our sample. Most intriguing, however, is the appearance of incompressible peaks at fractional filling factors, the strongest of which emerge around $B = 1$ T. It is straightforward to distinguish FQH states from oscillations in compressibility caused by localized states. Localized states occur at a constant density offset from their parent quantum Hall state and are therefore parallel

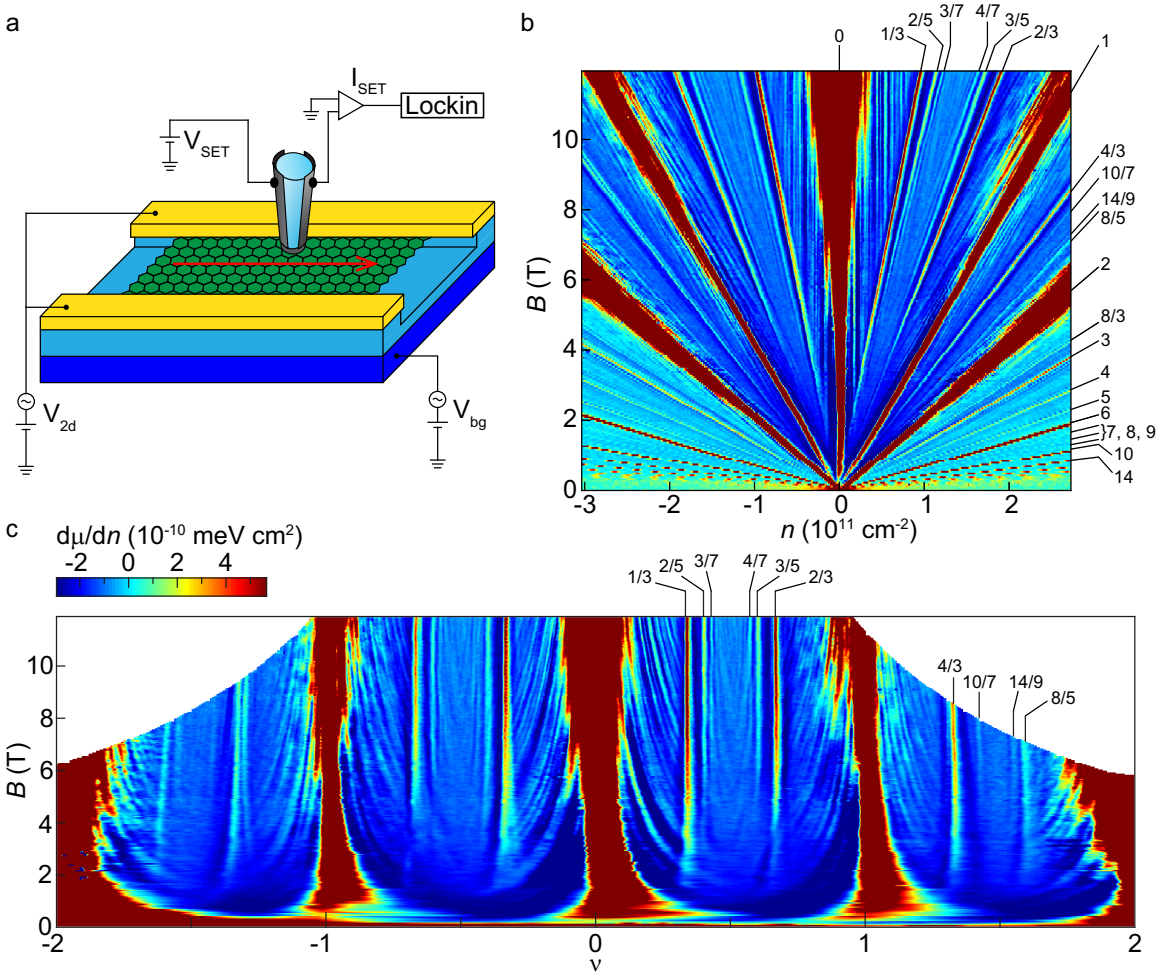

Figure 4.1: Measurement setup and Landau fan. (a) The SET is about 100 nm in size and is held 50 to 150 nm above the graphene flake. The red arrow indicates the path of the spatial scans in Fig. 4.4. V, voltage; I, current. (b) Inverse compressibility $d\mu/dn$ as a function of carrier density n and magnetic field B. (c) Data from (b) plotted as a function of filling factor ν. Vertical features correspond to quantum Hall states, whereas localized states curve as the magnetic field is changed. Principal integer and FQH states are labeled in (b) and (c). These panels share the same color scale.

to lines of constant filling factor in the n-B plane [79]. When inverse compressibility is plotted as a function of filling factor (Fig. 4.1c), localized states curve as the magnetic field is changed, whereas any incompressible behavior caused by an integer or FQH state appears as a vertical feature (see Section 4.7).

4.3 Unconventional Sequence of FQH States

Figure 4.2a shows a finer measurement of the inverse compressibility as a function of filling factor and magnetic field for $\nu < 1$. Incompressible peaks occur at $\nu = 1/3$, 2/3, 2/5, 3/5, 3/7, 4/7, and 4/9, reproducing the standard composite fermion sequence observed in GaAs. We resolve the strongest incompressible states, $\nu = 1/3$ and 2/3, down to $B \approx 1$ T, although $\nu = 2/3$ weakens considerably below 4 T. As the filling factor denominator increases, the field at which the corresponding state emerges also increases, with $\nu = 4/9$ only apparent above $B \approx 9$ T.

Between $\nu = 1$ and 2, we observe a different pattern of incompressible behavior (Fig. 4.2b). Surprisingly, no FQH states with odd numerators occur in this regime. Instead, the system condenses into incompressible states only at $\nu = 4/3$, 8/5, 10/7, and 14/9. The incompressible peaks at $\nu = 4/3$ and 8/5 are the most robust, persisting down to about 1 and 1.5 T, respectively. In graphene, $\nu = 2$ corresponds to a filled LL ($N = 0$), so it is natural to label FQH states with the filling fraction $\nu^* = 2 - \nu$. Doing so reveals a clear pattern of incompressible peaks at $\nu^* = 2p/(4p \pm 1)$ for integer $p \leq 2$, which is similar to the composite fermion sequence, except that only filling fractions with even numerators lead to incompressible states.

The absence of odd-numerator fractions indicates that a robust underlying symmetry enables low-lying excitations, preventing the formation of incompressible states. One

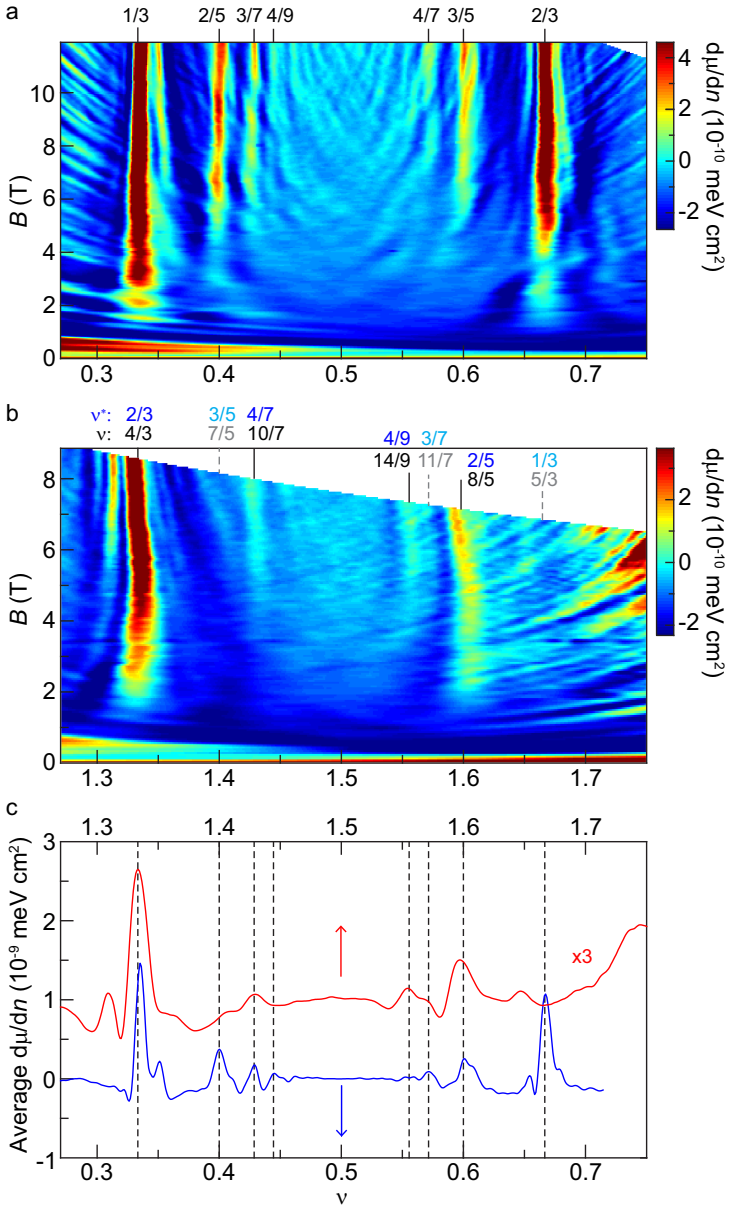

Figure 4.2: (a) Finer measurement of $d\mu/dn$ as a function of filling factor and magnetic field. Incompressible states follow the standard composite fermion sequence between $\nu = 0$ and 1. (b) Finer measurement of $d\mu/dn$ between $\nu = 1$ and 2. Incompressible states occur only at filling fractions with even numerators. (c) $d\mu/dn$ between $\nu = 0$ and 1 (blue), and between $\nu = 1$ and 2 (red). Curves are offset for clarity. Averaging over magnetic field reduces the influence of localized states and shows clear incompressible peaks centered at $\nu = 1/3$, 2/3, 4/3, 2/5, 3/5, 8/5, 3/7, 4/7, 10/7, 4/9, and 14/9.

possible explanation is that the Zeeman effect lifts spin degeneracy, but valley symmetry remains intact, allowing large valley skyrmions to form with a minimal energy penalty at odd-numerator filling factors. The behavior we observe between $\nu = 1$ and 2 is reminiscent of results from strained Si and AlAs 2DEGs, which also have a valley degree of freedom and exhibit weakened odd-numerator states [113–116]. However, the analogy is not perfect. The large effective mass and g factor in these semiconducting materials lead to fully spin-polarized LLs due to single-particle effects; in contrast, the Zeeman energy is substantially smaller than the LL separation in graphene. In valley-symmetric AlAs, the energy gap at $\nu = 1/3$ is large compared with that at $\nu = 5/3$ [115], opposite from the behavior we observe at $\nu^* = 1/3$ and 5/3 when we account for the half-integer shift of LLs in graphene. This suggests that the total electron density, and not just the filling fraction, may play an important role in electronic interactions in the lowest LL, a topic that has only recently been explored [117]. Moreover, whereas the incompressible behavior we observe between $\nu = 1$ and 2 is consistent with SU(2) symmetry, it is evident that this symmetry does not persist between $\nu = 0$ and 1, where the full composite fermion sequence is present. The differing behavior above and below $\nu = 1$ suggests an intriguing interplay between the inherent symmetries of graphene and electronic correlations in the lowest LL. This is different from strained Si, in which odd-numerator states are weakened both above and below $\nu = 1$ [113]. In the valley-symmetric AlAs data from [115], both $\nu = 7/5$ and 3/5 states are absent, whereas $\nu = 8/5$ and 2/5 are visible. At higher magnetic fields, however, the $\nu = 3/5$ state is apparent [117], similar to the behavior in graphene.

Averaging over a range of magnetic fields helps to reduce fluctuations from localized states because they do not occur at constant filling factor as the magnetic field is varied. Figure 4.2c shows the inverse compressibility between $\nu = 0$ and 1, averaged over 9 to 11.9 T (blue), and between $\nu = 1$ and 2, averaged over 4.9 to 6.4 T (red). These curves reveal clear

incompressible peaks centered at the filling fractions discussed above, as well as negative contributions to the inverse compressibility immediately surrounding each FQH state, which can be ascribed to interactions among the quasiparticles and quasiholes involved in the FQHE [57]. A slight incompressible peak occurring at $\nu = 1.65$ (Fig. 4.2c) may indicate the emergence of a FQH state at $\nu = 5/3$; however, it is much weaker than all other multiples of $\nu = 1/3$ and is therefore consistent with the conclusion that all odd-numerator FQH states are suppressed for $\nu > 1$.

4.4 Steps in Chemical Potential and Widths of FQH States

Integrating the inverse compressibility with respect to carrier density allows us to extract the step in chemical potential $\Delta\mu_\nu$ associated with each FQH state and thereby determine the corresponding energy gap Δ_ν. Figure 4.3a displays the chemical potential as a function of carrier density at $B = 11.9$ T. We define $\Delta\mu_\nu$ as the difference between the local maximum and minimum in the chemical potential, and the values for each FQH state as a function of magnetic field are plotted in Figs. 4.3b,c. We define the zero of $d\mu/dn$ based on its value at $\nu = 1/2$ to accurately determine $\Delta\mu_\nu$ at each field (see Section 4.7). Because the chemical potential is defined with respect to electrons, the step in chemical potential must be multiplied by the ratio of the quasiparticle charge to the electron charge to obtain the energy gap of fractionally charged quasiparticles.

The steps in chemical potential at each multiple of $\nu = 1/3$ have comparable magnitudes (Fig. 4.3b), and they scale approximately linearly with the field. The linear dependence of the FQH energy gaps on the magnetic field is surprising because states driven by electronic interactions are expected to scale as $B^{1/2}$; the origin of this behavior is unclear. The steps in chemical potential at $\nu = 2/5$, $3/5$, and $8/5$ are smaller and also depend

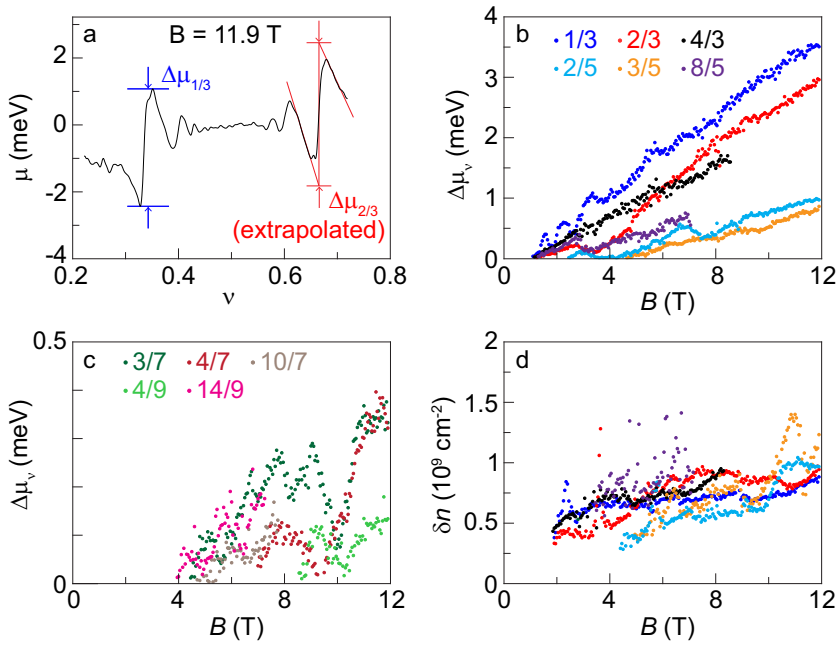

Figure 4.3: (a) Chemical potential relative to its value at $\nu = 1/2$ as a function of carrier density at 11.9 T. The step in chemical potential of each incompressible state is given by the difference in chemical potential between the local maximum and minimum (blue). Data presented in (b) and (c) were extracted using this method. (b) Steps in chemical potential associated with FQH states at measured multiples of $\nu = 1/3$ and 1/5 as a function of magnetic field. (c) Steps in chemical potential of FQH states at measured multiples of $\nu = 1/7$ and 1/9 as a function of magnetic field. (d) Incompressible peak width of the FQH states as a function of magnetic field. Colors are same as in (b).

approximately linearly on the magnetic field, although we cannot rule out a $B^{1/2}$ scaling. The steps in chemical potential at $\nu = 3/7$, 4/7, 10/7, 4/9, and 14/9 are even smaller (Fig. 4.3c), and their extracted magnitudes fluctuate substantially as a function of the magnetic field, presumably because of localized states at the measurement point.

The energy gaps obtained from compressibility, which yield the cost of adding charged quasiparticle excitations to the system, have a slightly different physical meaning from those obtained in activation measurements, which probe the energy separation between the ground state and lowest excited state at a given filling factor. Nonetheless, the energy gaps that we extract (Fig. 4.3) are comparable to results from activation studies [53, 109], which yielded

$\Delta_{1/3} \approx 1.4$ to 1.8 meV at 12 T and $\Delta_{4/3} \approx 1.4$ meV at 35 T. A comparison to $\Delta_{4/3}$ at 35 T is difficult because of the discrepancy in field strength; however, extrapolating the linear slope we measure in $\Delta_{4/3}$ yields a value of ∼2.8 meV at 35 T. At the highest available magnetic fields, our measured energy gaps are only slightly smaller than theoretical predictions at $\nu = 1/3$ but are 3 to 10 times smaller than those theoretically predicted at $\nu = 2/3$, 4/3, 2/5, and 8/5 (see Section 4.7) [96,97,99,101,102,107]. This discrepancy probably results in part from sample disorder, which smears out the cusps in $\mu(n)$ and therefore decreases the apparent step in chemical potential. The effects of disorder can be partially mitigated by linear extrapolation of the negative slope in $\mu(n)$ surrounding each fractional quantum Hall state (see Section 4.7) [118]. The widths δn of the most robust FQH states (Fig. 4.3d) were determined by fitting a Gaussian to the incompressible peak at each filling factor. They are only weakly dependent on magnetic field, suggesting that δn reflects the amount of local disorder in our device [79]. The exceptionally small peak widths provide another indication that the sample is especially clean.

Together, the unconventional sequence and relative strengths of the FQH states provide insight into the interplay between electronic interactions and symmetry in graphene. Between $\nu = 0$ and 1, the compressibility is approximately symmetric about $\nu = 1/2$, suggesting that the fourfold spin and valley degeneracy is fully lifted. In contrast, the missing odd-numerator states indicate that one symmetry persists between $\nu = 1$ and 2. Nonetheless, the behavior in each regime exhibits some surprising similarities. Notably, the incompressible states that we observe above and below $\nu = 1$ have comparable energy gaps. Further study is necessary to elucidate the exact spin and valley ordering of each state; for example, tilted field measurements decouple Zeeman splitting from orbital effects and could provide insight into spin polarization.

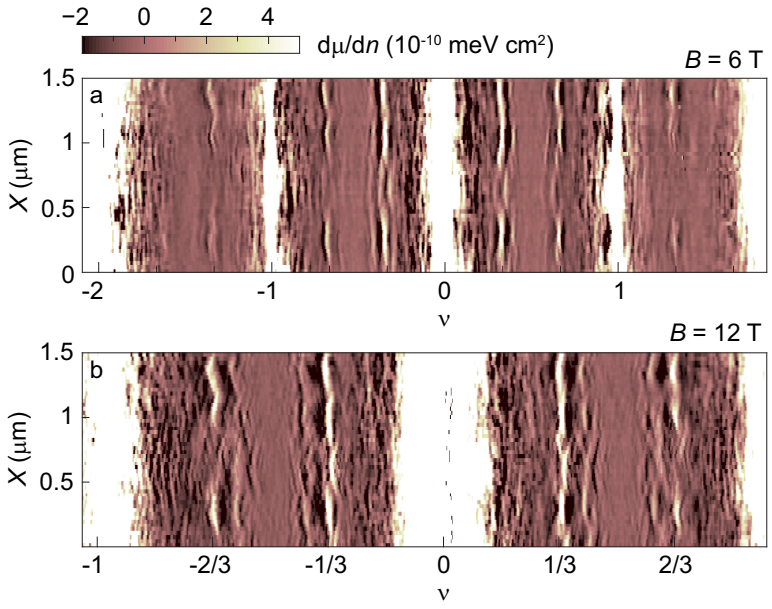

Figure 4.4: $d\mu/dn$ as a function of filling factor and position X along the flake (red arrow in Fig. 4.1) at $B = 6$ T (a) and 12 T (b). At both fields, we observe density fluctuations and variations in the strength of the FQH states as a function of position. States at $\nu = 2/3$ and 4/3 appear more susceptible to disorder than does $\nu = 1/3$.

4.5 Spatial Dependence

All of the measurements described above were taken at one position. Line scans of the inverse compressibility as a function of filling factor and position at $B = 6$ and 12 T are shown in Figs. 4.4a,b, respectively. The gate voltages at which the incompressible peaks occur vary with position, which can be explained by local density fluctuations. The magnitude of these fluctuations is similar to the width of the FQH states and may explain why the FQHE has been so difficult to observe in transport studies: Different regions of the sample form a given FQH state at different back-gate voltages. Figure 4.4 also shows that incompressible peak magnitude fluctuates substantially as a function of position. Although some incompressible states, such as those at $\nu = 1/3$, persist at virtually all positions, others are more susceptible to disorder. Both $\nu = 2/3$ and 4/3 fully disappear in some locations, which seem to be correlated with the areas where the integer quantum Hall states are

wider, a sign that local disorder is comparatively large. Despite the existence of disordered regions, the ability to perform local measurements reveals a multitude of FQH states in the cleanest areas. The observation of incompressible behavior at multiples of $\nu = 1/9$ indicates a substantial improvement in sample quality; together with the unconventional pattern of FQH states, this shows that graphene provides an especially rich platform in which to investigate correlated electronic states and their interplay with underlying symmetry.

Acknowledgments

We thank M. T. Allen for useful discussions and for helping to current anneal the device and B. I. Halperin, D. Abanin, J. K. Jain, S. das Sarma, J. Martin, V. Venkatachalam, S. Hart, and G. Ben-Shach for helpful discussions. This work is supported by the U.S. Department of Energy, Office of Basic Energy Sciences, Division of Materials Sciences and Engineering, under award no. DE-SC0001819. J.H.S. and B.K. acknowledge financial support from the Deutsche Forschungsgemeinschaft graphene priority program, and B.K. acknowledges financial support from the Bayer Science and Education Foundation. This work was performed in part at the Center for Nanoscale Systems (of Harvard Univ.), a member of the National Nanotechnology Infrastructure Network, which is supported by the NSF under award no. ECS-0335765.

4.6 Methods

The sample and tip fabrication procedures are outlined in Appendices A and B. The sample was measured in a ^{3}He cryostat, and was cleaned by current annealing. All measurements were performed at approximately 450 mK. The back gate voltage was limited to ± 10 V to avoid structural damage to the device. The sample whose data appears in this

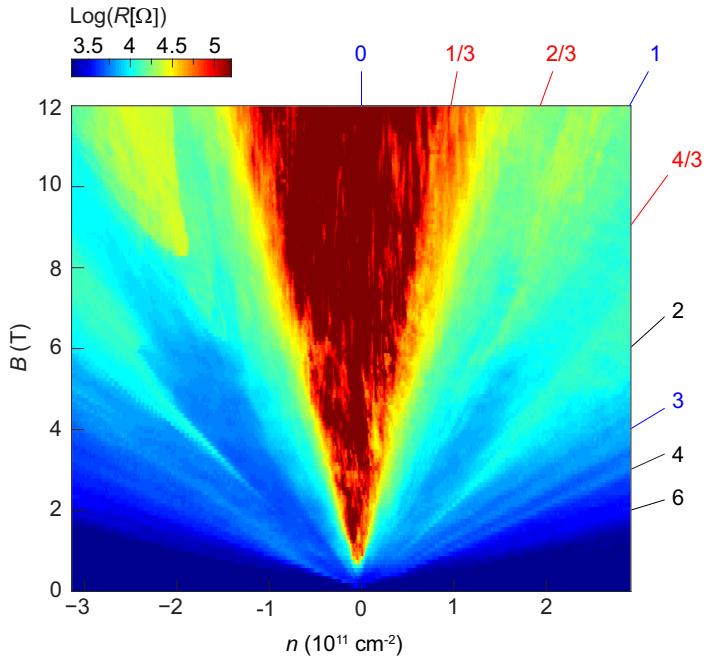

Figure 4.5: Sample resistance as a function of carrier density n and magnetic field B. Numbers and solid slanted lines at the edge of the plot indicate selected filling factors ν.

paper is a monolayer-bilayer hybrid. Its size is 3.5 μm in width (the monolayer portion is 2 μm), and 1 μm in length (*i.e.* distance between contacts). All the local measurements reported in the main text were conducted on the monolayer side of the flake, approximately 1.3 μm from the monolayer-bilayer interface and 500 nm from the electrical contacts. The electrical leads of the tip were 16 nm thick, and the island was 7 nm. The SET diameter was approximately 100 nm, and it was held 50-150 nm above the graphene flake during measurements.

4.7 Supplementary Discussion

4.7.1 Electronic transport

The sample discussed in this paper is a hybrid consisting of monolayer and bilayer graphene regions in parallel. Figure 4.5 shows the two-terminal resistance of the device

as a function of carrier density n and magnetic field B. We observe several quantum Hall features, with resistance maxima occurring at $\nu = 0$, 1, 2, 3, 4 and 6. This sequence includes the strongest monolayer and bilayer states, consistent with previous measurements [119]. Conductance plateaus at approximately the expected quantized value occur at filling factors $\nu = 1$ and 2 suggesting that both the monolayer and bilayer sides are simultaneously in a fully developed quantum Hall state. Conductance is also suppressed strongly at the charge neutrality point, with resistance reaching approximately 1 MΩ. However, no oscillations in resistance occur at fractional filling factors. This likely reflects the charge inhomogeneity in the sample, as discussed in the main text. It is worthwhile to note that in transport, the resistive region at $\nu = 0$ is so wide that it envelops $\nu = 1/3$, even though $\nu = 1/3$ is visible at virtually all positions along the monolayer in local compressibility measurements.

4.7.2 Effects of current annealing

The data presented in the main text were taken after two rounds of current annealing, and the sample changed substantially as a result of each current annealing step. Below, we discuss the progression of flake behavior associated with these cleaning procedures. Figures 4.6-4.9 show data prior to current annealing, and Figs. 4.10 and 4.11 display data taken after gentle current annealing. Even before current annealing the device, incompressible fractional quantum Hall (FQH) states were visible. FQH states are clearly distinguishable in Fig. 4.6 above 5-6 T, although the incompressible peaks are not nearly as pronounced, and localized states significantly modulate their apparent strength. The increased disorder is particularly evident in the breadth of localized states surrounding $\nu = 2$, which obscure all FQH states above $\nu = 4/3$. Figures 4.7a,b show spatial maps at $B = 8$ and 12 T, respectively, and the average compressibility over these spatial regions is plotted in Fig. 4.7c. Incompressible behavior is only evident at multiples of $\nu = 1/3$, but the data reveal

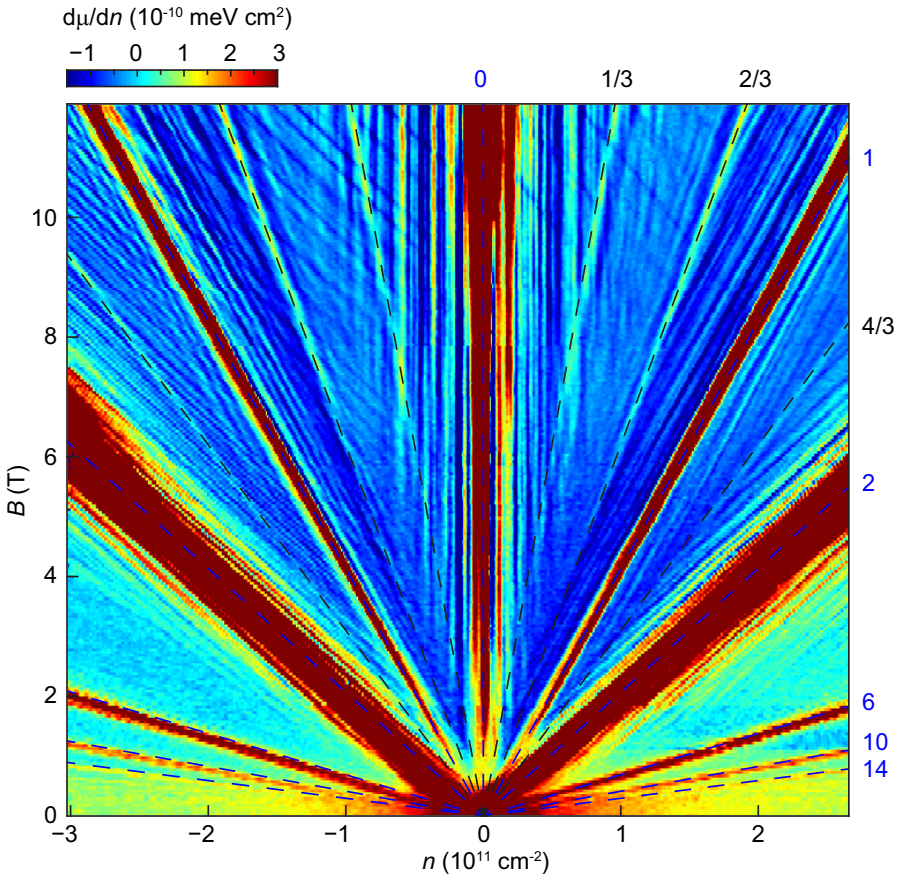

Figure 4.6: Inverse compressibility $d\mu/dn$ as a function of filling factor and magnetic field. Incompressible FQH states emerge around 5-6 T. Localized states associated with $\nu = -2$ are especially broad.

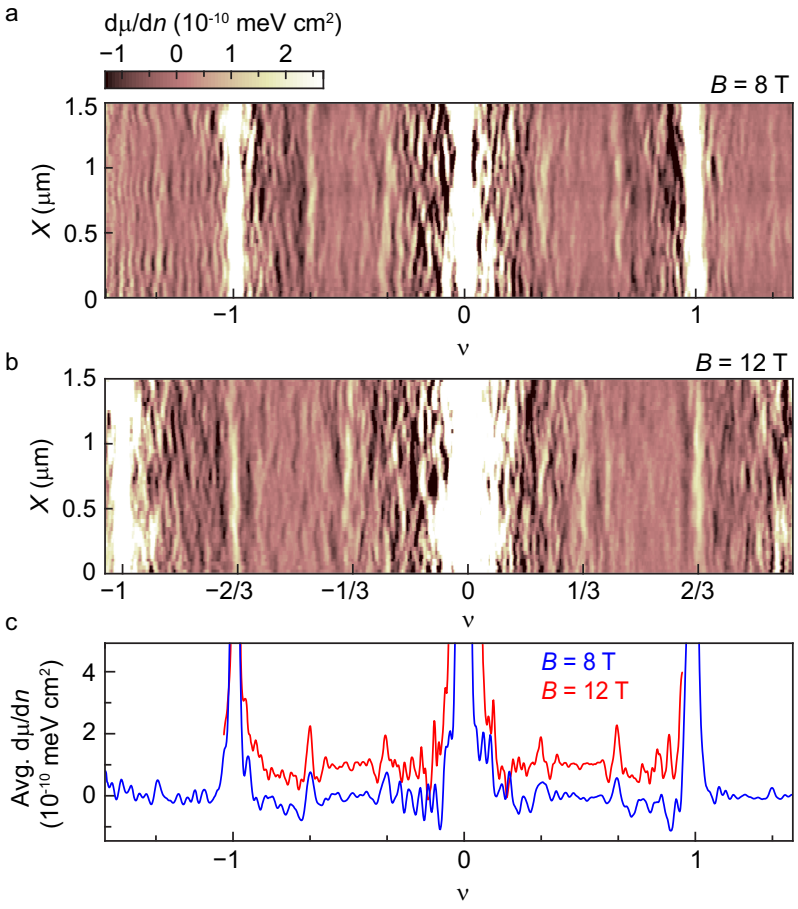

Figure 4.7: $d\mu/dn$ as a function of filling factor and position X along the flake at $B = 8$ T (a) and 12 T (b). (c) Spatial average of $d\mu/dn$ at 8 T (blue) and 12 T (red). Curves are offset for clarity.

relatively homogeneous strength of each FQH state as a function of position, particularly compared to that presented in Fig. 4.4.

Finer measurements which reveal FQH states at $\nu = 1/3$, $2/3$, $4/3$, $2/5$, $3/5$ and $4/7$ are shown in Figs. 4.8a,b. A three-dimensional rendering of the high-field data is plotted as a function of filling factor in Fig. 4.8c, and the average of inverse compressibility over this field range can be seen Fig. 4.8d. Interestingly, the incompressible behavior at $\nu = 2/3$ persists to lower fields than $\nu = 1/3$, and the same is true for $\nu = 3/5$ with respect to $\nu = 2/5$. This is the opposite behavior from that observed after current annealing.

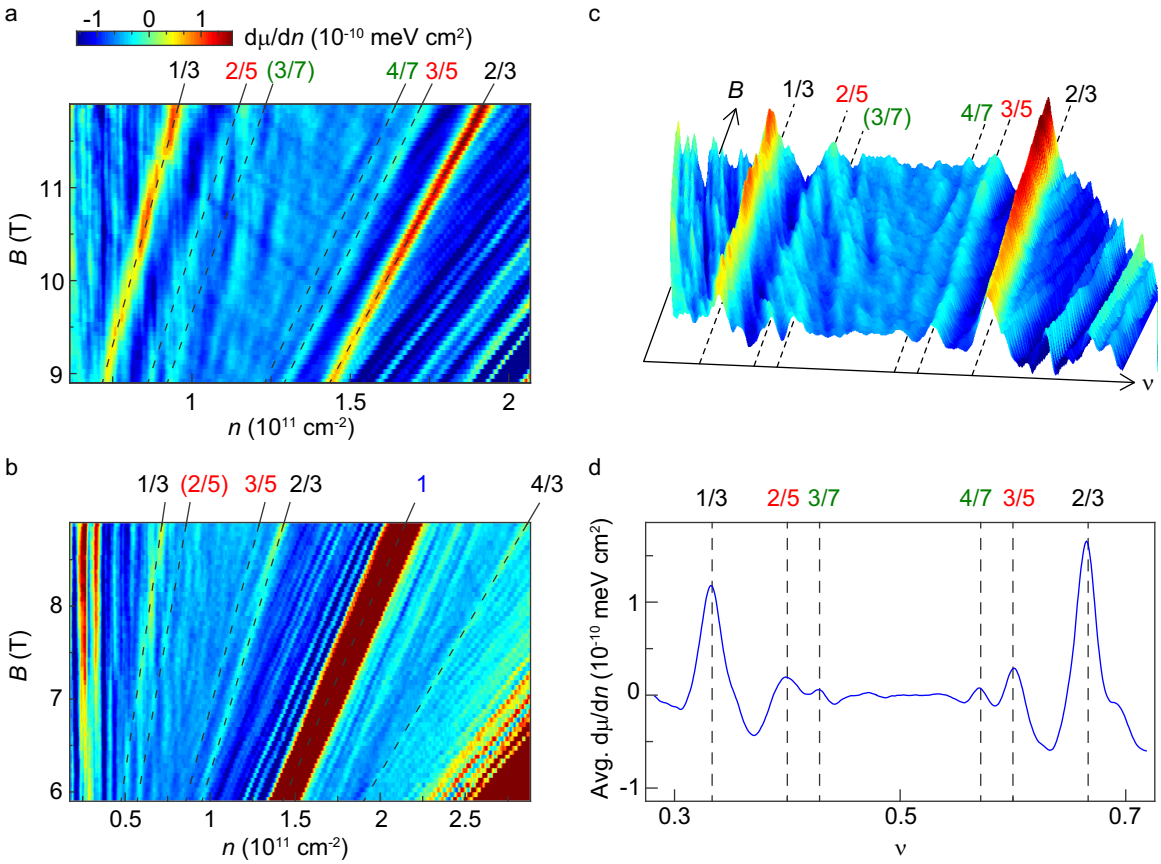

Figure 4.8: FQH states prior to current annealing. (a) and (b) Spatial average of $d\mu/dn$ as a function of carrier density and magnetic field taken at six different locations. Incompressible states occur at $\nu = 1/3$, $2/3$, $2/5$, $3/5$ and $4/7$ which are marked by dashed lines. Despite the averaging, localized states parallel to $\nu = 0$ and 1 are still visible and modulate the apparent amplitude of the fractional states. (c) 3D rendering of the data in (a) plotted as a function of filling factor. In this rendering, localized states appear as curved compressibility oscillations rather than straight lines. (d) $d\mu/dn$ as a function of filling factor, averaged over the field range shown in (a).

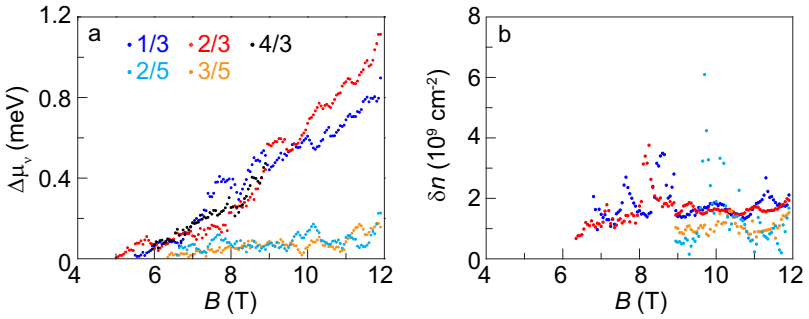

Figure 4.9: (a) Steps in chemical potential of each FQH state as a function of magnetic field. Gap size depends primarily on the denominator of the filling factor. (b) Incompressible peak widths of each FQH state, which are not strongly dependent on magnetic field. Data were taken prior to current annealing.

The data presented in Fig. 4.8 are actually an average over measurements performed at six different locations, each separated by about 200 nm. Spatial averaging mitigates the fluctuations in compressibility caused by localized states to some degree. Nonetheless, the incompressible peaks at $\nu = 1/3$ and $2/5$ are still strongly modulated by localized states, which may explain why they disappear at higher fields than their counterparts near $\nu = 1$ with the same denominator.

The steps in chemical potential $\Delta\mu_\nu$ and incompressible peak widths δn associated with each FQH state prior to current annealing are shown in Fig. 4.9. The extracted values of $\Delta\mu_\nu$ were smaller before annealing for all states, with $\Delta\mu_{1/3}$ and $\Delta\mu_{2/3}$ reaching only 1 meV at 12 T. Moreover, the steps in chemical potential depended primarily on filling factor denominator, with no differences evident over the fluctuations caused by localized states. All incompressible FQH peaks had similar widths, but they were slightly wider than after current annealing, indicating increased charge inhomogeneity.

We next gently current annealed the sample, applying only 1 V between contacts. This had no effect on electronic transport, but dramatically improved sample quality. The data reveal additional incompressible FQH states at $\nu = 8/5$, $3/7$ and $10/7$, and a large increase

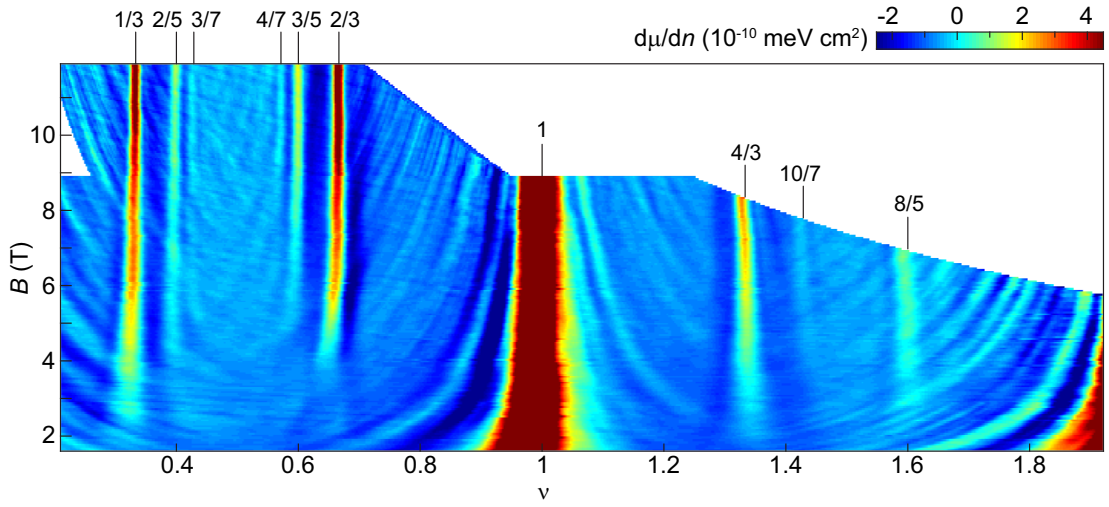

Figure 4.10: Inverse compressiblity as a function of filling factor and magnetic field after gentle current annealing. Clear incompressible peaks occur at $\nu = 1/3$, $2/3$, $2/5$, $3/5$, $3/7$, $4/7$, $4/3$, $8/5$ and $10/7$. Few localized states are visible due to the decreased sample disorder and the relatively large excitation in density: approximately 1.5×10^9 cm^{-2}, which is identical to that used to take the data in Figs. 4.6-4.8, but 2.5 times larger than was used in the measurements presented in the main text.

in the magnitude of the incompressible peaks associated with other FQH states (Fig. 4.10). Each incompressible state persists to lower field as well, with $\nu = 1/3$, $4/3$ and $8/5$ all visible at 2 T. It is worthwhile to note that $\nu = 2/3$ is less robust, disappearing around 4 T, consistent with the diminished gap observed around 3.5 T after the second round of current annealing. The step in chemical potential associated with each FQH state increased as a result of current annealing as well, with $\Delta\mu_{1/3}$ reaching 2.5 meV and $\Delta\mu_{3/5}$ reaching 0.7 meV at 12 T (Fig. 4.11a). Moreover, the incompressible peak magnitude remained approximately independent of position, as illustrated in Fig. 4.11b.

We then current annealed the sample a second time, applying 1.32 V between contacts. Although we did not record the exact resistance or current through the device during this process, we can estimate a flake resistance of about 1 kΩ, and use this to obtain an approximate current density of 0.38 mA/μm. The data in the main text were taken after

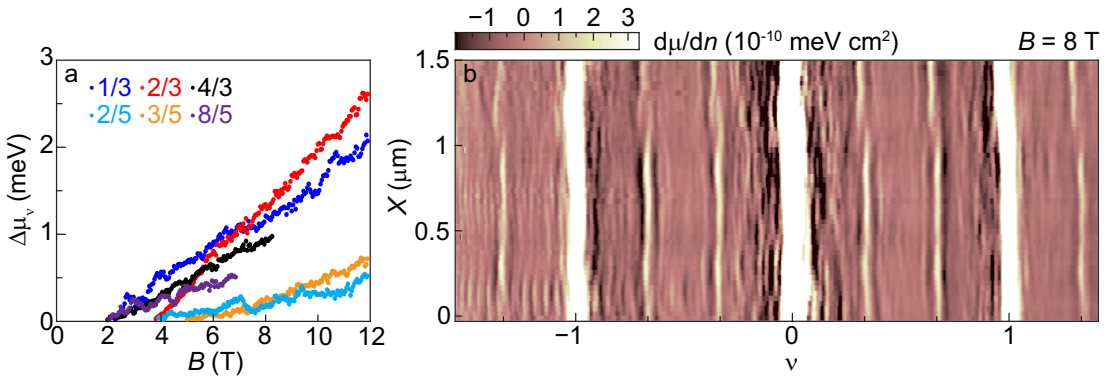

Figure 4.11: (a) Steps in chemical potential of each FQH state as a function of magnetic field after gentle current annealing. (b) $d\mu/dn$ as a function of filling factor and position X along the flake at $B = 8$ T after gentle current annealing. Incompressible peaks are visible at $\nu = 1/3$, $2/5$, $3/5$, $2/3$ and $4/3$, and sample behavior varies only moderately with position.

this current annealing step. For completeness, we show in Fig. 4.12 the spatial average of inverse compressibility from Figs. 4.4a,b.

4.7.3 Determination of the offset in inverse compressibility

Due to the finite size of the sample, some fringing fields from the back gate directly affect the SET, giving rise to a constant positive offset in the measured inverse compressibility. To accurately extract $\Delta\mu_\nu$ of each FQH state, this parasitic capacitance must be taken into account. Determining the zero of $d\mu/dn$ is further complicated because interactions among charge carriers produce a negative contribution to the inverse compressibility that depends on magnetic field [57]. Figure 4.13 shows the average inverse compressibility as a function of magnetic field for the filling factor ranges $0.45 < \nu < 0.55$ and $1.45 < \nu < 1.55$. The inverse compressibility in both ranges is similar, and is fit well by $d\mu/dn \sim -B^{-1/2}$ dependence, as expected for interacting particles with density $n \propto B$. The fit to these curves is used to define $d\mu/dn = 0$ at each field for the extraction of $\Delta\mu_\nu$. Figures showing linecuts of $d\mu/dn$ as a function of density also follow the convention that $d\mu/dn = 0$ at $\Delta\mu_\nu = 1/2$. However,

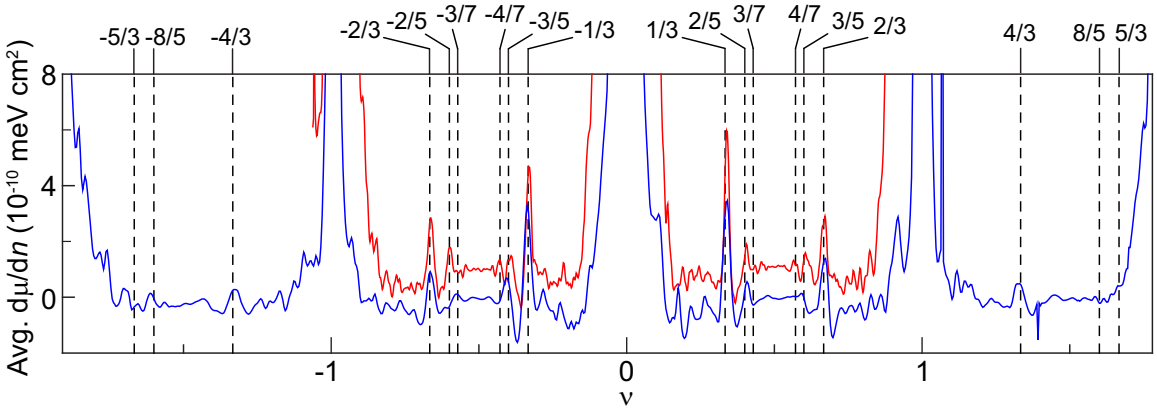

Figure 4.12: Average $d\mu/dn$ as a function of position from the data presented in Figs. 4.4a (blue) and b (red). Curves are offset for clarity.

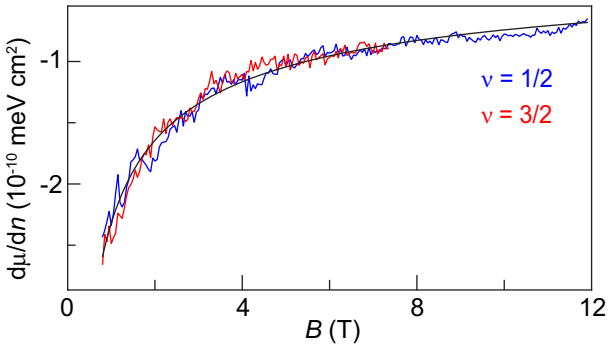

Figure 4.13: Average inverse compressibility as a function of magnetic field for the filling factor ranges 0.45-0.55 (blue) and 1.45-1.55 (red). The data are well fit by $B^{-1/2}$ dependence, as shown by the black fit. The black fit is used to determine $d\mu/dn = 0$ for the purpose of FQH gap size extraction at each field.

the inverse compressibility in color plots is defined so that $d\mu/dn = 0$ in the compressible regions associated with Landau levels at filling factors $\nu > 2$ (*e.g.* at $\nu = 3.5$).

4.7.4 Comparison with theoretically predicted energy gaps

Table 4.1 lists the theoretically predicted energy gaps Δ_ν of several FQH states, and compares our measurements with the predicted values at the highest experimentally accessible field. To the best of our knowledge, no quantitative predictions are available for the other FQH states that we observe. In Table 4.1, the theoretically predicted values assume

Table 4.1: Summary of FQH energy gaps. Theoretical predictions for energy gap size at the highest experimentally accessible magnetic field are compared with the corresponding measured and extrapolated values. Experimental and extrapolated values assume that the charge of the quasiparticles involved is given by the electron charge divided by the denominator of the filling factor.

ν	Theoretically predicted Δ_ν	Predicted Δ_ν at largest B (meV)	Experimental Δ_ν at largest B (meV)	Extrapolated Δ_ν at largest B (meV)
1/3	$(0.03\text{-}0.1)e^2/\epsilon l_B$ [96, 97, 99, 101] [102, 104, 107]	1.3-4.3 (at 12 T)	1.2	1.5
2/3	$(0.08\text{-}0.11)e^2/\epsilon l_B$ [102]	3.5-4.8 (at 12 T)	1	1.5
4/3	$(0.08\text{-}0.11)e^2/\epsilon l_B$ [102, 107]	2.8-3.9 (at 8 T)	0.5	0.75
2/5	$(0.04\text{-}0.051)e^2/\epsilon l_B$ [97, 102, 107]	1.7-2.2 (at 12 T)	0.2	0.4
8/5	$(0.02\text{-}0.051)e^2/\epsilon l_B$ [97, 102, 107]	0.7-1.7 (at 7 T)	0.15	-
14/9	$0.019e^2/\epsilon l_B$ [107]	0.6 (at 7 T)	0.02	-

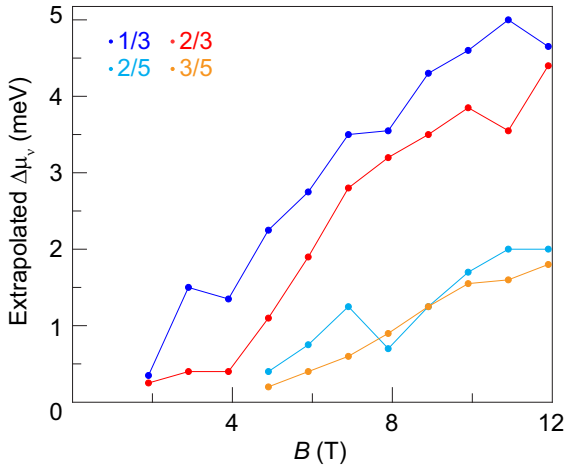

Figure 4.14: Steps in chemical potential at $\nu = 1/3$ (blue), 2/3 (red), 2/5 (cyan) and 3/5 (orange) obtained by linearly extrapolating the negative compressibility surrounding each FQH state, as illustrated in red in Fig. 4.3a. Lines between data points are guides to the eye.

a dielectric constant of 4.5 in suspended graphene [120] and the extracted experimental values assume that the quasiparticle charge is given by the electron charge divided by the filling factor denominator. As stated in the main text of the manuscript, the energy gaps that we extract from our measurements are smaller than theoretically predicted. Even if we linearly extrapolate the negative slope in $\mu(n)$ surrounding each state (red lines in Fig. 4.3a) to mitigate the effects of disorder [118], the discrepancy persists for all FQH states except $\nu = 1/3$. The extrapolated steps in chemical potential at select magnetic fields are summarized for $\nu = 1/3$, 2/3, 2/5 and 3/5 in Fig. 4.14.

From Fig. 4.3b, we extract an energy gap $\Delta_{1/3} \approx 1.2$ meV at $B = 12$ T, only slightly below the range specified by theoretical predictions. From the extrapolated values in Fig. 4.14, we obtain an estimate $\Delta_{1/3} \approx 1.5$ meV, which is within the range spanned by theoretical predictions. In contrast, even the extrapolated $\Delta_{2/3} \approx 1.4$ meV is still 2-3 times smaller than theoretically predicted. Similarly, the estimated value of $\Delta_{2/5}$ from the extrapolation in Fig. 4.13 is only about 0.4 meV at $B = 12$ T, approximately 4-5 times smaller than

theoretically predicted. Although the extrapolated steps in chemical potential at $\nu = 4/3$ are not shown in Fig. 4.14, $\Delta_{4/3} \approx 0.75$ meV at 8 T, about 4-5 times smaller than the theoretical prediction. Finally, we note that linear extrapolation was not possible at $\nu = 8/5$ or 14/9, but the energy gaps at these filling factors are also significantly smaller than expected.

4.7.5 Reproducibility and ruling out extrinsic effects

The results described in the main text are reproducible, independent of tip position or amount of current annealing, and they cannot be explained by extrinsic effects. Although disorder is present and we see local variations in quality, this only changes the behavior we observe quantitatively and not qualitatively. Below, we present additional measurements from several locations and rule out spurious effects associated with the monolayer-bilayer interface, the electrical contacts, current annealing, and strain.

Although all measurements were performed on a single device, the local nature of our technique allows us to effectively probe multiple independent samples simply by moving the tip to different locations. This helps distinguish localized states, whose spectrum varies with position, from FQH states, which are robust, and also provides corroborating evidence for the overarching picture we observe. We use three key metrics to determine whether a given incompressible peak should be labeled as a FQH state. First, we require that the incompressible peak should appear vertical in a plot vs. filling factor over a large (at least 3 T) range in magnetic field. Over smaller field ranges, the curvature of a localized state may not be apparent. Second, we only label incompressible peaks as FQH states if they are reproducible in multiple locations. Finally, we check if the slope of an incompressible peak in the n-B plane can be reasonably matched to a nearby quantum Hall state, and if so, we ascribe these features to localized states.

The measurements presented in Figs. 4.2, 4.6 and 4.10 were all performed at different positions. Additional measurements at different locations are shown in Fig. 4.15. The data in these figures reveal different patterns of localized states, but qualitatively similar behavior to that presented in the main text. Specifically, odd-numerator FQH states are absent or significantly suppressed between $\nu = 1$ and 2, and the compressibility is approximately symmetric about $\nu = 1/2$ for $0 < \nu < 1$.

We can rule out that the bilayer portion of the device affects the behavior that we observe. First, the measurements presented in the main text were performed far (1.3 μm = 50-175 magnetic lengths between 1 and 12 T) from the monolayer-bilayer interface. Band bending associated with the interface is only expected to persist a few magnetic lengths into the monolayer side [121], and therefore would not affect the local measurements in Figs. 4.1 and 4.2. Moreover, the spatial scans in Figs. 4.4, 4.7 and 4.11 show that sample behavior is not sensitive to distance from the interface, which sits at approximately X = -100 nm.

We can also eliminate doping from the contacts as a potential influence on the behavior that we observe. Measurements in the main text were performed approximately 500 nm from the contacts, whereas contact doping is only found to extend 200-300 nm into the flake [122]. Although we have not imaged within 200 nm of the contacts because it jeopardizes the scanning SET tip, we have performed measurements in which we vary the distance between tip and contact, and we do not observe systematic differences in sample behavior (Fig. 4.16). These measurements span the entire width of the flake, and approximately 600 nm in length (*i.e.* distance between contacts). For all locations we have imaged, the charge neutrality point occurs within 0.5 V of zero back gate voltage. This suggests that there is practically no doping of the sample, which also excludes doping from the contacts.

We can also explicitly rule out that current annealing had unintended consequences. We have imaged the entire sample after each current annealing step, and no portions of the

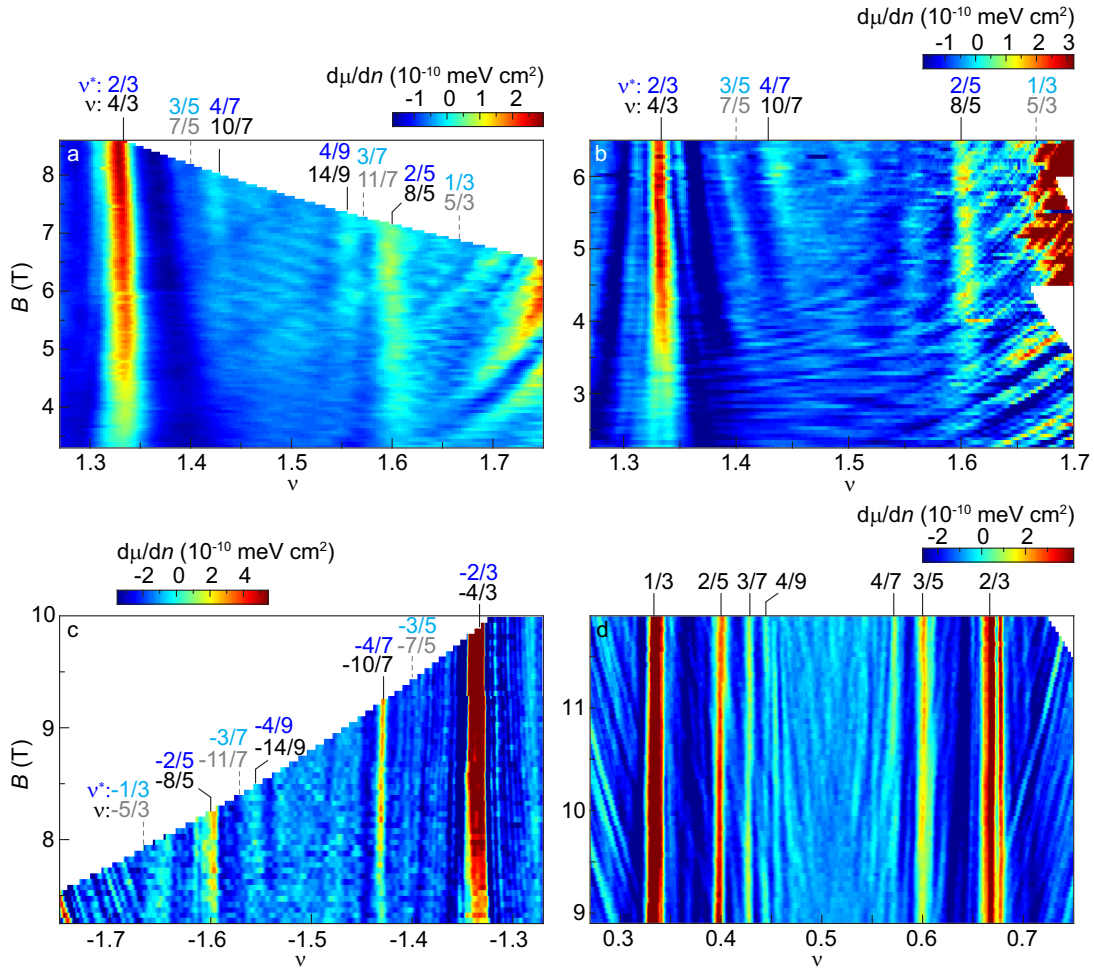

Figure 4.15: Measurements at additional positions. (a)-(c) $d\mu/dn$ in several positions as a function of magnetic field over the filling factor range between $|\nu| = 1$ and 2. The spectra of localized states changes, but the pattern of FQH states is robust. In panel (b), only states at $\nu = 4/3$ and $8/5$ are visible, indicating decreased sample quality, but the absence of odd-numerator states remains. Panel (c) shows a measurement on the hole side after a third current annealing step. Odd-numerator FQH states are absent, except a small peak around $\nu = -1.65$, which may indicate a weak state at $\nu = -5/3$. (d) $d\mu/dn$ as a function of magnetic field and filling factor for $\nu < 1$. The spectra of localized states is different from Fig. 4.2a, but the pattern of FQH states is robust. The incompressible peak just to the right of $\nu = 4/9$ does not occur at the same filling factor as in Fig. 4.2a.

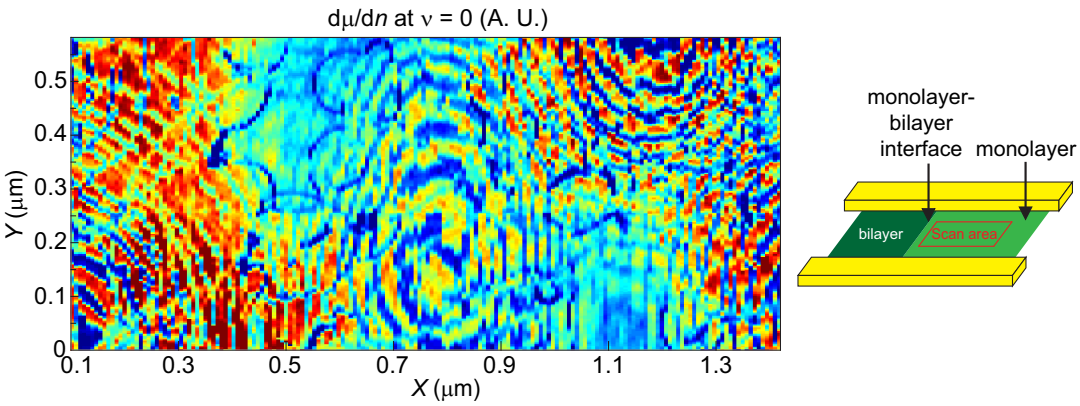

Figure 4.16: $d\mu/dn$ at $\nu = 0$ as a function of X and Y position, as illustrated in the schematic on the right. Sample behavior is independent of distance to the electrical contacts and distance from the monolayer-bilayer interface (which sits at $X \approx -100$ nm). The dips in $d\mu/dn$ correspond to the population of individual electrons into localized states confined to disorder puddles. Units are not given for $d\mu/dn$ because the high $\nu = 0$ resistance artificially enhances the measured inverse compressibility.

flake have been removed or destroyed. The qualitative picture we observe is also insensitive to the amount of cleaning performed. Even before current annealing the flake, we observed several FQH states, and their sequence was consistent with absent odd-numerator states between $\nu = 1$ and 2, but full symmetry breaking between $\nu = 0$ and 1. Upon subsequent current annealing steps, we saw additional FQH states, and their energy gaps increased, but the overarching pattern remained unchanged. Based on the continuity of our observations throughout many current annealing steps, including those before any cleaning, we exclude current annealing as an explanation for the behavior we observe.

Finally, we discuss the effects of strain, which is another form of disorder. Though we cannot explicitly rule out that strain may be present in the device, we note that it likely varies from one location to another, whereas the picture we observe is robust. Moreover, heating during current annealing is likely to cause strain to relax, heighten, or otherwise change, whereas the qualitative behavior we observe is insensitive to the amount of current annealing that we perform. Finally, we note that we can probe height variations in the

sample. We observe ripples of about 1 nm peak-to-peak amplitude and 400 nm wavelength. These are relatively small, indicating that out of plane strain is small. Moreover, these features do not appear to be correlated with sample behavior. Based on all these observations, we conclude that strain is not a likely explanation for the behavior that we observe. It is also worthwhile to note that even if strain breaks valley symmetry, it is not clear why it would have different effects above and below $\nu = 1$.

Chapter 5

Fractional Quantum Hall Phase Transitions and Four-Flux States in Graphene

Graphene and its multilayers have attracted considerable interest because their four-fold spin and valley degeneracy enables a rich variety of broken-symmetry states arising from electron-electron interactions and raises the prospect of controlled phase transitions among them. Here we report local electronic compressibility measurements of ultraclean suspended graphene that reveal a multitude of fractional quantum Hall states surrounding filling factors $\nu = -1/2$ and $-1/4$. Several of these states exhibit phase transitions that indicate abrupt changes in the underlying order, and we observe many additional oscillations in compressibility as ν approaches $-1/2$, suggesting further changes in spin and/or valley polarization. We use a simple model based on crossing Landau levels of composite fermions with different internal degrees of freedom to explain many qualitative features of the experimental data. Our results add to the diverse array of many-body states observed

in graphene and demonstrate substantial control over their order parameters, establishing graphene as an excellent platform to study correlated electron phases of matter.

5.1 Introduction

When a two-dimensional electron gas is subject to a perpendicular magnetic field B, the electronic spectrum forms a sequence of Landau levels (LLs), which can accommodate one electron per flux quantum for each internal electronic state. Generally, this gives rise to incompressible quantized Hall states at integer values of the filling factor $\nu = nh/eB$, where n is the carrier density, h is Planck's constant and e is the electron charge. In very clean samples at high magnetic field, Coulomb interactions become important and produce additional quantized Hall states at certain fractional filling factors [2, 49, 50, 52]. These fractional quantized Hall (FQH) states can be understood in terms of so-called composite fermions (CFs), which may be described as an electron bound to an even number m of magnetic flux quanta. CFs with $m = 2$ (^{2}CFs) experience a reduced effective magnetic field proportional to $(\nu - 1/2)$, and FQH states at $\nu = p/(2p \pm 1)$ are understood to arise when an integer number p of ^{2}CF LLs are occupied. In CF theory, FQH states of electrons are therefore interpreted as the integer quantized Hall effect of these new composite particles [52].

Like electrons, CFs can have internal quantum numbers such as spin or valley index (isospin). When more than one CF LL is occupied, ground states with different polarizations of these degrees of freedom are possible at a given filling factor, and transitions between different phases may occur when system parameters are varied. Phase transitions between FQH states with differing spin polarization have been observed in GaAs by tuning the magnitude of the magnetic field [123–126], its direction [127–132], or the applied pressure

[133]. In AlAs 2DEGs, strain has been used to induce phase transitions between valley-polarized and unpolarized states [114, 115, 117].

In graphene, the electronic Hamiltonian has an approximate SU(4) symmetry arising from the spin and valley degrees of freedom. This symmetry is weakly broken due to the Zeeman effect and electron-electron scattering between valleys, which may be enhanced by (or compete with) effects of the dominant Coulomb interactions. Electron-electron interactions were recently shown to produce surprising patterns of symmetry breaking and phase transitions in the integer quantum Hall regime [41, 48, 90–92]. Theoretical proposals suggest that the strengths of FQH states can also be tuned in monolayer and bilayer graphene, and that transitions between different ordered phases are possible [106, 134, 135]. However, despite the observation of robust FQH states in graphene [53, 109–111, 136, 137], their rich phase diagram has yet to be fully explored.

Here we report local electronic compressibility measurements of suspended graphene, performed using a scanning single-electron transistor (SET) [77, 78], which reveal a succession of FQH phase transitions as well as four-flux CF (^{4}CF) states. A schematic of the measurement setup is shown in Fig. 5.1a (see also Section 5.6). Modulating the carrier density with a back gate and monitoring the resulting change in SET current allows us to measure both the local chemical potential μ and the local inverse compressibility of the graphene flake with a spatial resolution of approximately 100 nm. The inverse compressibility κ^{-1} is properly defined as $n^2 d\mu/dn$, but hereafter we drop the prefactor and use the term to mean $d\mu/dn$. The data presented below were taken at one location, but similar behavior was observed at multiple positions (see Section 5.7).

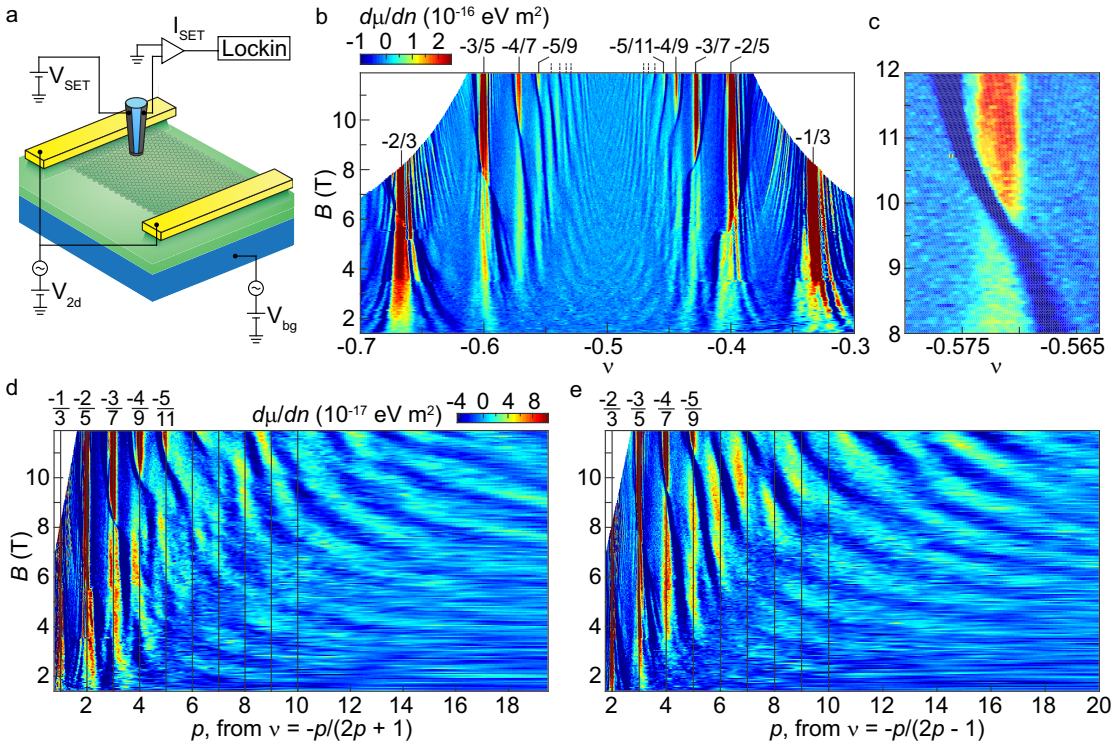

Figure 5.1: (a) Schematic of the measurement setup. (b) Inverse compressibility $d\mu/dn$ as a function of filling factor ν and magnetic field B. Phase transitions occur for all fractional quantum Hall (FQH) states except $\nu = -1/3$. (c) Finer measurement around $\nu = -4/7$ showing the negative compressibility and peak splitting associated with the phase transition. Panels (b) and (c) have identical color scales. (d) and (e) $d\mu/dn$ as a function of B and composite fermion Landau level (CF LL) index p. Panels (d) and (e) have identical color scales, and both show oscillations in compressibility that persist very close to $\nu = -1/2$. Principal FQH states are marked by black lines and are labeled. The dashed lines in panel (b) mark where higher-denominator FQH states in the standard CF sequence would be expected to occur.

5.2 FQH Phase Transitions

Figure 5.1b shows the inverse compressibility as a function of filling factor and magnetic field. FQH states appear as vertical incompressible peaks at $\nu = -1/3$, $-2/3$, $-2/5$, $-3/5$, $-3/7$, $-4/7$, $-4/9$, $-5/9$ and $-5/11$, consistent with the standard CF sequence observed for $|\nu| < 1$ in previous measurements [137] (we focus on $\nu < 0$ because the QH features are slightly better developed than for $\nu > 0$) . Surprisingly, every FQH state except $\nu = -1/3$ exhibits a narrow magnetic field range over which the incompressible behavior is strongly suppressed and the energy gap decreases. The critical field at which this occurs increases with filling fraction denominator, and the suppression is associated with regions of sharply negative compressibility that cross each FQH state, often generating two coexisting incompressible peaks at slightly different filling factors over a small range in magnetic field (Fig. 5.1c). Interestingly, the negative compressibility, which indicates a decrease in the electron chemical potential as electrons are added, has an especially large amplitude that is similar (but opposite in sign) to the incompressible peaks of the actual FQH states.

The interruptions in each incompressible peak suggest phase transitions in which the spin and/or valley polarization of electrons changes abruptly. The behavior is similar to that observed in GaAs, where transport measurements showed FQH states splitting into doublets near phase transitions [124,125,129,132]. However, no dramatic features of negative compressibility were present in GaAs [126], and the inverse compressibility did not display a strong asymmetry between filling factors just above and below the FQH states [19, 126].

Several less prominent modulations in compressibility that occur close to $\nu = -1/2$ are also visible in Fig. 5.1b. We emphasize that they are not caused by localized states, which occur near the strongest FQH states such as $\nu = -2/3$, but not around high-denominator states, such as $\nu = -4/7$ (see Section 5.7). Further insight can be gained by plotting the

inverse compressibility as a function of p rather than ν (Figs. 5.1d,e). Doing so more clearly illustrates the behavior near $\nu = -1/2$ and reveals oscillations in inverse compressibility that persist to values of p as large as 20 and magnetic fields as low as a few Tesla. We note that this behavior cannot be explained by Shubnikov de Haas oscillations of CFs, because variations in compressibility occur even at constant filling factor. The oscillations become stronger and more vertical as the magnetic field is increased, suggesting that they are associated with developing FQH states. Moreover, they seem to extend from the negative compressibility features of the phase transitions, suggesting that they result from changes in spin and/or valley polarization as magnetic field and filling factor are varied.

Signatures of phase transitions have previously been observed in compressibility measurements only at $\nu = 2/3$ in GaAs [126], although optical and transport studies of GaAs and AlAs have revealed evidence of changes in spin or isospin polarization for filling fractions with larger denominators [116,127]. We observe clear phase transitions up to $\nu = -5/9$ and $-5/11$, and additional compressibility oscillations are apparent much closer to $\nu = -1/2$. Similar oscillations have not been reported in GaAs; their existence in graphene suggests a rich array of ordered electronic states and hints at a delicate energetic competition among them. Graphene therefore offers an excellent platform to study electronic interactions and their dependence on underlying symmetry.

5.3 Model and Numerical Simulation

To gain further insight into the phase transitions, we introduce a simple model to describe CFs with internal degrees of freedom [99,100,107,138] (see Section 5.7 for details). Due to graphene's peculiar band structure, the lowest LL is already half-full at $\nu = 0$, and experiments suggest that the $\nu = 0$ state has no net spin polarization [41]. For $0 >$

$\nu > -1$, we assume that the ground state is obtained by putting holes in the $\nu = 0$ state, which we convert to CFs by attaching two flux quanta to each hole. The CFs have two possible spin states ($\pm$) and we consider many-body states where there may be different particle densities for the two spins. Single-particle energies of the two spin states will be split by an amount proportional to B due to the Zeeman effect, which favors a state where all the spins are aligned with the field. However, the SU(4)-invariant part of the Coulomb interaction will typically favor states with more equal occupation [107]. Because the Coulomb interaction energies scale as $B^{1/2}$, then for fixed ν, varying the magnetic field will change the relative importance of the two terms, which suggests that the experimentally observed phase transitions may be associated with changes in spin polarization, as in GaAs.

Our model applies most directly to the situation where all electrons in the ground state of $\nu = 0$ have the same valley configuration, as in the Kekule or the charge-density-wave states [43]. The antiferromagnetic state is more complicated because the constituent electron states differ in valley index as well as spin, but we expect that results for this case should be at least qualitatively similar to the case we consider [54]. Future studies in which a tilted magnetic field is applied to the sample may help determine the spin and valley ordering of the FQH states.

Within our model, effects of the SU(4)-invariant Coulomb interaction are modeled by a sum of the "kinetic energies" of the occupied states in the CF LLs, which scale as $B^{1/2}$ for fixed orbital index N^*. A schematic diagram of CF LL energies $E^{\pm}_{N^*}$ and their scaling with magnetic field is shown in Fig. 5.2a. At certain critical magnetic fields, CF LLs with different spin and orbital degrees of freedom cross, leading to phase transitions.

Based on this model, we have numerically simulated the inverse compressibility. In our simulation, we broaden the CF LLs by a fixed amount of disorder δn and calculate the occupation of each CF LL, which ultimately yields the inverse compressibility as a function

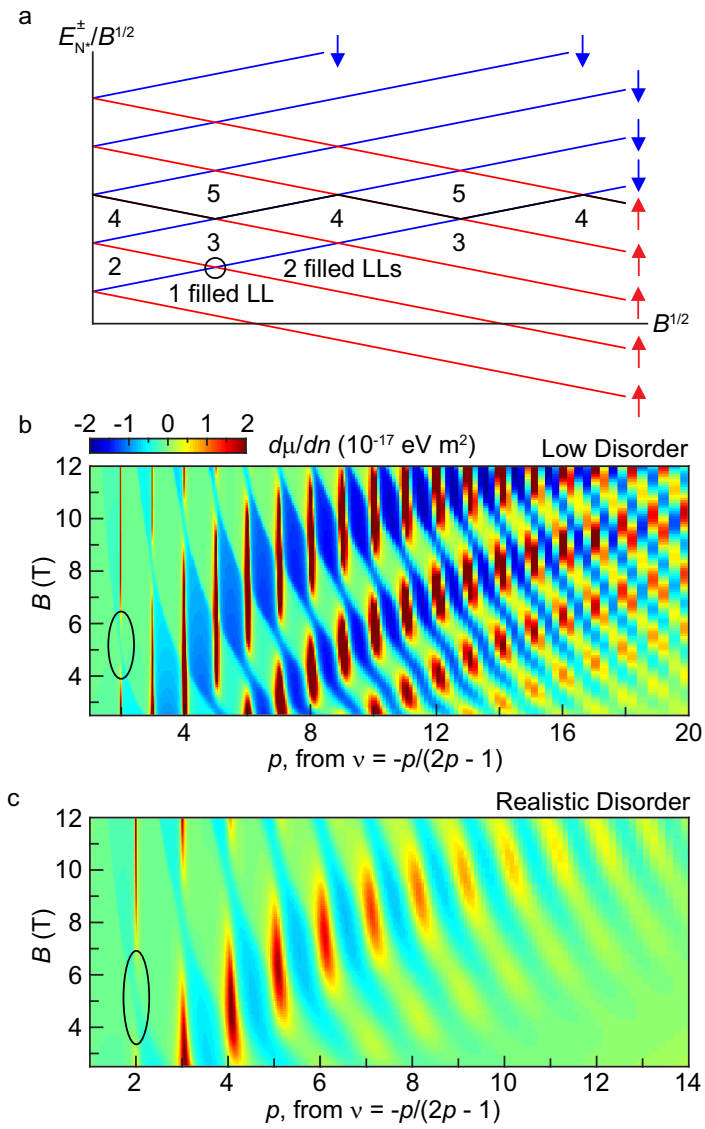

Figure 5.2: (a) Schematic of CF LL energies $E_p^{\pm}$ divided by and plotted against $B^{1/2}$. Crossings (black circle) between spin-up and down CF LLs (colored arrows) correspond to phase transitions. (b) and (c) Numerical simulations of $d\mu/dn$ as a function of B and p assuming either minimal charge inhomogeneity (b), or more realistic density fluctuations (c). Black ovals correspond to the black circle in panel (a). Both panels use the same color scale.

of density and magnetic field. The results, which assume either a small amount of disorder or more realistic density fluctuations based on the widths of the FQH peaks, are shown in Figs. 5.2b,c, respectively.

The simulations in Fig. 5.2 share many characteristics with the experimental data. Most striking are the breaks in the incompressible peaks of FQH states with $p \geq 2$, and the reasonably good agreement between the critical fields of these transitions in the simulation and their experimental counterparts. In addition, the simulations show regions of negative compressibility that cross from one side of the FQH state to the other as the phase transition occurs. This is qualitatively similar to the behavior that we observe, although the experimental features are much narrower. Finally, we note that the oscillations in inverse compressibility become less robust and start to curve at low magnetic field and high p, similar to the experimental data. The values used for parameters in the simulation agree well with expectations based on other experimental metrics. By matching the simulation to the experimental critical fields and assuming Zeeman splitting with a g factor of 2, we extract an effective mass $m^* = 0.18 m_e(\nu B[\mathrm{T}])^{1/2}$, the same order of magnitude as for CFs in GaAs [123]. In addition, the density fluctuations $\delta n = 1.5 \times 10^8$ cm^{-2} assumed in Fig. 5.2c are comparable to the widths of the FQH states we observe. Given the simplicity of the model, the agreement with experiment is remarkable, suggesting that it provides a basic framework to understand the underlying physics.

The critical fields of the phase transitions vary slightly with position, and a much smaller critical field at $\nu = 2/3$ was observed before the final current annealing step (see Section 5.7). The change after current annealing suggests that disorder is relevant, but the exact mechanism is not clear. Disorder that breaks valley symmetry could preferentially support one FQH phase over the other if the $\nu = 0$ state is a canted antiferromagnet. It

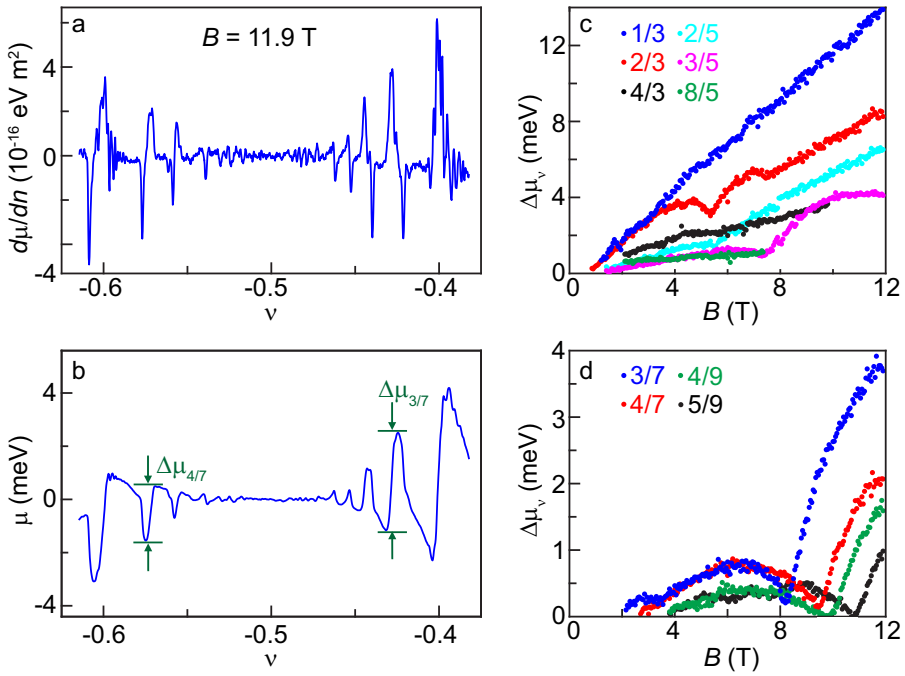

Figure 5.3: (a) $d\mu/dn$ as a function of ν at $B = 11.9$ T. (b) Chemical potential relative to its value at $\nu = -1/2$ as a function of ν at 11.9 T. (c) and (d) Steps in chemical potential $\Delta\mu_\nu$ [green labels in panel (b)] of FQH states as a function of B at measured multiples of $\nu = 1/3$ and $1/5$ (c), and $\nu = 1/7$ and $1/9$ (d). The non-monotonic dependence visible for several FQH states results from the phase transitions that they undergo.

is also possible that the level of disorder affects the dielectric constant. The origin of the spatial dependence merits further study.

5.4 Steps in Chemical Potential

Integrating the inverse compressibility with respect to carrier density allows us to extract the steps in chemical potential $\Delta\mu_\nu$ of each FQH state; multiplying $\Delta\mu_\nu$ by the quasiparticle charge then yields the corresponding energy gaps. Figures 5.3a,b show inverse compressibility and chemical potential, respectively, as a function of filling factor at 11.9 T. In Figs. 5.3c,d, we plot $\Delta\mu_\nu$ as a function of magnetic field. The complex non-monotonic behavior of the energy gaps exhibited by several FQH states (Fig. 5.3d) is similar to the

behavior in GaAs near phase transitions [131]. This behavior becomes increasingly pronounced and the field range over which incompressible behavior is suppressed widens as filling factor denominator increases. A similar pattern occurs in the simulations of Fig. 5.2, and it likely results from the increasing effects of density fluctuations on CF LL width as p increases.

The step in chemical potential at $\nu = -1/3$ scales linearly with B over the entire field range that we study. This behavior is consistent with prior studies [137], but the linearity is surprising because interaction-driven states typically scale as $B^{1/2}$. The behavior also contradicts the $B^{1/2}$ dependence expected from our model, although we note that the model does not include interactions among CFs, LL mixing, finite temperature effects, or the possibility of other excitations such as skyrmions. Linear scaling with magnetic field at $\nu = 1/3$ has been theoretically predicted to arise from spin-flip excitations over an intermediate field range [104].

5.5 Four-Flux Composite Fermion States

In addition to the phase transitions discussed above, the exceptional sample quality reveals several FQH states belonging to the ^{4}CF sequence $\nu = p/(4p \pm 1)$ and its analogue around $\nu = -1$ for the first time in graphene. We observe incompressible behavior at $\nu = -1/5, -2/7, -2/9, -3/11, -5/7$ and $-6/5$ (Figs. 5.4a-c). An additional weak incompressible peak occurs between $\nu = -9/7$ and $-14/11$, but the experimental uncertainty in filling factor prevents a more precise assignment (see Section 5.7). No other ^{4}CF states are visible; FQH states at $\nu = -4/5, -9/5$ and $-12/7$ are conspicuously absent, despite the robust appearance of their counterparts near $\nu = 0$. This may reflect interesting patterns of symmetry-breaking in the lowest LL [137,139], but could also be caused by differing degrees

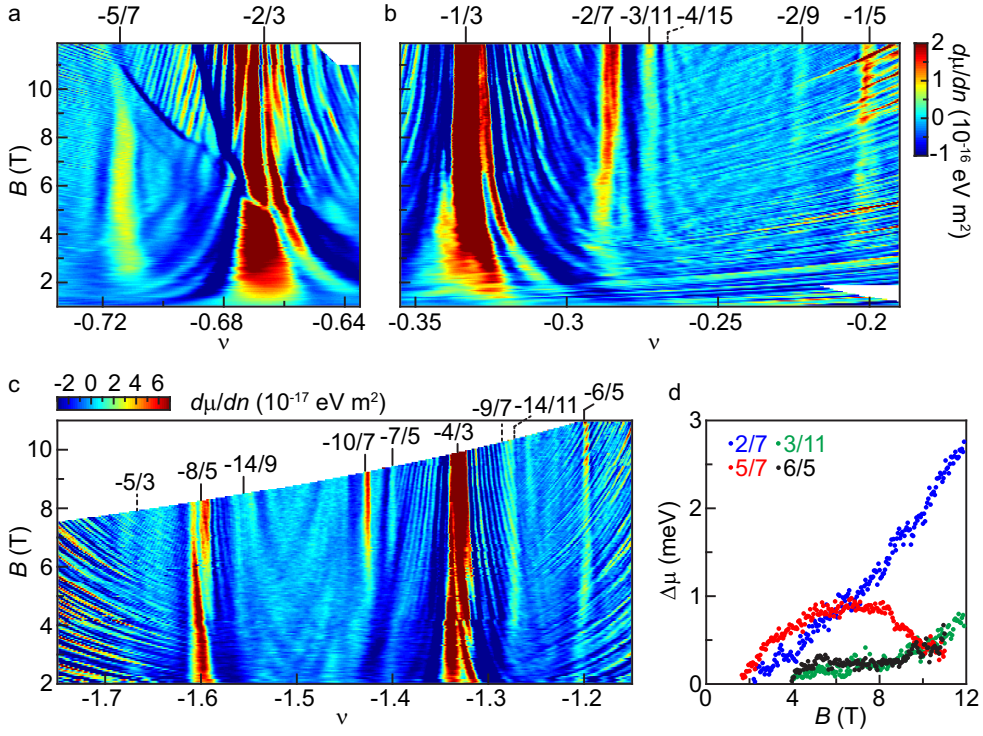

Figure 5.4: (a)-(c) $d\mu/dn$ as a function of ν and B. Prominent four-flux FQH states are labeled. (d) $\Delta\mu_\nu$ of the ^{4}CF states as a function of B.

of disorder at different filling factors, or by competition with other quantum Hall states, particularly near $\nu = -2$.

The extracted steps in chemical potential for several ^{4}CF FQH states are plotted as a function of magnetic field in Fig. 5.4d. The fluctuations caused by localized states near $\nu = -1/5$ and $-2/9$ prevent an accurate determination of $\Delta\mu_\nu$ for these states, but all other states except for $\nu = -5/7$ scale approximately linearly with magnetic field. Further study is required to determine whether the non-monotonic behavior of $\Delta\mu_{-5/7}$ reflects a phase transition or whether the state is simply competing with $\nu = -2/3$. Regardless, the appearance of ^{4}CF states and phase transitions represents an important advance in sample quality that enables further study of and control over the delicate many-body states arising from interacting Dirac fermions in graphene.

Acknowledgments

We would like to thank M. T. Allen for help with current annealing. We also acknowledge useful discussions with M. Kharitonov, J. K. Jain, L. S. Levitov and S. H. Simon. This work is supported by the US Department of Energy, Office of Basic Energy Sciences, Division of Materials Sciences and Engineering under Award #DE-SC0001819. JHS and BK acknowledge financial support from the DFG graphene priority programme. BK acknowledges financial support from the Bayer Science and Education Foundation. This work was performed in part at the Center for Nanoscale Systems at Harvard University, a member of the National Nanotechnology Infrastructure Network, which is supported by the National Science Foundation under award no. ECS-0335765.

5.6 Methods

Both tip and sample were the same as those used in Chapter 4. The data presented in this paper was taken after one more current annealing step with a source-drain bias $V_{sd} = 1.56$ V. All the local measurements reported in the main text were conducted on the monolayer side of the flake, approximately 300 nm from the monolayer-bilayer interface and 500 nm from the electrical contacts.

5.7 Supplementary Discussion

5.7.1 Detailed explanation of model and simulation

Below, we describe in detail the method used to numerically simulate the inverse compressibility shown in Fig. 5.2. The simulation is based on a model of composite fermion Landau level (CF LL) energies $E^{\pm}_{N^*}$, where N^* is the CF orbital index and $\pm$ corresponds to spin-down (up) states. $E^{\pm}_{N^*}$ contains two terms, the first of which is an effective kinetic

energy arising from Coulomb interactions

$$E_{N^*} = (N^* - \frac{1}{2})\hbar\omega_c^*. \tag{5.1}$$

In the above expression, $\omega_c^* = eB^*/m^*$ is the CF cyclotron frequency, $B^* = |B - 2n\Phi_0|$ is the reduced magnetic field felt by CFs, e is the absolute value of the electron charge, n is the carrier density, B is the magnetic field (in Tesla), $\Phi_0 = h/e$ is the flux quantum, and $h = 2\pi\hbar$ is Planck's constant. Because the fractional quantum Hall effect (FQHE) is driven by electron-electron interactions, we assume that the CF effective mass $m^* \propto \sqrt{n}$. Furthermore, we can define filling factor $\nu = nh/eB$, which implies that $B^* = |1 - 2\nu|$ and $m^* \propto \sqrt{\nu B}$ (this expression for mass is similar to that proposed by Park and Jain [138], except for an additional factor of $\sqrt{\nu}$, which is a small factor of order unity and does not dramatically change the qualitative simulated behavior). Substituting these results into Eq. 5.1 and using the $\nu = p/(2p-1)$ branch (we use this throughout the derivation because that is what is shown in Fig. 5.2):

$$E_{N^*} = \alpha(N^* - \frac{1}{2})(2\nu - 1)\sqrt{B/\nu}. \tag{5.2}$$

Both panels in Fig. 5.2 were generated using fit parameter $\alpha = 1.03 \times 10^{-22}$ J/T$^{1/2}$, which we determine by matching the phase transitions in our model to the experimental data.

The second term in our model is an energy splitting that scales linearly with magnetic field $E^{\pm} = \pm\beta B$. In the simplest case, this splitting can arise from the Zeeman effect; then $\beta = 0.5g\mu_B$, where $g \approx 2$ is the g factor of electrons in graphene and μ_B is the Bohr magneton. For concreteness, we consider this case below. However, our model applies equally well to any form of spin and/or valley energy splitting that scales linearly with magnetic field. The final expression for the energy of CF LLs therefore reads

$$E_{N^*}^{\pm} = E_{N^*} + E^{\pm} = \alpha(N^* - \frac{1}{2})(2\nu - 1)\sqrt{\frac{B}{\nu}} \pm \frac{1}{2}g\mu_B B. \tag{5.3}$$

If we assume that there is no disorder and define ν^* as the CF filling factor (identical to p, except that ν^* can take on non-integer values), then we can write the following relation:

$$\nu^* = \int_{-\infty}^{\mu} \sum_{N^*,\pm} \delta(\mu' - E^{\pm}_{N^*}) d\mu' \tag{5.4}$$

However, in real samples, disorder is always present. We therefore modify Eq. 5.4 to include finite smearing of the CF LLs:

$$\nu^* = \sum_{N^*,\pm} [\frac{1}{\pi} \arctan(\frac{\mu - E^{\pm}_{N^*}}{\Delta}) + \frac{1}{2}] = \frac{\nu}{2\nu - 1}. \tag{5.5}$$

In the above expression, we have introduced Lorentzian disorder broadening. This represents an arbitrary choice among several possible functional forms that can be used to account for disorder, but using other types of smearing does not alter the qualitative expectations from the model. In Eq. 5.5, the parameter Δ can be thought of as the width of the CF LL that arises from disorder, and if we assume a constant density inhomogeneity δn in the sample, Δ is a function of ν. We can relate Δ to δn by taking derivatives of Eq. 5.3 as well as the expressions $\nu^* = \nu/(2\nu - 1)$ and $\nu = nh/eB$, yielding:

$$\Delta = \frac{dE^{\pm}_{N^*}}{dN^*} \delta\nu^* = [\alpha(2\nu - 1)\sqrt{B/\nu}][\frac{(\delta n)h}{eB(2\nu - 1)^2}] = \frac{(\delta n)\alpha h}{e\sqrt{B\nu}(2\nu - 1)}. \tag{5.6}$$

We use $\delta n = 3 \times 10^7$ and 1.5×10^8 cm^{-2} to produce Figs. 5.2b,c, respectively.

In Eq. 5.5, the last equality follows from the relation between electron filling factor and the number of occupied CF LLs. Given the expression for $E^{\pm}_{N^*}$ from Eq. 5.3, we can numerically solve Eq. 5.5 for μ as a function of ν, and use simple algebra to recover $d\mu/dn$. Strictly speaking, the quantity μ in Eqs. 5.4 and 5.5 is the chemical potential for a CF, that is the energy to add an electron plus two quanta of the fictitious (Chern-Simons) magnetic field. We expect that this will differ from the chemical potential to add an electron by at most a factor of order unity, and within the level of approximation incorporated in our model of non-interacting CFs, we neglect the difference between these quantities.

We observe only one phase transition in the data at each filling factor, which we believe corresponds to the highest-field one. This likely reflects the level of disorder in the sample, and is consistent with our theoretical model (Fig. 5.2c). The model predicts that further improvements in cleanliness would allow us to observe multiple phase transitions in a given filling factor over the available experimental range (Fig. 5.2b). We note that there are already some low-field oscillations in compressibility (*e.g.* in Fig. 5.1e, starting from $B = 7$ T, just to the right of $p = 5$) that are reminiscent of the diamond-shaped compressibility modulations between incompressible peaks in Fig. 5.2; this behavior may be a precursor to the more delicate low-field features.

5.7.2 Measurements at additional locations

Although all the data presented in the main text were taken at a single location, the qualitative behavior and phase transitions that we observe are independent of position. Figure 5.5 shows inverse compressibility as a function of filling factor and magnetic field at two additional positions that are 300 and 600 nm, respectively, further from the monolayer-bilayer interface than the original measurement position. The phase transitions occur at slightly different critical fields at each location, but the qualitative behavior is unchanged: they are still marked by sharply negative compressibility that cuts across the FQH state, and the critical field increases with filling factor denominator. We emphasize that due to the local nature of the measurement technique, moving the tip to different locations on the flake allows us to effectively probe multiple independent samples.

The variation in the critical fields of the phase transitions suggests that the stability of the FQH states is influenced by the details of the disorder at each location. This is further supported by measurements taken prior to the final current annealing step, when the sample had significantly more disorder. These measurements revealed a $\nu = 2/3$ phase

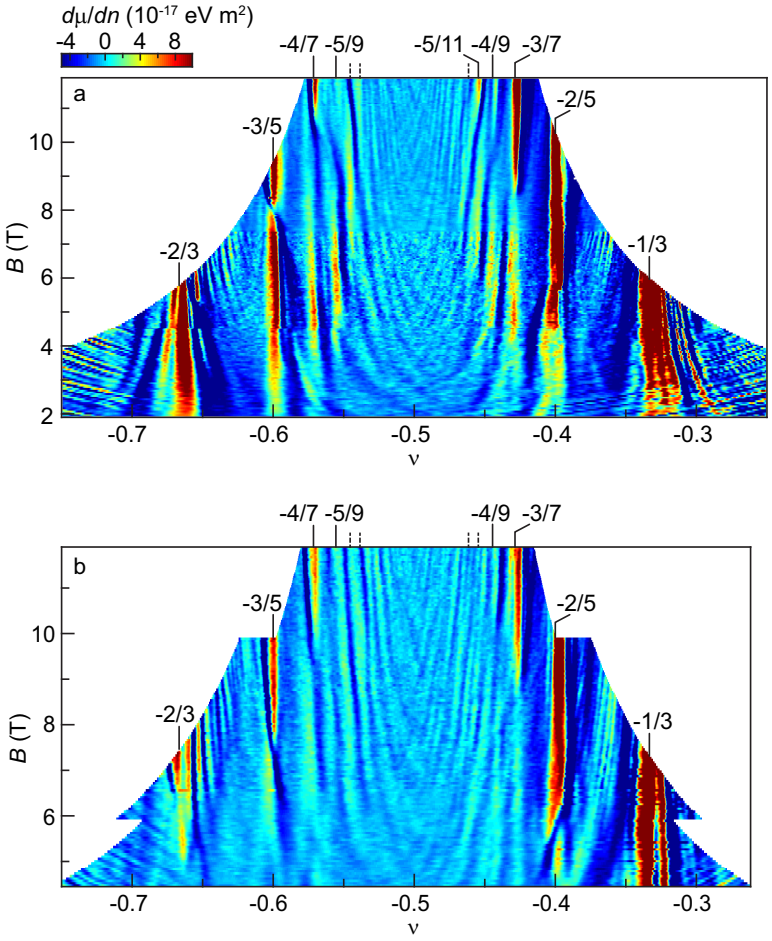

Figure 5.5: (a) and (b) Inverse compressibility $d\mu/dn$ as a function of filling factor ν and magnetic field B. The measurements were performed at two additional positions 300 nm (a) and 600 nm (b) from those presented in the main text, but the qualitative behavior is similar. Principal FQH states are labeled and marked with black lines.

transition around $B = 3.5$ T at multiple locations (Fig. 5.6); the large change in critical field likely reflects the large discrepancy in disorder.

5.7.3 Localized states and compressibility oscillations near $\nu = -1/2$

As stated in the main text, localized states are clearly visible near the strongest FQH states (Fig. 5.1a). Localized states are easy to identify because they run parallel to their parent QH state in the n-B plane [13], and therefore appear as curved compressibility oscillations in the ν-B plane. Although the modulations in compressibility near $\nu = -1/2$ also curve in the ν-B plane, their origin is distinct. For FQH states with high denominators (*i.e.* between $\nu = -4/7$ and $-5/11$), no localized states are visible (Fig. 5.1c). This is likely because the small quasiparticle charge associated with these states enables efficient screening of the underlying disorder potential as quasiparticles are added to the system. Due to the absence of localized states associated with high-denominator FQH states, and because the oscillations in compressibility near $\nu = -1/2$ do not match the slope of low-denominator FQH states in the n-B plane, we conclude that these oscillations are not caused by localized states.

Moreover, localized states, as their name suggests, are confined to a particular region in space. They are visible when a small area being sensed by the SET does not have the same carrier density as the bulk of the sensed area. Because the localized states are spatially isolated, little crosstalk is expected with other regions, and their strengths should not be affected when they intersect a FQH state at a different spatial location.

5.7.4 Zoom-ins on phase transitions

Finer measurements of various phase transitions are depicted in Fig. 5.7. The pattern of localized states changes above and below several of the phase transitions, indicating that

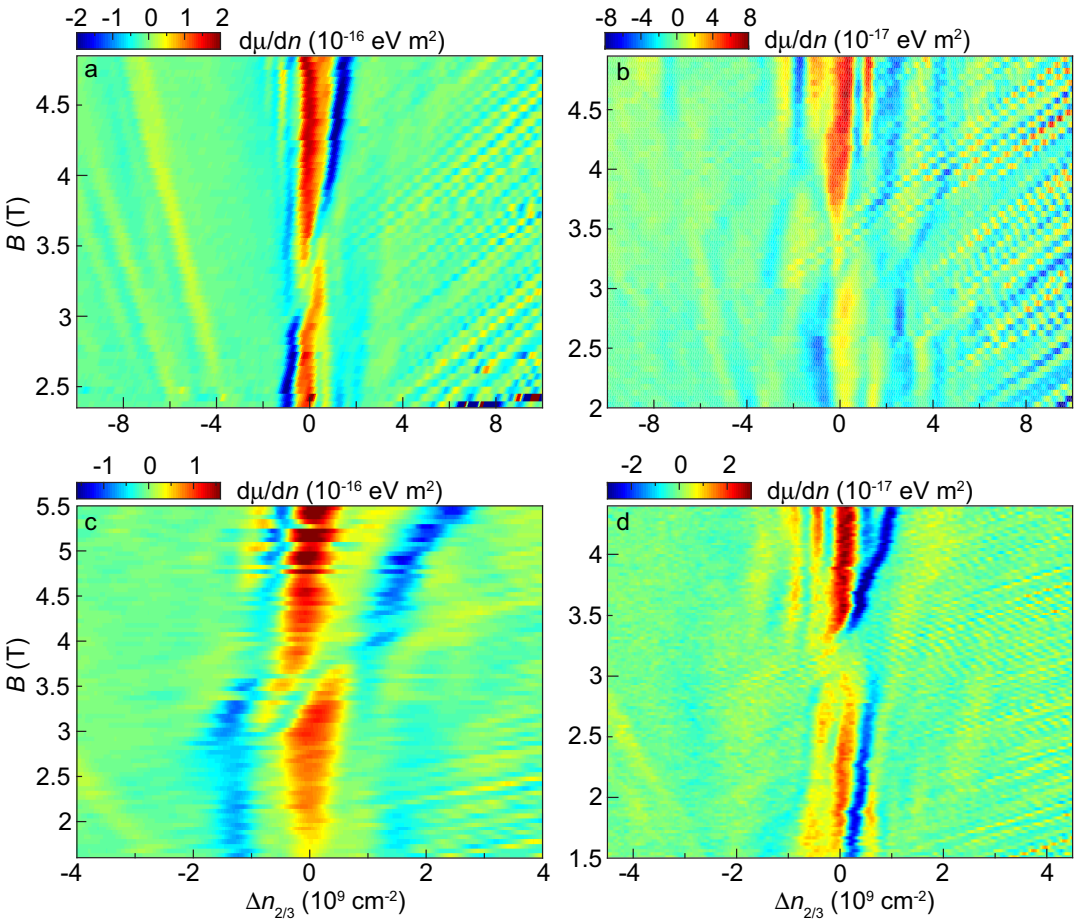

Figure 5.6: (a)-(d) $d\mu/dn$ as a function of the carrier density offset from $\nu = 2/3$ ($\Delta n_{2/3}$) and magnetic field, taken at different locations. The $\nu = 2/3$ incompressible peak splits into a doublet and weakens considerably between 3 and 3.5 T, but then strengthens again at lower field, indicating a phase transition. The measurement positions in panels (a)-(c) were all separated by at least 300 nm, and the region probed in panel (d) is near that in (a).

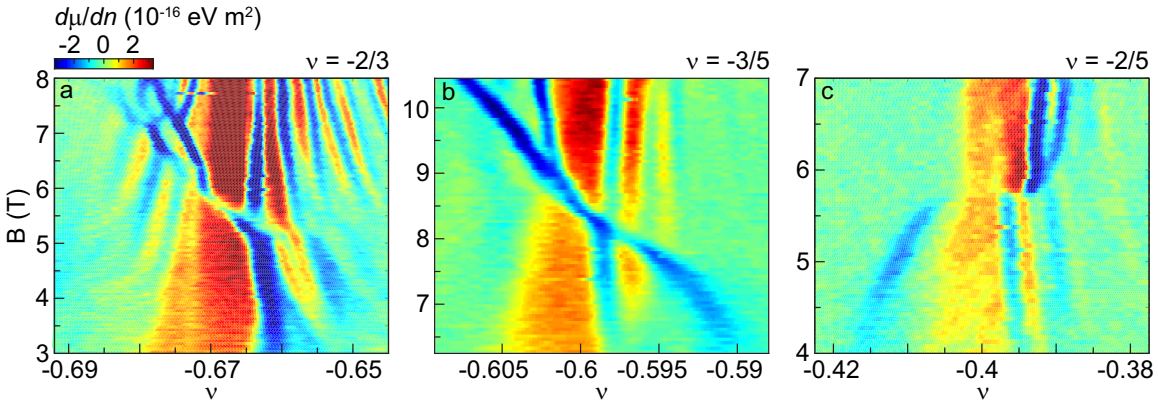

Figure 5.7: (a)-(c) Finer measurements of $d\mu/dn$ as a function of ν and B, zoomed in on the phase transitions at $\nu = -2/3, -3/5$ and $-2/5$, respectively.

the screening changes, as was observed in GaAs [126]. In some cases, multiple narrow curved negative compressibility features are visible (Figs. 5.7a,b and 5.4a); this behavior cannot be explained by localized states, and its origin remains unclear. For $\nu = -2/5$, the phase transition appears to occur virtually instantaneously in magnetic field at the two measurement locations (Figs. 5.5a and 5.7c). However, in the third measurement position, the phase transition reverts back to the more typical behavior observed at other filling factors (Fig. 5.5b). The differences in behavior may be related to the level of disorder at each location; further study is required to fully understand the origin of this behavior.

5.7.5 Carrier density at large back gate voltage

At large back gate voltage V_{bg}, the incompressible peaks of the FQH states curve slightly in the V_{bg}-B plane. This likely reflects a small change in the capacitance between the back gate and the sample that occurs because the graphene sags slightly at large back gate voltages. To account for this effect, we use the relationship $n = \frac{C_g}{e}[1 + \gamma(V_{bg})^2]V_{bg}$, where $C_g/e = 3.02 \times 10^{14}$ m^{-2} is proportional to the gate capacitance without any flake sagging and $\gamma = 1.67 \times 10^{-4}$ is an empirical factor that accounts for the deflection of the sample as

the gate voltage is increased (it corresponds to about 3 nm of sagging at $V_{bg} = 10$ V). This correction is used for all figures in the paper, but the impact is only significant for Fig. 5.4c. The procedure does, however, contribute some uncertainty in the filling factor, particularly at large filling factors ($|\nu| > 1$) and high magnetic field.

Chapter 6

Electron-Hole Asymmetric Fractional Quantum Hall Effect in Bilayer Graphene

The nature of fractional quantum Hall (FQH) states is determined by the interplay between the Coulomb interaction and the symmetries of the system. The unique combination of spin, valley, and orbital degeneracies in bilayer graphene is predicted to produce novel and tunable FQH ground states [55, 102, 106, 134, 135, 140, 141]. Here we present local electronic compressibility measurements of the FQH effect in the lowest Landau level (LL) of bilayer graphene. We observe incompressible FQH states at filling factors $\nu = -10/3, -4/3, 2/3,$ and $8/3$, with hints of additional states appearing at $\nu = -17/5, -7/5, 3/5$ and $13/5$. This sequence of states breaks particle-hole symmetry and instead obeys a $\nu \rightarrow \nu + 2$ symmetry, which highlights the importance of the orbital degeneracy for many-body states in bilayer graphene.

6.1 Introduction

The charge carriers in bilayer graphene obey an electron-hole symmetric dispersion at zero magnetic field. Application of a perpendicular magnetic field B breaks this dispersion into energy bands known as LLs. In addition to the standard spin and valley degeneracy found in monolayer graphene, the $N = 0$ and $N = 1$ orbital states in bilayer graphene are also degenerate and occur at zero energy [7]. This results in a sequence of single-particle quantum Hall states at $\nu = \pm 4(M + 1)e^2/h$, where M is a non-negative integer [16].

When the disorder is sufficiently low, the eightfold degeneracy of the lowest LL is lifted by electron-electron interactions, which results in quantum Hall states at all integer filling factors [72, 73]. The nature of these broken-symmetry states has been studied extensively both experimentally and theoretically, with particular attention given to the insulating $\nu = 0$ state. The filling sequence was initially predicted to first maximize spin polarization, then valley ordering, and finally orbital polarization [17]. It has been shown, however, that the ground state at $\nu = 0$ in bilayer graphene in certain samples is actually a canted antiferromagnet, which maximizes neither spin nor valley polarization [44, 48]. Multiple groups have also been able to induce transitions between different spin and valley orders of the ground states using external electric and magnetic fields [48, 90–92]. It is clear that the interplay between Zeeman energy, layer asymmetry, valley anisotropy terms, and SU(4)-symmetric electron-electron interactions produces a rich phase diagram in bilayer graphene not found in any other system.

Knowledge of the ground state at integer filling factors is especially important for investigating the physics of partially filled LLs, where in exceptionally clean samples, the charge carriers condense into FQH states. The above-mentioned degrees of freedom as well as the strong screening of the Coulomb interaction in bilayer graphene are expected to result

in an interesting sequence of FQH states in the lowest LL [55, 102, 106, 134, 135, 140, 141]. Indeed, partial breaking of the SU(4) symmetry in monolayer graphene has already resulted in sequences of FQH states with multiple missing fractions [53, 110, 111, 136, 137]. Phase transitions between FQH states with different polarizations have also been observed in monolayer graphene [142].

Experimental observation of FQH states, however, has proven to be difficult in bilayer graphene. Hints of a $\nu = 1/3$ state were first reported in transport by Bao *et al.* [74]. Very recently, Ki *et al.* observed robust FQH states at $\nu = -1/2$ and $\nu = -4/3$ in a current-annealed suspended bilayer sample [143]. Here, we report local compressibility measurements of a bilayer graphene device fabricated on hexagonal boron nitride (h-BN), performed using a scanning single-electron transistor (SET). Our technique allows us to directly probe the thermodynamic properties of the bulk of the sample [77,78]. We measure the local chemical potential μ and the local inverse compressibility $d\mu/dn$ by changing the carrier density n with a proximal graphite gate located 7.5 nm from the graphene and monitoring the resulting change in SET current. An optical image of the contacted device is shown in Fig. 6.1a.

6.2 FQH states in Bilayer Graphene

Figure 6.1b shows a measurement of the inverse compressibility as a function of filling factor at $B = 2$ T. Incompressible features are present at all nonzero multiples of $\nu = 4$, indicating that we are measuring bilayer graphene. The full width at half maximum of the $\nu = 4$ peak provides a measure of the disorder in the system and is on the order of 10^{10} cm^{-2}, similar to that observed in suspended bilayers [72, 144]. Broken-symmetry states at $\nu = 0$ and ± 2 are also visible at $B = 2$ T, which further indicates the cleanliness

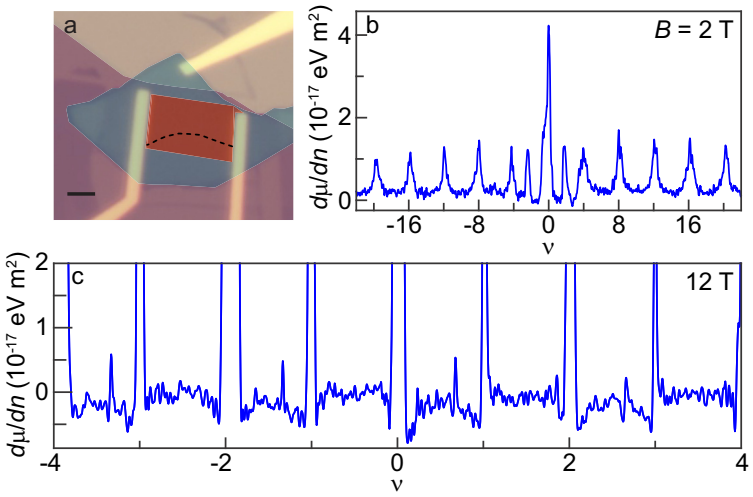

Figure 6.1: (a) Optical image of the device with colored overlays showing the graphite (blue), boron nitride (purple), and monolayer-bilayer graphene hybrid (red). The black dashed line marks the interface between monolayer and bilayer. The scale bar is 2 μm. (b) and (c) Inverse compressibility $d\mu/dn$ as a function of filling factor ν at magnetic field $B = 2$ T and 12 T, respectively.

of the sample. Most interesting, however, is the appearance of additional incompressible peaks at $B = 12$ T, shown in Fig. 6.1c. At this field, all of the broken-symmetry states between $\nu = \pm 4$ have fully developed. In addition, we observe incompressible features at $\nu = -10/3, -4/3, 2/3$, and $8/3$, suggesting the presence of FQH states.

To confirm the origin of the incompressible peaks, we measure the inverse compressibility as a function of filling factor and magnetic field. Figures 6.2a,b show the behavior for $-4 < \nu < 0$ and $0 < \nu < 4$, respectively. Quantum Hall states appear as vertical features when plotted in this form, while localized states, which occur at a constant density offset from their parent states, curve as the magnetic field is changed [13, 137]. We can then unambiguously identify the features at $\nu = -10/3, -4/3, 2/3$, and $8/3$ as FQH states. The FQH states closer to the charge neutrality point are more incompressible than those at higher filling factors, and they persist to fairly low magnetic fields, with the last

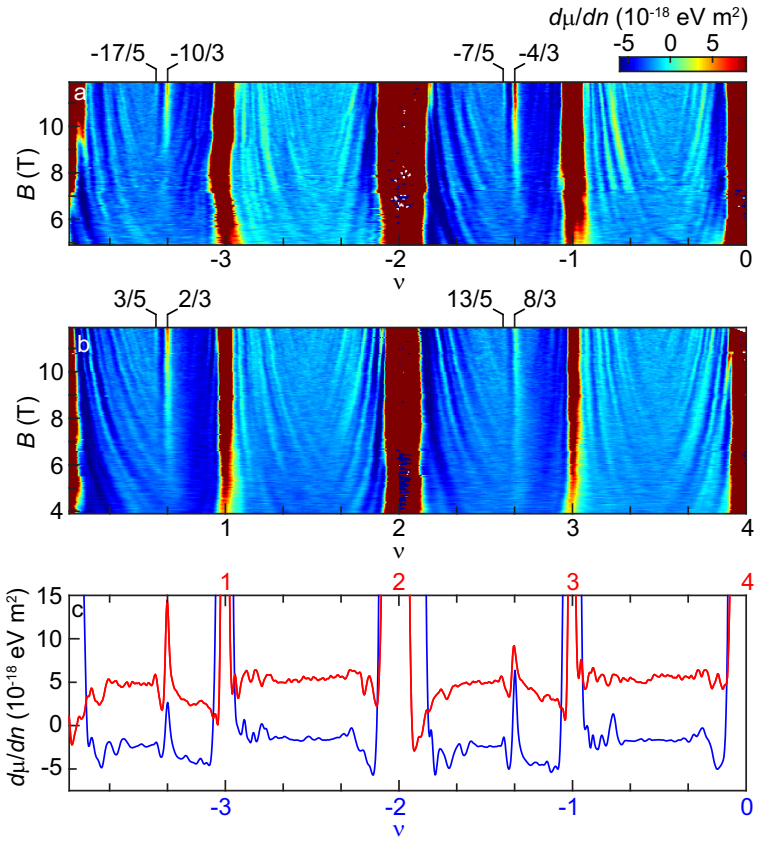

Figure 6.2: (a) and (b) Inverse compressibility as a function of filling factor and magnetic field. The color scales are the same in both panels. (c) Average inverse compressibility between $B = 9.9$ and 11.9 T as a function of filling factor. The red curve (electron side) is offset by 7×10^{-18} eV m^2 for clarity.

hints disappearing around 6 T. At $B > 10$ T, we also see evidence of developing states at $\nu = -17/5, -7/5, 3/5$, and $13/5$.

Averaging the inverse compressibility over a range of magnetic fields reduces the fluctuations created by localized states and clarifies the underlying behavior. Figure 6.2c shows the average inverse compressibility from $B = 9.9$ to 11.9 T, which clearly shows the FQH states identified above. Figure 6.2c also reveals that the background inverse compressibility is markedly lower between the integer filling factors where we observe the FQH states. This correlation is consistent with previous experiments where a negative background com-

pressibility was attributed to Coulomb interactions between charge carriers [57]. We also note that the background inverse compressibility in higher LLs, where no FQH states were observed, was much higher than in the lowest LL (see Section 6.6).

6.3 Electron-Hole Asymmetric Sequence of States

Interestingly, the sequence of FQH states that we observe does not obey particle-hole symmetry but rather seems to follow a $\nu \rightarrow \nu + 2$ symmetry. This indicates that the orbital degeneracy uniquely present in bilayer graphene is playing an important role in determining the sequence of observed fractions. Recent theoretical work on the FQH effect in the lowest LL has predicted the presence of FQH states with a $\nu \rightarrow \nu + 2$ symmetry in bilayer graphene based on a model that incorporates the strong screening and LL mixing present in the lowest LL of bilayer graphene [55]. We do not see any fractions between $\nu = -3$ and -2, nor between $\nu = 1$ and 2, nor their $\nu + 2$ symmetric counterparts. At these filling factors, one might expect to have a filled $N = 0$ LL and be partially filling an $N = 1$ LL. The absence of states in these ranges suggests a difference between partial filling when both the $N = 0$ and $N = 1$ LLs are empty and partial filling of the $N = 1$ LL when the $N = 0$ LL is full. The increased LL mixing present when the $N = 0$ LL is full [145] may be weakening the strength of FQH states in the $N = 1$ LL.

Our observed FQH sequence also suggests possible orbital polarization of the FQH states. The FQH states we observe at $\nu = 2p + 2/3$, where $p = -1, 0$, or 1, could be singlet states of $N = 0$ and $N = 1$ orbitals, or could arise from a 2/3 state with full orbital polarization. The next strongest FQH states we observe occur at $\nu = 2p + 3/5$, which must have some nonzero orbital polarization. It is worthwhile to note that the strongest

FQH states at multiples of $\nu = 1/5$ do not have even numerators, in contrast with recent theoretical predictions [55].

The strongest FQH states that we observe are different from those seen in previous experiments on bilayer graphene, which may point to different patterns of symmetry-breaking in the different systems. Ki *et al.* observed FQH states at $\nu = -4/3$, and $-1/2$, with hints of an additional feature at $\nu = -8/5$ [143]; the only FQH state that we also observe is $\nu = -4/3$. It is also possible that the effective interactions present in the two samples may be different due to differences in screening between a suspended bilayer and a bilayer on a substrate. The fact that different sample preparations result in different FQH states is a sign of the theoretically predicted tunability of the FQH effect in bilayer graphene [106,134,140]. Beyond the changes in polarization observed in monolayers, it appears possible to experimentally tune the relative strengths of various incompressible FQH states in bilayer graphene. Future experiments in which a perpendicular electric field and/or a parallel magnetic field are applied to the sample will provide insight into the conditions under which different FQH states are favored.

6.4 Steps in Chemical Potential of FQH States

We can integrate the inverse compressibility as a function of density to obtain the energy cost of adding an electron to the system, as discussed in ref. [137]. This quantity must be divided by the quasiparticle charge associated with each state to determine the corresponding energy gap Δ_ν. The most likely quasiparticle charge for states at multiples of $\nu = 1/3$ is $e/3$, but the nature of the FQH states in bilayer graphene is not yet fully understood, so we plot the extracted steps in chemical potential $\Delta\mu_\nu$ in Fig. 6.3a. For $\nu = -4/3$ and $\nu = 2/3$, $\Delta\mu_\nu$ is about 0.75 and 0.6 meV, respectively, at $B = 12$ T.

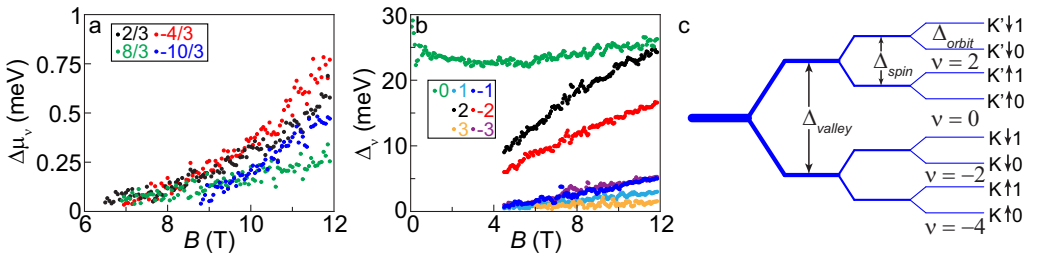

Figure 6.3: (a) Steps in chemical potential of the fractional quantum Hall (FQH) states as a function of magnetic field. (b) Energy gaps of the integer broken-symmetry states in the lowest Landau level (LL). (c) Schematic diagram showing the order of symmetry breaking in the sample.

Assuming a quasiparticle charge of $e/3$, the energy gap we find at $\nu = -4/3$ is comparable with, if somewhat larger than, that found in ref. [143] at similar magnetic fields. The gaps of FQH states farther away from charge neutrality are smaller; $\Delta\mu_{-10/3}$ and $\Delta\mu_{8/3}$ are only about 0.5 and 0.3 meV at $B = 12$ T. All of the extracted gaps appear to scale approximately linearly with B. Previous measurements of broken-symmetry integer states in suspended bilayers also found a linear-B dependence of the gaps, which was attributed to LL mixing [22, 144].

The energy gaps of the integer filling factors $|\nu| < 4$ are shown in Fig. 6.3b. All of the gaps increase with B, except for $\nu = 0$, which is fairly constant around 23-25 meV over almost the full range in magnetic field. The size of the gap and its persistence to zero field lead us to conclude that the ground state at $\nu = 0$ is layer-polarized. If we assume that the $\nu \to \nu + 2$ symmetry arises from the orbital degree of freedom, we can fully determine the sequence of symmetry-breaking in the sample: valley polarization is first maximized, then spin polarization, and finally orbital polarization, as illustrated in Fig. 6.3c. The large valley polarization in our sample relative to other bilayer devices may be caused by interactions with the substrate. A large band gap has been observed in a monolayer graphene sample on h-BN with a proximal graphite gate, which was attributed to the breaking of sublattice

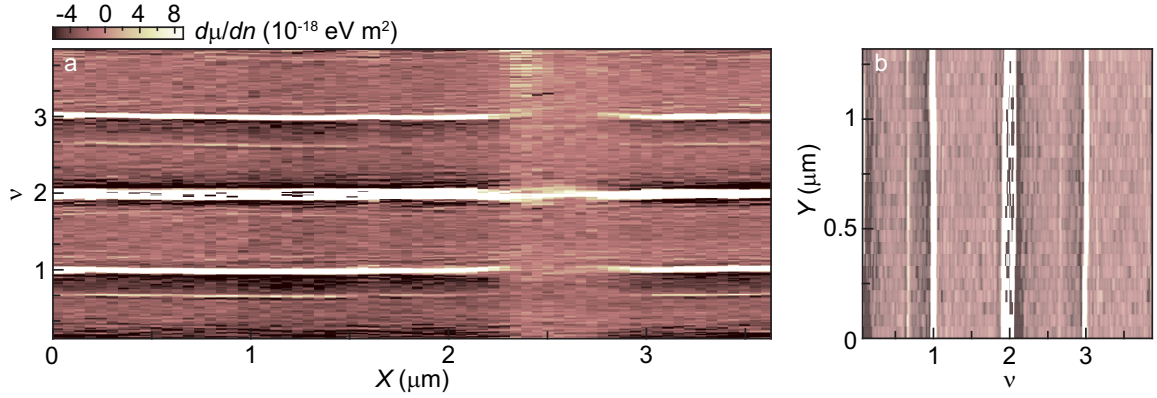

Figure 6.4: Inverse compressibility as a function of filling factor and position X (a) and Y (b). The sequence of FQH states does not vary with position.

symmetry by h-BN [146]. It is also possible that the difference in distance between the top layer to the graphite gate and the bottom layer to the graphite gate is creating a potential difference in the two layers [9], or that the different environments experienced by each layer play a role. Even if the $\nu = 0$ gap is caused by single-particle effects, its constancy over the entire field range is somewhat surprising because both the potential difference between the layers and the Coulomb energy are expected to contribute to the gap [147].

All of the measurements described above were performed at a single location on the sample. Local measurement allows us to find the cleanest regions and study the properties of FQH states in those areas. In addition, the local nature of our probe allows us to, in effect, measure multiple independent samples by measuring at different locations. Figure 6.4 shows linescans of inverse compressibility as a function of filling factor and position. The net level of doping remains fairly constant over the entire range of the spatial scans, but there are fluctuations in the strengths of the broken-symmetry and FQH states, likely due to differences in the amount of local disorder. Despite these fluctuations, the overarching pattern of FQH states is consistent across the entire sample, and also did not change with current annealing (see Section 6.6). The electron-hole asymmetric sequence of FQH states

can therefore be attributed to the intrinsic properties of bilayer graphene, rather than disorder. The observation of an unconventional sequence of FQH states in bilayer graphene indicates the importance of its underlying symmetries and opens new avenues for exploring the nature and tunability of the FQH effect.

Acknowledgments

We would like to thank D. A. Abanin and B. I. Halperin for useful discussions. We also thank Javier Sanchez-Yamagishi for help with fabrication.

6.5 Methods

Graphite was mechanically exfoliated onto an O_2-plasma-cleaned doped Si wafer capped with 285 nm of SiO_2. Suitable graphite pieces were found using a combination of optical microscopy and atomic force microscopy (AFM). A 7.5-nm-thick piece of hexagonal boron nitride (h-BN) was then transferred onto the graphite using the process detailed in ref. [146]. A hybrid monolayer-bilayer graphene flake was then transferred onto the h-BN using the same method. Contacts were defined to the graphene and graphite using electron-beam lithography before thermal evaporation of Cr/Au (1 nm/85 nm) contacts and liftoff in warm acetone. The sample was cleaned in a mixture of Ar/H_2 at 350 °C before each transfer step and after liftoff. The sample was further cleaned using an AFM tip. Measurements were made in a ^{3}He cryostat at approximately 450 mK. The sample was cleaned in the cryostat using current annealing. The sample measures 8 μm from contact to contact and is 4 μm wide. All measurements presented here were made on the bilayer side of the flake.

The fabrication of the SET tip was performed according to the procedure outlined in Appendix B. Electrical leads were 16 nm thick and the island was approximately 7 nm.

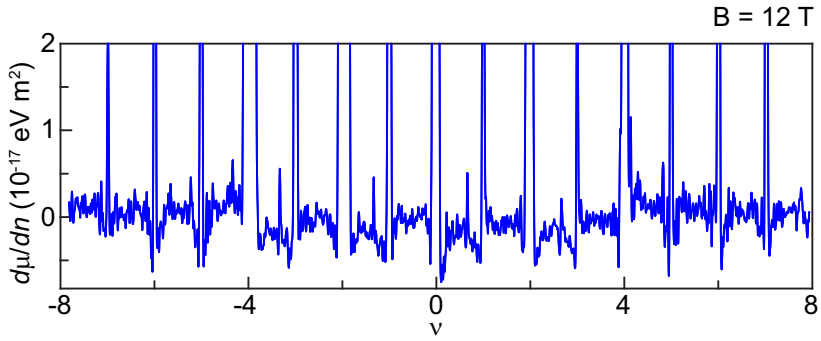

Figure 6.5: Inverse compressibility over a larger range in filling factor showing the lowest LL has more negative background compressibility than higher LLs.

The diameter of the SET was approximately 100 nm, and it was held 50-100 nm above the graphene flake during measurements.

6.6 Supplementary Discussion

6.6.1 Higher Landau levels in bilayer graphene

Figure 6.5 shows the inverse compressibility as a function of filling factor for $-8 < \nu < 8$. Despite theoretical predictions of robust FQH states in the $N = 2$ LL [102, 140] and experimental hints in other samples [48], we do not observe any FQH states between $|\nu| = 4$ and 8. The background inverse compressibility at $4 < |\nu| < 8$ is considerably higher than at $0 < |\nu| < 4$, which is consistent with lower background compressibility corresponding to Coulomb interactions between quasiparticles, as discussed in the main text.

6.6.2 Effects of current annealing

The data presented in the main text were taken after multiple current anneals, with a maximum source-drain voltage $V_{sd} = 10$ V. Figure 6.6 shows the progression of the behavior upon current annealing. Prior to current annealing the sample, we observed all the integer

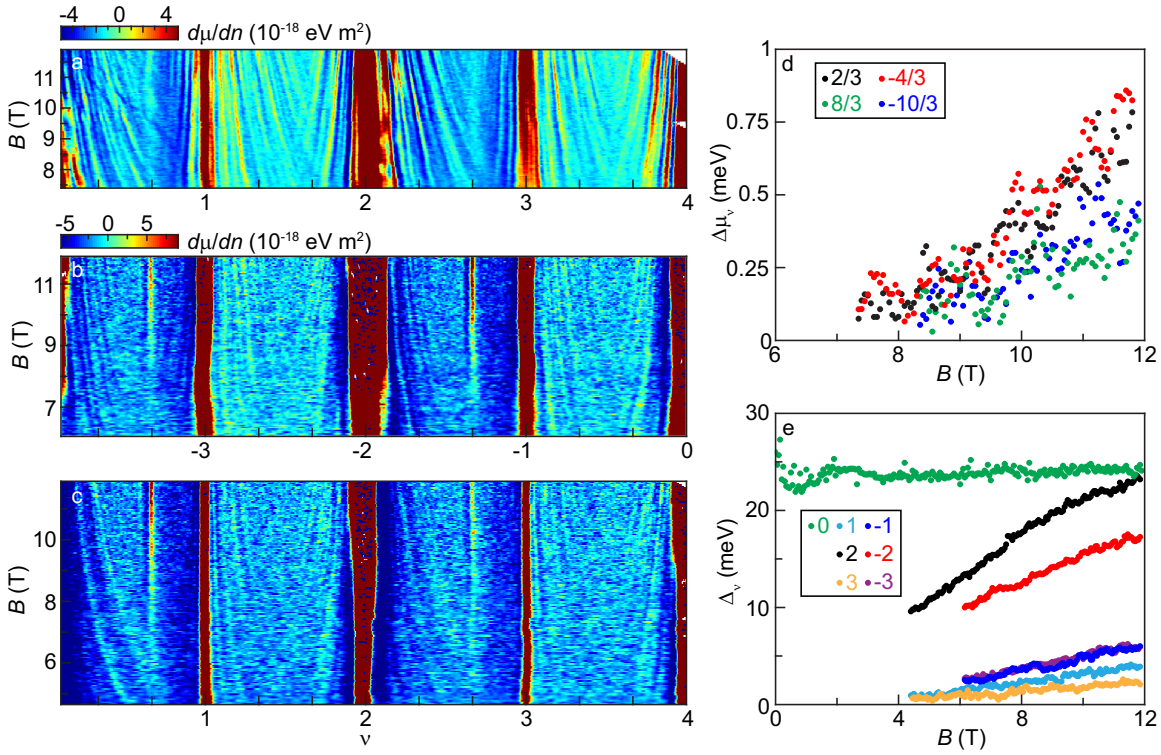

Figure 6.6: (a) Inverse compressibility as a function of filling factor and magnetic field after annealing to a source-drain voltage $V_{sd} = 4$ V. Weak incompressible peaks are visible at $\nu = 2/3$ and $8/3$. (b) and (c) Inverse compressibility as a function of filling factor and magnetic field after annealing to $V_{sd} = 8$ V. The FQH states become sharper and more incompressible, and they persist to lower magnetic field. (d) Steps in chemical potential of the FQH states after annealing to 8 V. (e) Energy gaps of the integer quantum Hall states after annealing to 8 V.

broken-symmetry states between $\nu = \pm 4$, but no FQH states were apparent. After current annealing to 4 V, we observed hints of incompressible states at $\nu = 2/3$ and $8/3$ (Fig. 6.6a). These states became more robust after annealing to 8 V (Figs. 6.6b-e) and additional FQH states appeared at $\nu = -4/3$ and $-10/3$. Throughout all current annealing steps, the sequence of incompressible FQH states did not change; current annealing appears to only increase their strength. It is worthwhile to note that the steps in chemical potential were slightly larger for $\nu = 2/3$ and $8/3$ after annealing to only 8 V than the data presented in Fig. 6.3a.

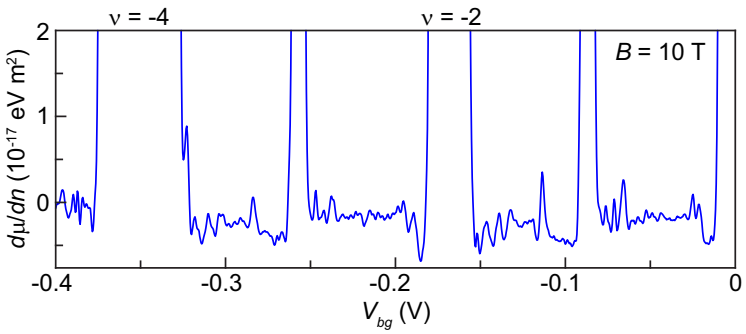

Figure 6.7: Inverse compressibility as a function of back gate voltage V_{bg}. For incompressible states, the quantum capacitance dominates over geometric capacitance, leading to very broad incompressible peaks, particularly at $\nu = -4$ and -2. The spacing between integer quantum Hall states also varies due to differences in background compressibility.

6.6.3 Conversion of gate voltage to filling factor with large geometric capacitance

The proximity of the graphite gate resulted in a large geometric capacitance, C_G, to the sample, causing the total capacitance, C_T, to depend strongly on the compressibility of the sample. Incompressible states dramatically alter C_T because quantum capacitance dominates over geometric capacitance in this regime. Figure 6.7 shows the compressibility as a function of back-gate voltage, V_{bg}, and the very wide integer quantum Hall states clearly demonstrate the filling-factor dependent change in the total capacitance.

In order to assign filling factor, we use the distance between $\nu = 2/3$ and 1 to find C_T in the $\nu = 0$ to 1 range. The equation

$$\frac{1}{C_T} = \frac{1}{C_G} + \frac{1}{e^2}\frac{d\mu}{dn}, \tag{6.1}$$

where $d\mu/dn$ is the average background inverse compressibility between $\nu = 0$ and 1, allows us to determine C_G. The extracted C_G corresponds to a back-gate to density conversion ratio of 2.7×10^{16} cm^{-2}/V, which is reasonable given a h-BN thickness of 7.5-8 nm and a dielectric constant a bit less than 4.

To find C_T in a different filling factor range, we then use Eq. 6.1, the average compressibility in this new filling factor range, and C_G, which we assume is constant. The extracted C_T then provides the conversion between the back-gate voltage and density. Throughout the manuscript, we use the same C_T for $-4 < \nu < -3, 0 < \nu < 1$, and their $\nu \rightarrow \nu + 2$ analogues. We also use a single C_T for filling factors between $\nu = -3$ and -2, $\nu = 1$ and 2, and their $\nu \rightarrow \nu + 2$ counterparts. For $|\nu| > 4$, we use the geometric capacitance.

Chapter 7

Electronic Compressibility at a Monolayer-Bilayer Graphene Interface

Adjoining monolayer and bilayer graphene flakes provide an intriguing system to study because the charge carriers evolve from massless to massive Dirac fermions as they cross the interface. Here we present local electronic compressibility measurements of a monolayer-bilayer hybrid graphene device subject to a perpendicular magnetic field. At the charge neutrality point, both sides of the sample are incompressible due to the formation of broken-symmetry states at filling factor $\nu = 0$, but we observe increased compressibility where they meet. This suggests that the $\nu = 0$ energy gap weakens or closes at the interface, a conclusion further supported by the absence of localized states centered at the monolayer-bilayer boundary. The behavior of several other quantum Hall states also changes as they approach the interface, suggesting that graphene samples with different numbers of layers in adjoining regions may provide an attractive method to locally engineer novel band structures.

7.1 Introduction

Stacking two graphene sheets to form a bilayer dramatically alters the electronic properties of the system. Whereas charge carriers in monolayers have linear dispersion and act as massless Dirac fermions [5], bilayers have parabolic bands at low energy that support massive Dirac fermions [7]. In a perpendicular magnetic field B, the respective Berry's phases of π and 2π in each material lead to single-particle quantum Hall features that are out of phase: in monolayers, states occur at $\nu = \pm 4(M + 1/2)$ [14, 15], whereas bilayers exhibit them at $\nu = \pm 4(M + 1)$ [16], with M a non-negative integer. In addition, the characteristic energy scales of the two systems are very different. Graphene has a much smaller density of states near the charge neutrality point due to its linear dispersion, so the Fermi energy is larger in monolayers for all experimentally relevant carrier densities n.

These striking differences raise the question of how electronic properties evolve near the interface of a monolayer-bilayer hybrid made from one continuous layer that extends throughout the entire sample and a second Bernal-stacked layer that overlaps with only part of the first sheet (Fig. 7.1a). The different energy scales of each side could lead to local charge transfer at the interface. In addition, theoretical studies predict angle-dependent transmission of electrons across the interface at zero magnetic field, with opposite dependence for each valley and corresponding valley polarization of the transmitted wave [148, 149]. In a magnetic field, the Landau levels (LLs) are predicted to disperse as they cross from monolayer to bilayer, leading to regions with flat energy bands near the boundary [121, 149]. This effect occurs within a few magnetic lengths $l_B = \sqrt{\hbar/eB}$ of the boundary, irrespective of the edge termination at the interface, which can take on an armchair or two different zigzag forms. Above, $\hbar$ is Planck's constant divided by 2π and e is the electron charge. Moreover, because the quantum Hall sequences are out of phase, the LLs of a given

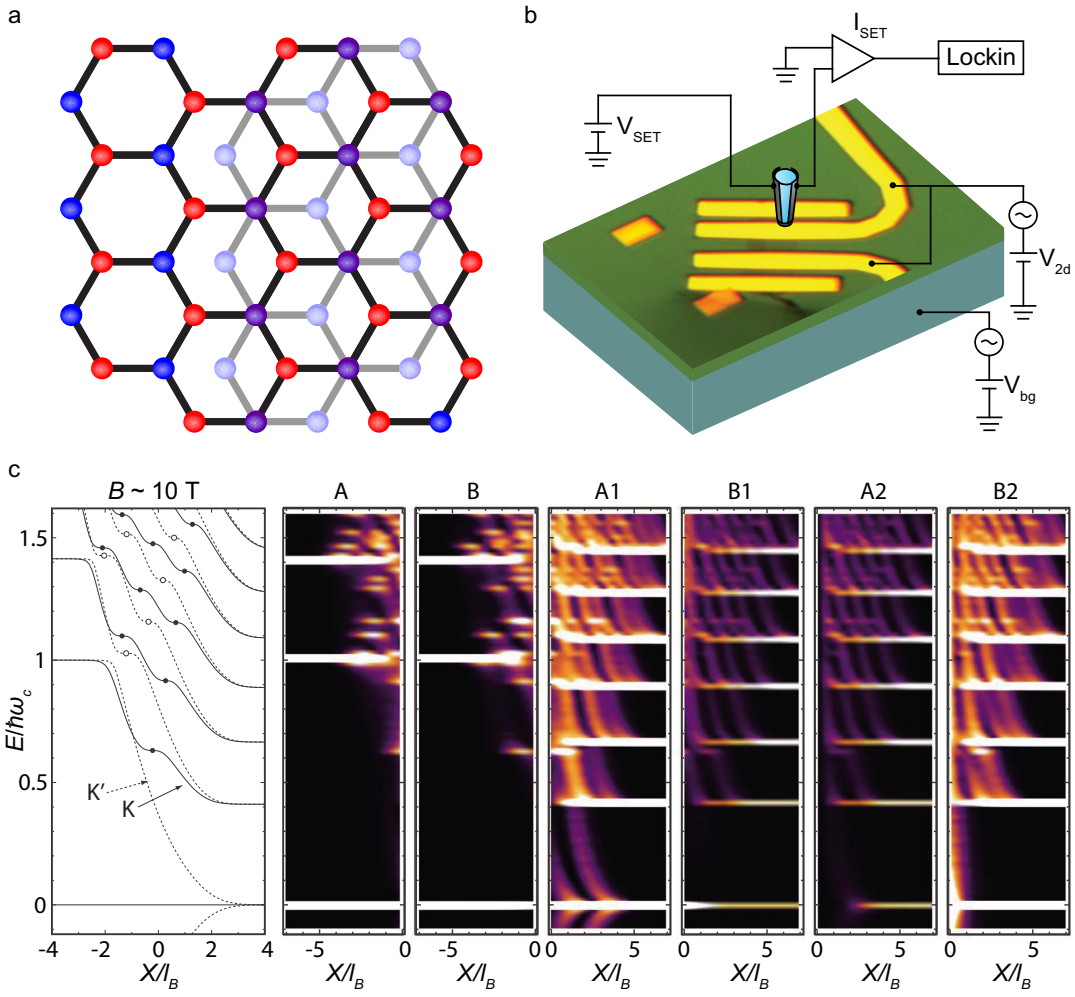

Figure 7.1: (a) Schematic illustration of a monolayer-bilayer hybrid with a zigzag edge termination in which the B2 atoms extend closest to the monolayer region. The bilayer region has Bernal stacking, with A2 atoms directly above B1 atoms in the lower layer. Here, the letter refers to sublattice and the number refers to the layer. (b) Optical image of the measured device, overlaid with a schematic illustration of the measurement setup. The single-electron transistor (SET) is held approximately 50-100 nm about the graphene device and is approximately 100 nm in diameter. (c) Landau level (LL) dispersion near the monolayer-bilayer boundary shown in (a), with negative X corresponding to the monolayer side. The color plots show the density of states (white, high; black, low) as a function of distance to the interface for each sublattice of the monolayer and bilayer sides. Panel (c) reproduced from ref. [121] with minor relabeling of variables.

degenerate orbital quartet in the monolayer split according to their valley degree of freedom and connect to different orbital states in the bilayer (Fig. 7.1c).

Despite the richness of the system, hybrid devices have received little experimental attention. Magnetotransport measurements conducted on a monolayer-bilayer hybrid device showed conductance oscillations consistent with parallel transport through both regions [119]. Quantum oscillations were also strongly modified at certain gate voltages in devices with a narrow monolayer strip at the edge of a large bilayer flake, suggesting that the LLs of the monolayer were influential, even though the bulk of the sample was bilayer graphene [119]. These results suggest that further exploration is warranted, but drawing firm conclusions about the local behavior at the interface from global transport measurements is difficult.

7.2 Changes in Quantum Hall States

To directly explore the electronic properties of a monolayer-bilayer interface, we conducted local electronic compressibility measurements of a suspended hybrid device using a scanning single-electron transistor (SET) [77, 78], schematically illustrated in Fig. 7.1b. The data presented in this chapter were taken on the same sample as was used in Chapters 4 and 5, but we focus here on the compressibility near the interface.

Figure 7.2 shows inverse compressibility as a function of position as the tip is moved from the monolayer to the bilayer side at various magnetic fields. Far from the interface, the expected single-particle quantum Hall sequences occur in each region, with additional incompressible peaks also visible at intermediate integer filling factors due to broken-symmetry states [39,72,73]. Near the interface, however, the behavior qualitatively changes. The strengths of incompressible peaks associated with single-particle quantum Hall states

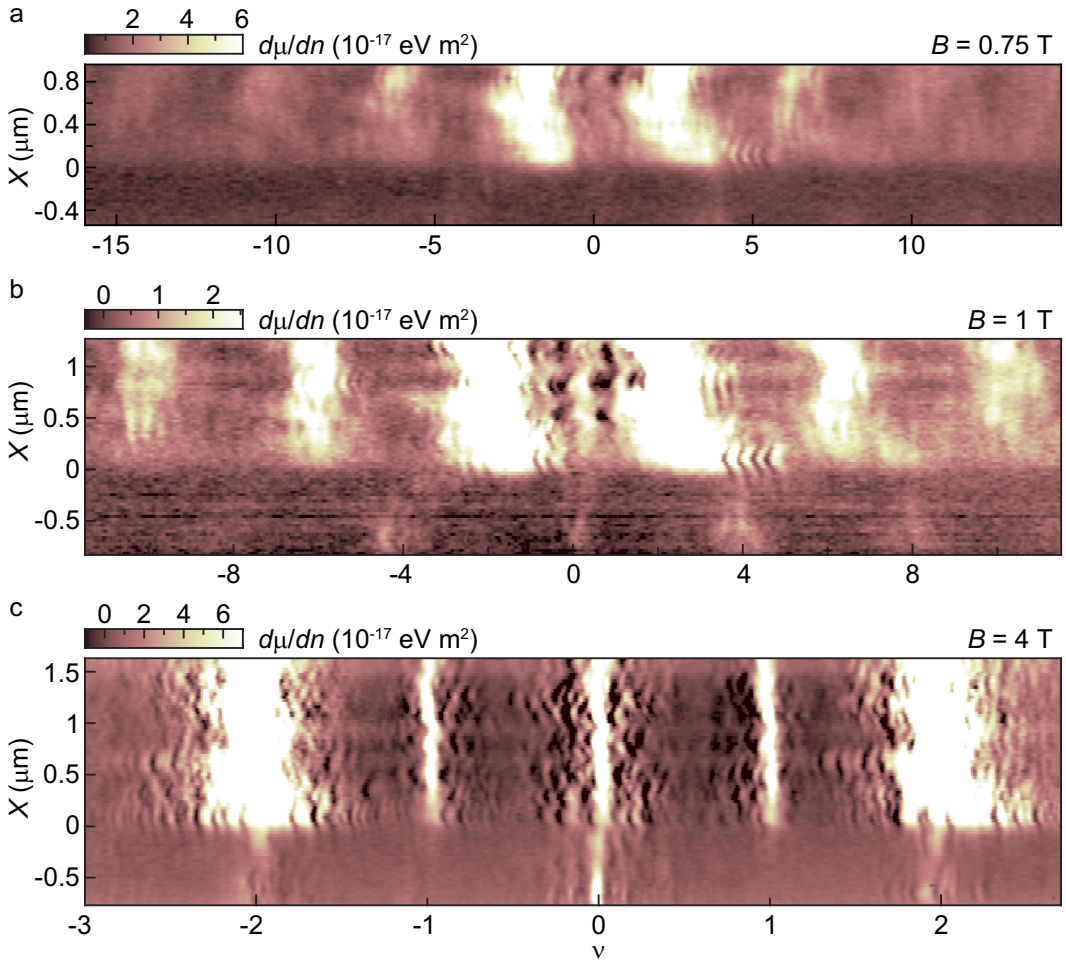

Figure 7.2: (a) Inverse compressibility $d\mu/dn$ as a function of filling factor ν and position X at $B = 0.75$ T (a), 1 T (b), and 4 T (c). Near the interface, the single-particle incompressible quantum Hall states weaken and broaden. The $\nu = 0$ state also weakens where the monolayer and bilayer meet, but the $\nu = \pm 2$ states get stronger and sharper on the bilayer side. In contrast to Fig. 7.1c, positive X corresponds to the monolayer side in this and subsequent experimental figures.

weaken as they approach the interface, whereas the opposite happens in the compressible regions, with additional incompressible behavior developing near the interface over certain ranges in filling factor (Figs. 7.2a,b). The spatial extent of these changes increases as filling factor increases, qualitatively consistent with theoretical predictions [121]. Although the differences in compressibility that we observe extend beyond a few magnetic lengths from the interface, this may be caused in part by the relatively large area sensed by the SET.

Changes to broken-symmetry states also occur near the monolayer-bilayer boundary. The $\nu = \pm 2$ incompressible peaks of the bilayer strengthen and narrow considerably near the interface (Fig. 7.2c). This behavior likely reflects the continuation of only one layer onto the monolayer side of the sample, which locally breaks layer symmetry. The $\nu = \pm 2$ states in bilayer graphene were shown to be stabilized by an electric field that breaks layer symmetry [90], and similar effects are may be at play near the interface.

At the charge neutrality point, the sample becomes more compressible near the interface (Figs. 7.2b,c). Whereas both monolayer and bilayer regions exhibit strong incompressible peaks associated with broken-symmetry $\nu = 0$ states, the boundary between these regions shows a marked increase in compressibility. This behavior is not limited to individual linescans; a similar effect is also visible in a two-dimensional spatial map of the inverse compressiblity at the charge neutrality point (Fig. 7.3). On both the monolayer and the bilayer sides, very incompressible behavior is again apparent. However, near the boundary between the two, the sample is more compressible.

7.3 Absence of Localized States at $\nu = 0$

In addition to the increased compressibility that is evident near the interface at $\nu = 0$, Fig. 7.3 shows that no localized states (visible as dark blue rings) are centered at the

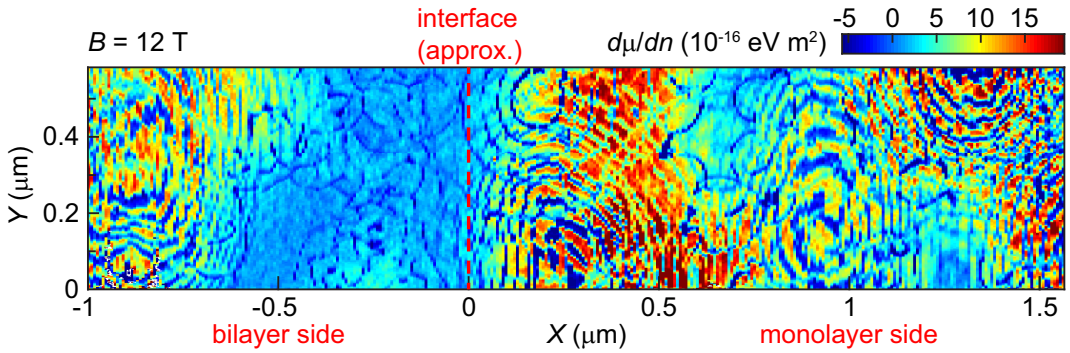

Figure 7.3: Inverse compressibility at $\nu = 0$ as a function of X and Y position at $B = 12$ T. Incompressible behavior occurs on both the monolayer and bilayer sides of the sample, but the interface is more compressible. Localized states are visible as dark blue ovals. None are centered at the interface, which occurs at approximately $X = 0$. The measured inverse compressibility is artificially enhanced due to the large resistance of the flake.

monolayer-bilayer boundary. Localized states only form in the presence of an energy gap [13], so their absence suggests that no energy gap is present at the interface. The same behavior also occurs in a linecut across the boundary taken at $B = 1$ T (Fig. 7.4). Although a spectrum of localized states (dark blue arcs) are clearly apparent in both the monolayer and the bilayer regions, none occur at the interface, which is compressible.

These findings suggest that the energy gap of the $\nu = 0$ broken-symmetry state weakens or closes at the interface. Such behavior could be caused by a band crossing and corresponding edge mode along the interface, which could arise if the nature of the broken-symmetry states in the monolayer and bilayer regions is different. Alternatively, recent experiments indicate that the $\nu = 0$ state is likely a canted antiferromagnet in both monolayer and bilayer graphene [47, 48]. At the physical edge of monolayer and bilayer samples in this state, the energy gap is predicted to partially close, as well as form interesting spin textures [150]. If similar behavior also occurs at the monolayer-bilayer boundary, it could account for the experimental findings described above. Finally, increased compressibility could also arise if the interface is dirty, *e.g.* because the edge termination attracts chemical adsorbates. Fur-

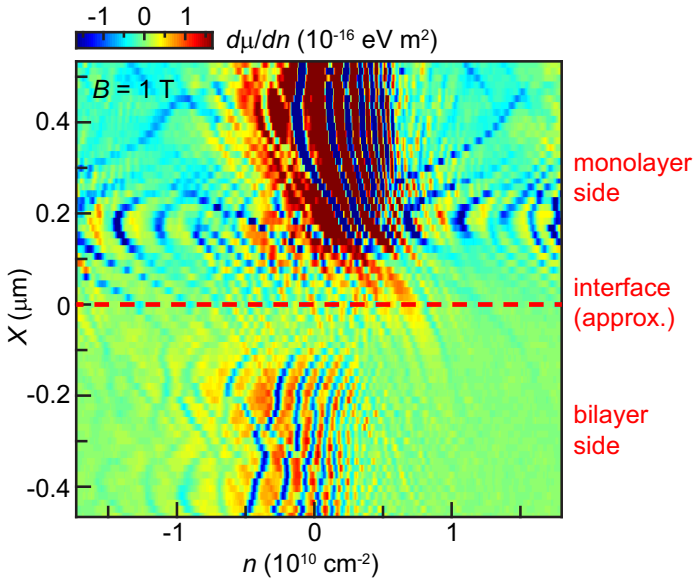

Figure 7.4: Inverse compressibility at $B = 1$ T as a function of carrier density n and position along the sample. The incompressible $\nu = 0$ state is visible on both the monolayer and bilayer sides of the sample, but the interface is compressible. No localized states, which appear as dark blue arcs, are centered at the interface, which occurs at approximately $X = 0$. The inverse compressibility at $\nu = 0$ is artificially enhanced due to the large resistance of the flake. Data were taken after current annealing the sample.

ther study is required to pinpoint the dominant cause of the compressible behavior around $\nu = 0$ at the interface.

7.4 Reproducibility and Outlook

The qualitative behavior described above was unchanged by current annealing the flake to remove disorder, as illustrated by the analogous measurements in Fig. 7.5. The sample became even cleaner, leading to fewer localized states and sharper incompressible peaks, as well as more broken-symmetry states. The changes of the $\nu = 0$ and ± 2 states at the boundary were still apparent, providing further evidence for the behavior described above. Nonetheless, the measurements were performed on only one sample, and therefore should be corroborated before sweeping conclusions can be made.

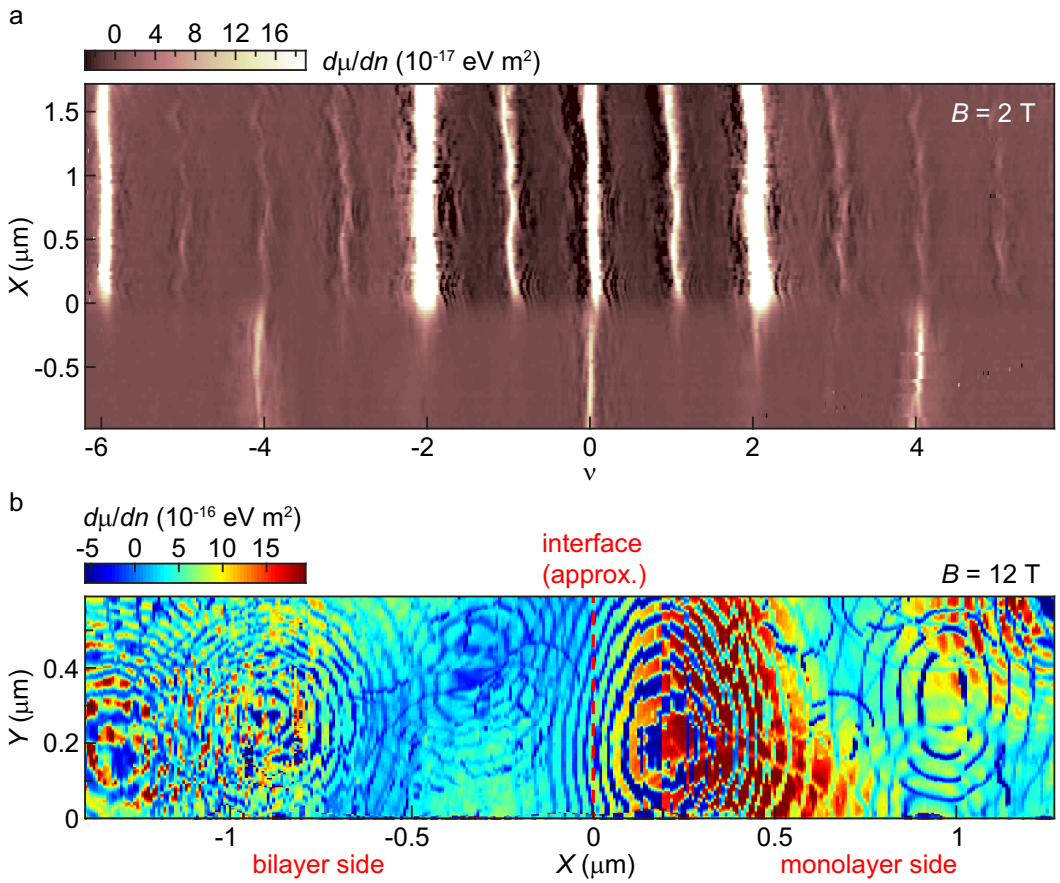

Figure 7.5: (a) Inverse compressibility as a function of filling factor and position X at $B = 2$ T after current annealing. As was the case before annealing, the interface is more compressible at the charge neutrality point, and the $\nu = \pm 2$ states are sharper and stronger at the monolayer-bilayer boundary. (b) Inverse compressibility at $\nu = 0$ as a function of X and Y position. Fewer localized states are present than before, indicating a cleaner sample, but the qualitative behavior is unchanged. The monolayer and bilayer sides are both more incompressible than the boundary between them, and no localized states are centered at the interface.

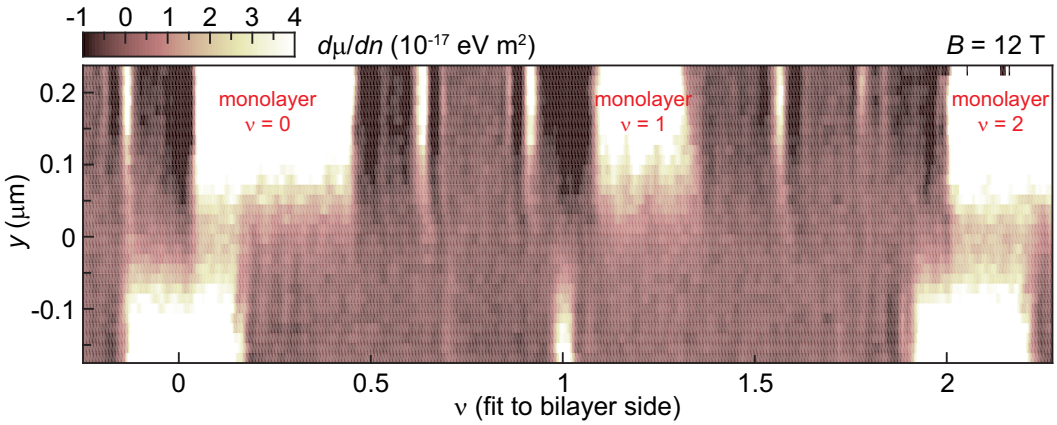

Figure 7.6: Inverse compressibility as a function of filling factor and position y at $B = 12$ T in a sample on boron nitride. Although the states do not occur at exactly the same gate voltage, the sample appears to be more compressible at the monolayer-bilayer boundary for both $\nu = 0$ and 2. The differences in the positions of the incompressible peaks may be caused by differences in doping and also by the different densities of states on each side, an effect exacerbated by the large geometric capacitance of the nearby gate. Weaker incompressible FQH states are also visible.

We have also fabricated a monolayer-bilayer hybrid device on a Si/SiO_2/graphite/boron nitride stack (the same sample whose bilayer properties are discussed in detail in Chapter 6). As for the suspended sample, the interface appears to show an increase in compressibility at the charge neutrality point (Fig. 7.6). However, the comparison is made more difficult because the $\nu = 0$ states on either side do not occur at exactly the same gate voltage. Moreover, the nature of the $\nu = 0$ state on the bilayer side is likely different in the boron nitride sample due to the strong asymmetry in the environment of each layer; the energy gap is approximately constant in magnetic field, suggesting valley polarization rather than a canted antiferromagnet [44]. Despite the limited number and nature of the samples explored, the data suggest that interesting effects may occur at the boundary between monolayer and bilayer graphene, and further exploration of these phenomena represents an exciting avenue to pursue.

Appendix A

Fabrication of Suspended Graphene Samples

Many of the experimental findings described in this thesis were apparent only because the devices were exceptionally clean. This appendix describes the fabrication of suspended graphene flakes, which follows a method similar to that presented in ref. [58].

A.1 Fabrication of Suspended Devices

Mechanical exfoliation of highly oriented pyrolytic graphite (grade ZYA, SPI Supplies) is used to deposit few-layer graphene flakes on a Si substrate coated with 300 nm of SiO_2. Deposition is carried out at 180 °C to minimize the amount of water present on the substrate. Suitable flakes are identified using an optical microscope, on the basis of contrast between the flake and the surrounding substrate. Electrical leads are then patterned using electron-beam lithography, followed by thermal evaporation of 3 nm of Cr and 100 nm of Au, and subsequent liftoff in warm acetone. The entire substrate is then immersed in 5:1 buffered oxide etch for 90 s, which etches approximately 40% of the SiO_2, including the area under

the graphene [58], but not the area under the metal contacts, which extend across the entire width of the flake to improve structural integrity. Finally, samples are transferred to methanol and dried using a critical point dryer. Finished devices are inserted into the measurement system as quickly as possible.

A.2 Current Annealing

Although some measurements were performed without further cleaning, more recently we have current annealed the samples by applying a source-drain voltage $V_{sd} \approx$ 1-3 V across the graphene. Graphene can sustain about 0.7 mA per μm width before the sample is destroyed, and we typically start with $V_{sd} \approx$ 0.5-1 V, and gradually increase it until the Dirac peak is sharp. Current annealing can be performed in liquid helium or in vacuum at low temperatures.

Appendix B

Scanning Single-Electron Transistor Microscope

The fabrication process for preparing the single-electron transistor (SET) tips used in Chapters 3-7 is described below. Some additional tips and tricks for running the scanning SET microscope are also provided. Additional information about operation and maintenance of the microscope is detailed in ref. [151].

B.1 SET Fabrication

Scanning probe tips are fabricated using a fiber puller to generate a conical taper at the end of a quartz rod. Al (16-19 nm) is thermally evaporated onto either side of the quartz rod to generate the two leads of the SET. Following a brief oxidation step, another thin (6-19 nm) layer of Al is evaporated onto the end of the conical tip to serve as the island of the SET. A second oxidation step completes the fabrication process. Tip size ranges from approximately 100 to 200 nm, and the tip is held between 50 and 200 nm above the flake during measurement.

B.2 Tips and Tricks for Running the Microscope

The scanning SET microscope functions exceptionally well given the many parts that must all work in concert. However, certain problems arise fairly frequently, and some potential solutions are detailed below. A few software improvements that were implemented over the past few years are also described.

B.2.1 Fixing a noisy SET tip

Several different methods can be used to try and fix a noisy SET tip without going through the painstaking process of preparing and inserting a new one. Perhaps most straightforward is applying a large source-drain bias across the SET. The rationale behind this approach is that the large electric field in the tunnel junctions will push any trapped charges onto either the island or one of the leads. Applying as much as 15-20 mV is fairly routine, and should not damage the SET. We once applied 100 mV at room temperature overnight, and the SET not only survived, but also behaved exceptionally well afterward.

A second method is to apply a large bias between the tip and the sample. This produces a large electric field, and in principle, should also push any trapped charges away from the oxide barriers near the island. Moving as many as 40 electrons out of flat band is perfectly safe. Typically, we increase the electric field over a timescale of several minutes, and the maximum electric field can be maintained anywhere from several minutes to several hours.

Finally, there have been several occasions where a noisy tip was heated to room temperature by raising the microscope rod, usually associated with sample changes such that the high temperature was maintained for hour-long timescales. This always seems to improve the noise level of the tip dramatically. The one time that we did it without changing or moving the sample, the tip drifted only slightly out of the previous fine scan range ($\sim$10 μm).

B.2.2 Sticky coarse motors

Coarse positioning of the SET tip is accomplished at ^{3}He temperatures using slip-stick motion of piezoelectric stacks. Unfortunately, this motion can often get stuck for the X and Y directions, and it is least reliable in the $-Y$ direction. Several techniques can be used to unstick the SET. First, while cooling down the microscope from room temperature immediately after inserting a new tip or sample, it can be helpful to periodically take approximately 100 coarse steps in a particular direction. This is meant to avoid water or other molecules freezing around the piezoelectric stacks and creating barriers.

If the motion is still stuck, increasing the coarse step frequency or power can help, although this introduces more crosstalk with other wires, and can also make the SET noisier. You should never use 100% power, as this will destroy the SET. This is an effect which has been reproduced at both Weizmann and Harvard, so don't waste your time.

Sometimes, the coarse motion can be jump-started by taking steps in continuous mode for some amount of time. The friction can heat the sapphire stage locally and unstick the piezos so that they perform slip-stick motion. Start slowly (at most 0.5 s), because the tip moves very quickly once it starts to move at all; three bouts of continuous mode in quick succession, for 30 s each, once unstuck a stubborn tip in the $-Y$ direction, but further time increases are probably not worthwhile. Note that this can also make the tip noisier. Once the tip has moved after the initial cooldown, motion often becomes easier from then onward. As a last resort, the microscope rod can be raised, and the tip can be repositioned at room temperature, which is particularly useful if one direction is especially problematic and you know where the tip sits relative to the sample.

B.2.3 Matching positions after system warmup

Long scans will often require more time to complete than the helium hold time allows. For delicate position-sensitive measurements, such as n-B sweeps, one must therefore match the position of the current scan to the previous one. This is often more difficult than it might seem because walking in the microscope room during helium transfers can shift the position of the tip.

As a starting point, use the relative positions indicated by the XY maps. The easiest way to match position is to look at the pattern of localized states and the magnitudes of any steps in chemical potential. If you are close to the correct position, moving in 0.05 V steps in X or Y can produce a meaningful change in behavior. Otherwise, you might want to save time by changing position in 0.1 V increments. It is also worth noting that the scanner seems to have some hysteresis, so that moving 0.1 V in $+X$ followed by 0.1 V in $-X$ does not always cause the behavior to revert back exactly. This type of discrepancy is often fixed simply by resuming the ramping of magnetic field, so a good strategy is to start at a magnetic field where you already have data, and simply throw out the first line of the new data. The V_{TOP} setpoint can also affect behavior.

Changing X and Y position significantly can also cause the position to shift slightly when you start ramping the field. So if you have had to move around a lot to find the perfect position match, be wary and watch the second line of the data as well. If you simply cannot match the position, it is worthwhile to try the position where you ended the previous scan, even if it seems far from ideal based on the XY map. Empirically, we have found that this sometimes works, which might be an indication of imperfect position correction with magnetic field, or might simply reflect some hysteresis or uncertainty in the XY map.

B.2.4 Hardware and software updates

Various improvements to the measurement software and hardware have been made over the past few years, and some important ones are described below. For Matlab functions, further comments are also given in the m-file code.

Perhaps the most important and often used improvements relate to single-step coarse motor control through the Special Measure software. The coarse motors have a dedicated Special Measure instrument, and @smcCoarseStep is the control function. The number of steps to be taken at a time is defined in smdata.inst(4).data.stepnum (4 should be replaced by the coarse motor instrument number if the rack is changed). The basic workflow is that Special Measure software sends a signal to the measurement hardware that it should first zero the SET bias, followed by other user-defined channels, typically back gate and sample voltages. The DecaDac channel that controls the field-effect transistor in the microscope then supplies -10 V to ground the SET, and after a 2 s wait time, a 0.25-second 5 V square pulse is applied to the relay box using the relevant DecaDac channel. This then triggers a short pulse that mimics a button being pressed on the remote box for coarse motion. Finally, the coarse motor will perform a step (accompanied by an audible click in the control room). After the specified number of steps has been taken, the SET is ungrounded, and after another 2 s of wait time, the SET and other voltages are returned to their original values.

The magnet and its power supply have also changed because we are using a compensated magnet to avoid interfering with TEM focusing on the basement floor. The new magnet power supply has a control function @smcCS410V. It can be used in either FIELD mode, for normal operation, or RAMP mode, in which a long ramp is started and data is taken as the field is swept. For the latter, the field should be recorded at each data point.

Some minor changes have been made to the @smcLinearCombination instrument originally written by Vivek Venkatachalam. To make it safe for controlling fine X' and Y'

motion, the ramp time in each direction is the same so that the tip will move in a straight line. This avoids inadvertently crashing into a contact in cases where ΔX is much larger than ΔY, or vice versa. The setfeedback function has also been tweaked slightly. It can be used to allow for feedback on both sides of the Coulomb blockade oscillations, or it can accept only one slope. The latter is useful for obtaining the energy gaps of very incompressible integer quantum Hall states.

Bibliography

[1] K. v. Klitzing, G. Dorda, and M. Pepper, New method for high-accuracy determination of the fine-structure constant based on quantized Hall resistance, *Phys. Rev. Lett.* **45**, 494 (1980).

[2] D. C. Tsui, H. L. Stormer, and A. C. Gossard, Two-dimensional magnetotransoprt in the extreme quantum limit, *Phys. Rev. Lett.* **48**, 1559 (1982).

[3] K. S. Novoselov, A. K. Geim, S. V. Morozov, D. Jiang, Y. Zhang, S. V. Dubonos, I. V. Grigorieva, and A. A. Firsov, Electric field effect in atomically thin carbon films, *Science* **306**, 666 (2004).

[4] R. E. Peierls, Quelques proprietes typiques des corpses solides, *Ann. I. H. Poincare* **5**, 177 (1935).

[5] P. R. Wallace, The band theory of graphite, *Phys. Rev.* **71**, 622 (1947).

[6] A. H. Castro Neto, F. Guinea, N. M. R. Peres, K. S. Novoselov, and A. K. Geim, The electronic properties of graphene, *Rev. Mod. Phys.* **81**, 109 (2009).

[7] E. McCann, and V. I. Fal'ko, Landau-level degeneracy and quantum Hall effect in a graphite bilayer, *Phys. Rev. Lett.* **96**, 086805 (2006).

[8] E. A. Henriksen, and J. P. Eisenstein, Measurement of the electronic compressibility of bilayer graphene, *Phys. Rev. B* **82**, 041412 (2010).

[9] E. McCann, Asymmetry gap in the electronic band structure of bilayer graphene, *Phys. Rev. B* **74**, 161403 (2006).

[10] E. V. Castro, K. S. Novoselov, S. V. Morozov, N. M. R. Peres, J. Dos Santos, J. Nilsson, F. Guinea, A. K. Geim, and A. H. C. Neto, Biased bilayer graphene: Semiconductor with a gap tunable by the electric field effect, *Phys. Rev. Lett.* **99**, 216802 (2007).

[11] J. B. Oostinga, H. B. Heersche, X. L. Liu, A. F. Morpurgo, and L. M. K. Vandersypen, Gate-induced insulating state in bilayer graphene devices, *Nat. Mater.* **7**, 151 (2008).

[12] J. K. Jain, *Composite Fermions* (Cambridge University Press, 2007).

[13] S. Ilani, J. Martin, E. Teitelbaum, J. H. Smet, D. Mahalu, V. Umansky, and A. Yacoby, The microscopic nature of localization in the quantum Hall effect, *Nature* **427**, 328 (2004).

[14] K. S. Novoselov, A. K. Geim, S. V. Morozov, D. Jiang, M. I. Katsnelson, I. V. Grigorieva, S. V. Dubonos, and A. A. Firsov, Two-dimensional gas of massless Dirac fermions in graphene, *Nature* **438**, 197 (2005).

[15] Y. B. Zhang, Y. W. Tan, H. L. Stormer, and P. Kim, Experimental observation of the quantum Hall effect and Berry's phase in graphene, *Nature* **438**, 201 (2005).

[16] K. S. Novoselov, E. McCann, S. V. Morozov, V. I. Fal'ko, M. I. Katsnelson, U. Zeitler, D. Jiang, F. Schedin, and A. K. Geim, Unconventional quantum Hall effect and Berry's phase of 2π in bilayer graphene, *Nat. Phys.* **2**, 177 (2006).

[17] Y. Barlas, R. Cote, K. Nomura, and A. H. MacDonald, Intra-Landau-level cyclotron resonance in bilayer graphene, *Phys. Rev. Lett.* **101**, 097601 (2008).

[18] N. W. Ashcroft, and N. D. Mermin, *Solid State Physics* (Brooks/Cole, Cengage Learning, 1976).

[19] J. P. Eisenstein, L. N. Pfeiffer, and K. W. West, Compressibility of the 2-dimensional electron gas - measurements of the zero-field exchange energy and fractional quantum Hall gap, *Phys. Rev. B* **50**, 1760 (1994).

[20] H. Min, G. Borghi, M. Polini, and A. H. MacDonald, Pseudospin magnetism in graphene, *Phys. Rev. B* **77**, 041407 (2008).

[21] F. Zhang, H. Min, M. Polini, and A. H. MacDonald, Spontaneous inversion symmetry breaking in graphene bilayers, *Phys. Rev. B* **81**, 041402 (2010).

[22] R. Nandkishore, and L. Levitov, Dynamical screening and excitonic instability in bilayer graphene, *Phys. Rev. Lett.* **104**, 156803 (2010).

[23] O. Vafek, and K. Yang, Many-body instability of Coulomb interacting bilayer graphene: Renormalization group approach, *Phys. Rev. B* **81**, 041401 (2010).

[24] Y. Lemonik, I. L. Aleiner, C. Toke, and V. I. Fal'ko, Spontaneous symmetry breaking and Lifshitz transition in bilayer graphene, *Phys. Rev. B* **82**, 201408 (2010).

[25] F. D. M. Haldane, Model for a quantum Hall-effect without Landau-levels - condensed-matter realization of the parity anomaly, *Phys. Rev. Lett.* **61**, 2015 (1988).

[26] S. Raghu, X. L. Qi, C. Honerkamp, and S. C. Zhang, Topological Mott insulators, *Phys. Rev. Lett.* **100**, 156401 (2008).

[27] R. Nandkishore, and L. Levitov, Quantum anomalous Hall state in bilayer graphene, *Phys. Rev. B* **82**, 115124 (2010).

[28] R. Nandkishore, and L. Levitov, Quantum anomalous Hall state in bilayer graphene, *arXiv: 1009.0497v1* (2010).

[29] R. E. Throckmorton, and O. Vafek, Fermions on bilayer graphene: Symmetry breaking for $B = 0$ and $\nu = 0$, *Phys. Rev. B* **86**, 115447 (2012).

[30] K. Nomura, and A. H. MacDonald, Quantum Hall ferromagnetism in graphene, *Phys. Rev. Lett.* **96**, 256602 (2006).

[31] J. Alicea, and M. P. A. Fisher, Graphene integer quantum Hall effect in the ferromagnetic and paramagnetic regimes, *Phys. Rev. B* **74**, 075422 (2006).

[32] V. P. Gusynin, V. A. Miransky, S. G. Sharapov, and I. A. Shovkovy, Excitonic gap, phase transition, and quantum Hall effect in graphene, *Phys. Rev. B* **74**, 195429 (2006).

[33] D. V. Khveshchenko, Composite Dirac fermions in graphene, *Phys. Rev. B* **75**, 153405 (2007).

[34] A. J. M. Giesbers, L. A. Ponomarenko, K. S. Novoselov, A. K. Geim, M. I. Katsnelson, J. C. Maan, and U. Zeitler, Gap opening in the zeroth Landau level of graphene, *Phys. Rev. B* **80**, 201403 (2009).

[35] J. G. Checkelsky, L. Li, and N. P. Ong, Zero-energy state in graphene in a high magnetic field, *Phys. Rev. Lett.* **100**, 206801 (2008).

[36] J. G. Checkelsky, L. Li, and N. P. Ong, Divergent resistance at the Dirac point in graphene: Evidence for a transition in a high magnetic field, *Phys. Rev. B* **79**, 115434 (2009).

[37] L. Zhang, J. Camacho, H. Cao, Y. P. Chen, M. Khodas, D. E. Kharzeev, A. M. Tsvelik, T. Valla, and I. A. Zaliznyak, Breakdown of the $N = 0$ quantum Hall state in graphene: Two insulating regimes, *Phys. Rev. B* **80**, 241412 (2009).

[38] Z. Jiang, Y. Zhang, H. L. Stormer, and P. Kim, Quantum Hall states near the charge-neutral Dirac point in graphene, *Phys. Rev. Lett.* **99**, 106802 (2007).

[39] Y. Zhang, Z. Jiang, J. P. Small, M. S. Purewal, Y. W. Tan, M. Fazlollahi, J. D. Chudow, J. A. Jaszczak, H. L. Stormer, and P. Kim, Landau-level splitting in graphene in high magnetic fields, *Phys. Rev. Lett.* **96**, 136806 (2006).

[40] D. A. Abanin, K. S. Novoselov, U. Zeitler, P. A. Lee, A. K. Geim, and L. S. Levitov, Dissipative quantum Hall effect in graphene near the Dirac point, *Phys. Rev. Lett.* **98**, 196806 (2007).

[41] A. F. Young, C. R. Dean, L. Wang, H. Ren, P. Cadden-Zimansky, K. Watanabe, T. Taniguchi, J. Hone, K. L. Shepard, and P. Kim, Spin and valley quantum Hall ferromagnetism in graphene, *Nat. Phys.* **8**, 550 (2012).

[42] J. Jung, and A. H. MacDonald, Theory of the magnetic-field-induced insulator in neutral graphene sheets, *Phys. Rev. B* **80**, 235417 (2009).

[43] M. Kharitonov, Phase diagram for the $\nu = 0$ quantum Hall state in monolayer graphene, *Phys. Rev. B* **85**, 155439 (2012).

[44] M. Kharitonov, Canted antiferromagnetic phase of the $\nu = 0$ quantum Hall state in bilayer graphene, *Phys. Rev. Lett.* **109**, 046803 (2012).

[45] K. Nomura, S. Ryu, and D.-H. Lee, Field-induced Kosterlitz-Thouless transition in the $N = 0$ Landau level of graphene, *Phys. Rev. Lett.* **103**, 216801 (2009).

[46] C.-Y. Hou, C. Chamon, and C. Mudry, Deconfined fractional electric charges in graphene at high magnetic fields, *Phys. Rev. B* **81**, 075427 (2010).

[47] A. F. Young, J. D. Sanchez-Yamagishi, B. Hunt, S. H. Choi, K. Watanabe, T. Taniguchi, R. C. Ashoori, and P. Jarillo-Herrero, Tunable symmetry breaking and helical edge transport in a graphene quantum spin Hall state, *arXiv: 1307.5104v1* (2013).

[48] P. Maher, C. R. Dean, A. F. Young, T. Taniguchi, K. Watanabe, K. L. Shepard, J. Hone, and P. Kim, Evidence for a spin phase transition at charge neutrality in bilayer graphene, *Nat. Phys.* **9**, 154 (2013).

[49] R. B. Laughlin, Anomalous quantum Hall-effect - an incompressible quantum fluid with fractionally charged excitations, *Phys. Rev. Lett.* **50**, 1395 (1983).

[50] B. I. Halperin, Theory of the quantized hall conductance, *Helv. Phys. Acta* **56**, 75 (1983).

[51] J. Martin, S. Ilani, B. Verdene, J. Smet, V. Umansky, D. Mahalu, D. Schuh, G. Abstreiter, and A. Yacoby, Localization of fractionally charged quasi-particles, *Science* **305**, 980 (2004).

[52] J. K. Jain, Composite-fermion approach for the fractional quantum Hall-effect, *Phys. Rev. Lett.* **63**, 199 (1989).

[53] C. R. Dean, A. F. Young, P. Cadden-Zimansky, L. Wang, H. Ren, K. Watanabe, T. Taniguchi, P. Kim, J. Hone, and K. L. Shepard, Multicomponent fractional quantum Hall effect in graphene, *Nat. Phys.* **7**, 693 (2011).

[54] D. A. Abanin, B. E. Feldman, A. Yacoby, and B. I. Halperin, Fractional and integer quantum Hall effects in the zeroth Landau level in graphene, *arXiv: 1303.5372v1* (2013).

[55] Z. Papic, and D. A. Abanin, Topological phases in the zeroth Landau level of bilayer graphene, *arXiv: 1307.2909v1* (2013).

[56] M. A. Kastner, The single-electron transistor, *Rev. Mod. Phys.* **64**, 849 (1992).

[57] J. P. Eisenstein, L. N. Pfeiffer, and K. W. West, Negative compressibility of interacting 2-dimensional electron and quasi-particle gases, *Phys. Rev. Lett.* **68**, 674 (1992).

[58] K. I. Bolotin, K. J. Sikes, Z. Jiang, M. Klima, G. Fudenberg, J. Hone, P. Kim, and H. L. Stormer, Ultrahigh electron mobility in suspended graphene, *Solid State Commun.* **146**, 351 (2008).

[59] X. Du, I. Skachko, A. Barker, and E. Y. Andrei, Approaching ballistic transport in suspended graphene, *Nat. Nanotechnol.* **3**, 491 (2008).

[60] M. Ezawa, Intrinsic Zeeman effect in graphene, *J. Phys. Soc. Jpn.* **76**, 094701 (2007).

[61] D. A. Abanin, S. A. Parameswaran, and S. L. Sondhi, Charge 2e skyrmions in bilayer graphene, *Phys. Rev. Lett.* **103**, 076802 (2009).

[62] S. V. Morozov, K. S. Novoselov, M. I. Katsnelson, F. Schedin, D. C. Elias, J. A. Jaszczak, and A. K. Geim, Giant intrinsic carrier mobilities in graphene and its bilayer, *Phys. Rev. Lett.* **100**, 016602 (2008).

[63] J. Martin, N. Akerman, G. Ulbricht, T. Lohmann, J. H. Smet, K. Von Klitzing, and A. Yacoby, Observation of electron-hole puddles in graphene using a scanning single-electron transistor, *Nat. Phys.* **4**, 144 (2008).

[64] S. Adam, and S. Das Sarma, Boltzmann transport and residual conductivity in bilayer graphene, *Phys. Rev. B* **77**, 115436 (2008).

[65] M. I. Katsnelson, Minimal conductivity in bilayer graphene, *Eur. Phys. J. B* **52**, 151 (2006).

[66] I. Snyman, and C. W. J. Beenakker, Ballistic transmission through a graphene bilayer, *Phys. Rev. B* **75**, 045322 (2007).

[67] D. A. Abanin, P. A. Lee, and L. S. Levitov, Randomness-induced XY ordering in a graphene quantum Hall ferromagnet, *Phys. Rev. Lett.* **98**, 156801 (2007).

[68] W. Z. Bao, F. Miao, Z. Chen, H. Zhang, W. Y. Jang, C. Dames, and C. N. Lau, Controlled ripple texturing of suspended graphene and ultrathin graphite membranes, *Nat. Nanotechnol.* **4**, 562 (2009).

[69] D. V. Khveshchenko, Magnetic-field-induced insulating behavior in highly oriented pyrolitic graphite, *Phys. Rev. Lett.* **87**, 206401 (2001).

[70] E. V. Gorbar, V. P. Gusynin, V. A. Miransky, and I. A. Shovkovy, Magnetic field driven metal-insulator phase transition in planar systems, *Phys. Rev. B* **66**, 045108 (2002).

[71] V. T. Dolgopolov, A. A. Shashkin, A. V. Aristov, D. Schmerek, W. Hansen, J. P. Kotthaus, and M. Holland, Direct measurements of the spin gap in the two-dimensional electron gas of AlGaAs-GaAs heterojunctions, *Phys. Rev. Lett.* **79**, 729 (1997).

[72] B. E. Feldman, J. Martin, and A. Yacoby, Broken-symmetry states and divergent resistance in suspended bilayer graphene, *Nat. Phys.* **5**, 889 (2009).

[73] Y. Zhao, P. Cadden-Zimansky, Z. Jiang, and P. Kim, Symmetry breaking in the zero-energy Landau level in bilayer graphene, *Phys. Rev. Lett.* **104**, 066801 (2010).

[74] W. Z. Bao, Z. Zhao, H. Zhang, G. Liu, P. Kratz, L. Jing, J. Velasco, D. Smirnov, and C. N. Lau, Magnetoconductance oscillations and evidence for fractional quantum Hall states in suspended bilayer and trilayer graphene, *Phys. Rev. Lett.* **105**, 246601 (2010).

[75] C. R. Dean, A. F. Young, I. Meric, C. Lee, L. Wang, S. Sorgenfrei, K. Watanabe, T. Taniguchi, P. Kim, K. L. Shepard, and J. Hone, Boron nitride substrates for high-quality graphene electronics, *Nat. Nanotechnol.* **5**, 722 (2010).

[76] Y. B. Zhang, T. T. Tang, C. Girit, Z. Hao, M. C. Martin, A. Zettl, M. F. Crommie, Y. R. Shen, and F. Wang, Direct observation of a widely tunable bandgap in bilayer graphene, *Nature* **459**, 820 (2009).

[77] M. J. Yoo, T. A. Fulton, H. F. Hess, R. L. Willett, L. N. Dunkleberger, R. J. Chichester, L. N. Pfeiffer, and K. W. West, Scanning single-electron transistor microscopy: Imaging individual charges, *Science* **276**, 579 (1997).

[78] A. Yacoby, H. F. Hess, T. A. Fulton, L. N. Pfeiffer, and K. W. West, Electrical imaging of the quantum Hall state, *Solid State Commun.* **111**, 1 (1999).

[79] J. Martin, N. Akerman, G. Ulbricht, T. Lohmann, K. von Klitzing, J. H. Smet, and A. Yacoby, The nature of localization in graphene under quantum Hall conditions, *Nat. Phys.* **5**, 669 (2009).

[80] A. F. Young, C. R. Dean, I. Meric, S. Sorgenfrei, H. Ren, K. Watanabe, T. Taniguchi, J. Hone, K. L. Shepard, and P. Kim, Electronic compressibility of layer-polarized bilayer graphene, *Phys. Rev. B* **85**, 235458 (2010).

[81] E. A. Henriksen, Z. Jiang, L.-C. Tung, M. E. Scwartz, M. Takita, Y.-J. Wang, P. Kim, and H. L. Stormer, Cyclotron resonance in bilayer graphene, *Phys. Rev. Lett.* **100**, 087403 (2008).

[82] E. Gorbar, V. P. Gusynin, and V. A. Miransky, Energy gaps at neutrality point in bilayer graphene in a magnetic field, *JETP Lett.* **91**, 314 (2010).

[83] E. V. Gorbar, V. P. Gusynin, and V. A. Miransky, Dynamics and phase diagram of the $\nu = 0$ quantum Hall state in bilayer graphene, *Phys. Rev. B* **81**, 155451 (2010).

[84] A. J. M. Giesbers, U. Zeitler, M. I. Katsnelson, L. A. Ponomarenko, T. M. Mohiuddin, and J. C. Maan, Quantum-Hall activation gaps in graphene, *Phys. Rev. Lett.* **99**, 206803 (2007).

[85] M. I. Katsnelson, and M. F. Prokhorova, Zero-energy states in corrugated bilayer graphene, *Phys. Rev. B* **77**, 205424 (2008).

[86] J. Kailasvuori, Pedestrian index theorem a la Aharonov-Casher for bulk threshold modes in corrugated multilayer graphene, *Europhys. Lett.* **87**, 47008 (2009).

[87] S. Kusminskiy, J. Nilsson, D. K. Campbell, and A. H. Castro Neto, Electronic compressibility of a graphene bilayer, *Phys. Rev. Lett.* **100**, 106805 (2008).

[88] G. Borghi, M. Polini, R. Asgari, and A. H. MacDonald, Compressibility of the electron gas in bilayer graphene, *Phys. Rev. B* **82**, 155403 (2010).

[89] J. Velasco, G. Liu, L. Jing, P. Kratz, H. Zhang, W. Z. Bao, M. Bockrath, and C. N. Lau, Probing charging and localization in the quantum Hall regime by graphene p-n-p junctions, *Phys. Rev. B* **81**, 121407 (2010).

[90] R. T. Weitz, M. T. Allen, B. E. Feldman, J. Martin, and A. Yacoby, Broken-symmetry states in doubly gated suspended bilayer graphene, *Science* **330**, 812 (2010).

[91] S. Kim, K. Lee, and E. Tutuc, Spin-polarized to valley-polarized transition in graphene bilayers at $\nu = 0$ in high magnetic fields, *Phys. Rev. Lett.* **107**, 016803 (2011).

[92] J. Velasco, L. Jing, W. Bao, Y. Lee, P. Kratz, V. Aji, M. Bockrath, C. N. Lau, C. Varma, R. Stillwell, D. Smirnov, F. Zhang, J. Jung, and A. H. MacDonald, Transport spectroscopy of symmetry-broken insulating states in bilayer graphene, *Nat. Nanotechnol.* **7**, 156 (2012).

[93] A. S. Mayorov, D. C. Elias, M. Mucha-Kruczynski, R. V. Gorbachev, T. Tudorovskiy, A. Zhukov, S. V. Morozov, M. I. Katsnelson, V. I. Falko, A. K. Geim, and K. S. Novoselov, Interaction-driven spectrum reconstruction in bilayer graphene, *Science* **333**, 860 (2011).

[94] F. Freitag, J. Trbovic, M. Weiss, and C. Schönenberger, Spontaneously gapped ground state in suspended bilayer graphene, *Phys. Rev. Lett.* **108**, 076602 (2012).

[95] M. Mucha-Kruczyński, I. L. Aleiner, and V. I. Fal'ko, Strained bilayer graphene: Band structure topology and Landau level spectrum, *Phys. Rev. B* **84**, 041404 (2011).

[96] V. M. Apalkov, and T. Chakraborty, Fractional quantum Hall states of Dirac electrons in graphene, *Phys. Rev. Lett.* **97**, 126801 (2006).

[97] C. Toke, P. E. Lammert, V. H. Crespi, and J. K. Jain, Fractional quantum Hall effect in graphene, *Phys. Rev. B* **74**, 235417 (2006).

[98] M. O. Goerbig, and N. Regnault, Analysis of a SU(4) generalization of Halperin's wave function as an approach towards a SU(4) fractional quantum Hall effect in graphene sheets, *Phys. Rev. B* **75**, 241405 (2007).

[99] C. Toke, and J. K. Jain, SU(4) composite fermions in graphene: Fractional quantum Hall states without analog in GaAs, *Phys. Rev. B* **75**, 245440 (2007).

[100] K. Yang, S. Das Sarma, and A. H. MacDonald, Collective modes and skyrmion excitations in graphene SU(4) quantum Hall ferromagnets, *Phys. Rev. B* **74**, 075423 (2006).

[101] N. Shibata, and K. Nomura, Coupled charge and valley excitations in graphene quantum Hall ferromagnets, *Phys. Rev. B* **77**, 235426 (2008).

[102] N. Shibata, and K. Nomura, Fractional quantum Hall effects in graphene and its bilayer, *J. Phys. Soc. Jpn.* **78**, 104708 (2009).

[103] Z. Papic, M. O. Goerbig, and N. Regnault, Theoretical expectations for a fractional quantum Hall effect in graphene, *Solid State Commun.* **149**, 1056 (2009).

[104] Z. Papic, M. O. Goerbig, and N. Regnault, Atypical fractional quantum Hall effect in graphene at filling factor 1/3, *Phys. Rev. Lett.* **105**, 176802 (2010).

[105] S. Modak, S. S. Mandal, and K. Sengupta, Fermionic Chern-Simons theory of SU(4) fractional quantum Hall effect, *Phys. Rev. B* **84**, 165118 (2011).

[106] Z. Papic, D. A. Abanin, Y. Barlas, and R. N. Bhatt, Tunable interactions and phase transitions in Dirac materials in a magnetic field, *Phys. Rev. B* **84**, 241306 (2011).

[107] C. Toke, and J. K. Jain, Multi-component fractional quantum Hall states in graphene: SU(4) versus SU(2), *J. Phys. Condens. Matter* **24**, 235601 (2012).

[108] M. O. Goerbig, and N. Regnault, Theoretical aspects of the fractional quantum Hall effect in graphene, *Nat. Nanotechnol.* **T146**, 014017 (2012).

[109] F. Ghahari, Y. Zhao, P. Cadden-Zimansky, K. Bolotin, and P. Kim, Measurement of the $\nu = 1/3$ fractional quantum Hall energy gap in suspended graphene, *Phys. Rev. Lett.* **106**, 046801 (2011).

[110] X. Du, I. Skachko, F. Duerr, A. Luican, and E. Y. Andrei, Fractional quantum Hall effect and insulating phase of dirac electrons in graphene, *Nature* **462**, 192 (2009).

[111] D. S. Lee, V. Skakalova, R. T. Weitz, K. von Klitzing, and J. H. Smet, Transconductance fluctuations as a probe for interaction-induced quantum Hall states in graphene, *Phys. Rev. Lett.* **109**, 056602 (2012).

[112] Z. Jiang, E. A. Henriksen, L. C. Tung, Y. J. Wang, M. E. Schwartz, M. Y. Han, P. Kim, and H. L. Stormer, Infrared spectroscopy of Landau levels of graphene, *Phys. Rev. Lett.* **98**, 197403 (2007).

[113] K. Lai, W. Pan, D. C. Tsui, S. Lyon, M. Muhlberger, and F. Schaffler, Two-flux composite fermion series of the fractional quantum Hall states in strained Si, *Phys. Rev. Lett.* **93**, 156805 (2004).

[114] N. C. Bishop, M. Padmanabhan, K. Vakili, Y. P. Shkolnikov, E. P. De Poortere, and M. Shayegan, Valley polarization and susceptibility of composite fermions around a filling factor $\nu = 3/2$, *Phys. Rev. Lett.* **98**, 266404 (2007).

[115] M. Padmanabhan, T. Gokmen, and M. Shayegan, Ferromagnetic fractional quantum Hall states in a valley-degenerate two-dimensional electron system, *Phys. Rev. Lett.* **104**, 016805 (2010).

[116] M. Padmanabhan, T. Gokmen, and M. Shayegan, Density dependence of valley polarization energy for composite fermions, *Phys. Rev. B* **80**, 035423 (2009).

[117] M. Padmanabhan, T. Gokmen, and M. Shayegan, Composite fermion valley polarization energies: Evidence for particle-hole asymmetry, *Phys. Rev. B* **81**, 113301 (2010).

[118] V. S. Khrapai, A. A. Shashkin, M. G. Trokina, V. T. Dolgopolov, V. Pellegrini, F. Beltram, G. Biasiol, and L. Sorba, Filling factor dependence of the fractional quantum Hall effect gap, *Phys. Rev. Lett.* **100**, 196805 (2008).

[119] C. P. Puls, N. E. Staley, and Y. Liu, Interface states and anomalous quantum oscillations in hybrid graphene structures, *Phys. Rev. B* **79**, 235415 (2009).

[120] T. Ando, Screening effect and impurity scattering in monolayer graphene, *J. Phys. Soc. Jpn.* **75**, 074716 (2006).

[121] M. Koshino, T. Nakanishi, and T. Ando, Interface Landau levels in graphene monolayer-bilayer junctions, *Phys. Rev. B* **82**, 205436 (2010).

[122] T. Mueller, F. Xia, M. Freitag, J. Tsang, and P. Avouris, Role of contacts in graphene transistors: A scanning photocurrent study, *Phys. Rev. B* **79**, 245430 (2009).

[123] I. V. Kukushkin, K. von Klitzing, and K. Eberl, Spin polarization of composite fermions: Measurements of the Fermi energy, *Phys. Rev. Lett.* **82**, 3665 (1999).

[124] J. H. Smet, R. A. Deutschmann, W. Wegscheider, G. Abstreiter, and K. von Klitzing, Ising ferromagnetism and domain morphology in the fractional quantum Hall regime, *Phys. Rev. Lett.* **86**, 2412 (2001).

[125] J. H. Smet, R. A. Deutschmann, F. Ertl, W. Wegscheider, G. Abstreiter, and K. von Klitzing, Gate-voltage control of spin interactions between electrons and nuclei in a semiconductor, *Nature* **415**, 281 (2002).

[126] B. Verdene, J. Martin, G. Gamez, J. Smet, K. Von Klitzing, D. Mahalu, D. Schuh, G. Abstreiter, and A. Yacoby, Microscopic manifestation of the spin phase transition at filling factor 2/3, *Nat. Phys.* **3**, 392 (2007).

[127] R. R. Du, A. S. Yeh, H. L. Stormer, D. C. Tsui, L. N. Pfeiffer, and K. W. West, Fractional quantum Hall-effect around $\nu = 3/2$ - composite fermions with a spin, *Phys. Rev. Lett.* **75**, 3926 (1995).

[128] M. Chen, W. Kang, and W. Wegscheider, Metamorphosis of the quantum Hall ferromagnet at $\nu = 2/5$, *Phys. Rev. Lett.* **91**, 116804 (2003).

[129] J. P. Eisenstein, H. L. Stormer, L. Pfeiffer, and K. W. West, Evidence for a phase-transition in the fractional quantum Hall-effect, *Phys. Rev. Lett.* **62**, 1540 (1989).

[130] R. G. Clark, S. R. Haynes, A. M. Suckling, J. R. Mallett, P. A. Wright, J. J. Harris, and C. T. Foxon, Spin configurations and quasiparticle fractional charge of fractional-quantum-Hall-effect ground-states in the $N = 0$ Landau-level, *Phys. Rev. Lett.* **62**, 1536 (1989).

[131] J. P. Eisenstein, H. L. Stormer, L. N. Pfeiffer, and K. W. West, Evidence for a spin transition in the $\nu = 2/3$ fractional quantum Hall-effect, *Phys. Rev. B* **41**, 7910 (1990).

[132] L. W. Engel, S. W. Hwang, T. Sajoto, D. C. Tsui, and M. Shayegan, Fractional quantum Hall-effect at $\nu = 2/3$ and $\nu = 3/5$ in tilted magnetic-fields, *Phys. Rev. B* **45**, 3418 (1992).

[133] H. Cho, J. B. Young, W. Kang, K. L. Campman, A. C. Gossard, M. Bichler, and W. Wegscheider, Hysteresis and spin transitions in the fractional quantum Hall effect, *Phys. Rev. Lett.* **81**, 2522 (1998).

[134] V. M. Apalkov, and T. Chakraborty, Controllable driven phase transitions in fractional quantum Hall states in bilayer graphene, *Phys. Rev. Lett.* **105**, 036801 (2010).

[135] Z. Papic, R. Thomale, and D. A. Abanin, Tunable electron interactions and fractional quantum Hall states in graphene, *Phys. Rev. Lett.* **107**, 176602 (2011).

[136] K. I. Bolotin, F. Ghahari, M. D. Shulman, H. L. Stormer, and P. Kim, Observation of the fractional quantum Hall effect in graphene, *Nature* **462**, 196 (2009).

[137] B. E. Feldman, B. Krauss, J. H. Smet, and A. Yacoby, Unconventional sequence of fractional quantum Hall states in suspended graphene, *Science* **337**, 1196 (2012).

[138] K. Park, and J. K. Jain, Phase diagram of the spin polarization of composite fermions and a new effective mass, *Phys. Rev. Lett.* **80**, 4237 (1998).

[139] T. M. Kott, B. Hu, S. H. Brown, and B. E. Kane, Valley degenerate 2D electrons in the lowest Landau level, *arXiv: 1210.2386v1* (2012).

[140] K. Snizhko, V. Cheianov, and S. H. Simon, Importance of interband transitions for the fractional quantum Hall effect in bilayer graphene, *Phys. Rev. B* **85**, 201415 (2012).

[141] V. M. Apalkov, and T. Chakraborty, Stable Pfaffian state in bilayer graphene, *Phys. Rev. Lett.* **107**, 186803 (2011).

[142] B. E. Feldman, A. J. Levin, B. Krauss, D. A. Abanin, B. I. Halperin, J. H. Smet, and A. Yacoby, Fractional quantum hall phase transitions and four-flux states in graphene, *Phys. Rev. Lett.* **111**, 076802 (2013).

[143] D. K. Ki, V. I. Fal'ko, and A. F. Morpurgo, Even-denominator fractional quantum Hall state in multi-terminal suspended bilayer graphene devices, *arXiv: 1305.4761v1* (2013).

[144] J. Martin, B. E. Feldman, R. T. Weitz, M. T. Allen, and A. Yacoby, Local compressibility measurements of correlated states in suspended bilayer graphene, *Phys. Rev. Lett.* **105**, 256806 (2010).

[145] M. R. Peterson, and C. Nayak, More realistic hamiltonians for the fractional quantum Hall regime in GaAs and graphene, *Phys. Rev. B* **87**, 245129 (2013).

[146] B. Hunt, J. D. Sanchez-Yamagishi, A. F. Young, M. Yankowitz, B. J. LeRoy, K. Watanabe, T. Taniguchi, P. Moon, M. Koshino, P. Jarillo-Herrero, and R. C. Ashoori, Massive Dirac fermions and Hofstadter butterfly in a van der Waals heterostructure, *Science* **340**, 1427 (2013).

[147] C. Tőke, and V. I. Fal'ko, Intra-Landau-level magnetoexcitons and the transition between quantum Hall states in undoped bilayer graphene, *Phys. Rev. B* **83**, 115455 (2011).

[148] T. Nakanishi, M. Koshino, and T. Ando, Transmission through a boundary between monolayer and bilayer graphene, *Phys. Rev. B* **82**, 125428 (2010).

[149] Z. X. Hu, and W. Ding, Edge states at the interface between monolayer and bilayer graphene, *Phys. Lett. A* **376**, 610 (2012).

[150] M. Kharitonov, Edge excitations of the canted antiferromagnetic phase of the $\nu = 0$ quantum Hall state in graphene: A simplified analysis, *Phys. Rev. B* **86**, 075450 (2012).

[151] J. Martin, The ultimate guide to the SPM (2010).